South Carolina
Department of Transportation

U.S. Department
of Transportation

Federal Highway Administration

CLEMSON UNIVERSITY

REAL TIME MEASUREMENT OF SCOUR DEPTHS AROUND BRIDGE PIERS AND ABUTMENTS

Final Report
Report No. FHWA-SC-14-05

By

Abdul A. Khan
Huriye S. Atamturktur

Glenn Department of Civil Engineering
Clemson University
Clemson, SC 29634

January 2015

South Carolina
Department of Transportation
P. O. Box 191
Columbia, SC 29202-0191

Technical Report Documentation Page

1. Report No. FHWA-SC-14-05	2. Government Accession No.	3. Recipient's Catalog No.
4. Title and Subtitle Real Time Measurement of Scour Depths Around Bridge Piers and Abutments		5. Report Date January 2015 6. Performing Organization Code
7. Author(s) A. A. Khan and H. S. Atamturktur		8. Performing Organization Report No.
9. Performing Organization Name and Address Glenn Department of Civil Engineering Clemson University 110 Lowry Hall Clemson, SC 29634-0911		10. Work Unit No. (TRAIS) 11. Contract or Grant No. SPR 692
12. Sponsoring Agency Name and Address South Carolina Department of Transportation Office of Materials and Research 1406 Shop Road Columbia, South Carolina 29201		13. Type of Report and Period Covered Final Report January 2011 to January 2015 14. Sponsoring Agency Code

15. Supplementary Notes

Prepared for the SCDOT in cooperation with the Federal Highway Administration

16. Abstract

Scour is one of the most significant threats to bridge infrastructure and is the leading cause of failure within the United States. Scour monitoring is an approved countermeasure as reported by the Federal Highway Administration. As the monitoring techniques available range from simple devices that rest on or in the channel bed to advanced scanning systems that provide a bed contour profile, a concise study of the state of the art in real time scour measurement capabilities is required.

The available techniques for monitoring scour are reviewed to highlight the governing physics, to evaluate field performance, and to identify the effect of environmental factors on accuracy and reliability. From this assessment, two devices are selected for further study: a sonar fathometer and a Time Domain Reflectometry (TDR) device. A novel device, called a Vibration-based Turbulent Pressure (VTP) sensor, is proposed which exploits the turbulence in open channels to locate the bed level. This sensor vibrates at significantly higher amplitude when in the channel flow relative to an identical sensor located in the sediment.

The vibration-based method, time domain reflectometry, and sonar devices are evaluated against simulated field conditions in order to determine their relative sensitivities to environmental conditions. These tests reveal that sonar and time domain reflectometry devices can be influenced by channel salinity and temperature. In addition, the sonar device is shown to be sensitive to the suspended sediment concentration in the channel, its height relative to the bed, and bed topography within the sonar beam. The vibration-based method is shown to be the least sensitive to environmental factors in the channel. In addition, the VTP device can provide reliable results in highly misaligned flows. Finally, the performance of TDR, sonar, and the vibration-based technique is evaluated under field conditions.

The field tests reveal that all instruments perform at their accuracy level. The sonar must be deployed close to the bed to guarantee that the beam will be contained within the scour hole and would not have large width. In addition, the site should not have high suspended load concentration. The TDR is insensitive to suspended sediment; however, salinity greater than 0.5 parts per thousand renders the instrument inoperable. The VTP is proven to be insensitive to all the environmental factors. However, field deployment reveals that debris accumulation may cause the instrument to report false bed location.

17. Key Words	18. Distribution Statement
Scour, measuring instruments, bridge piers, bridge abutments, flood damage.	No restrictions.

19. Security Classif. (of this report)	20. Security Classif. (of this page)	21. No. of Pages	22. Price
Unclassified	Unclassified		

ABSTRACT

Scour is one of the most significant threats to bridge infrastructure and is the leading cause of failure within the United States. Scour monitoring is an approved countermeasure as reported by the Federal Highway Administration. As the monitoring techniques available range from simple devices that rest on or in the channel bed to advanced scanning systems that provide a bed contour profile, a concise study of the state of the art in real time scour measurement capabilities is required.

The available techniques for monitoring scour are reviewed to highlight the governing physics, to evaluate the field performance, and to identify the effect of environmental factors on the accuracy and reliability. From this assessment, two devices are selected for further study; a sonar fathometer and a Time Domain Reflectometry (TDR) device. Several environmental factors are reported that influence these devices, including channel temperature, salinity, and suspended sediment concentration. A novel device, called Vibration-based Turbulent Pressure (VTP) sensor, is proposed which exploits the turbulence in open channels to locate the bed level. The device uses a sensor that is sensitive to the dynamic pressure due to the natural turbulence in open channels. This sensor vibrates at significantly higher amplitude when in the channel flow relative to an identical sensor located in the sediment.

The vibration-based method, time domain reflectometry, and sonar devices are evaluated against simulated field conditions in order to determine their relative sensitivities to environmental conditions. These tests reveal that sonar and time domain reflectometry devices can be influenced by channel salinity and temperature. In addition,

the sonar device is shown to be sensitive to the suspended sediment concentration in the channel, its height relative to the bed, and bed topography within the sonar beam. The vibration-based method is shown to be insensitive to the suspended sediment concentration, bed sediment type, and other environmental factors in the channel. The effect of flow angle is also evaluated for the vibration method, and reveals that it can provide reliable results in highly misaligned flows. An analytical model is built for further optimization of the device. The model is then verified, calibrated, and validated with experimental data. The validated model is used to develop a field prototype, which is tested experimentally and reveals satisfactory performance for deployment at bridge sites. Finally, the performance of TDR, sonar, and the vibration-based technique is evaluated under field conditions.

The field tests reveal that all instruments perform at their accuracy level. The sonar must be deployed close to the bed to guarantee that the beam will be contained within the scour hole and would not have large width. In addition, the site should not have high suspended load concentration. The TDR is insensitive to suspended sediment; however, salinity greater than 0.5 parts per thousand renders the instrument inoperable. The VTP is proven to be insensitive to all the environmental factors. However, field deployment reveals that debris accumulation may cause the instrument to report false bed location.

ACKNOWLEDGMENTS

We acknowledge the South Carolina Department of Transportation (SCDOT) for providing a grant and support to carry out the research and investigation in this project. We also would like to acknowledge the support of the SCDOT in field installations of devices.

We would like to acknowledge technical staff of the Glenn Department of Civil Engineering and the College of Engineering and Science at Clemson University for their help in experimental setup, manufacturing instruments, and field installation.

TABLE OF CONTENTS

Page

TITLE PAGE i

ABSTRACT ii

ACKNOWLEDGMENTS iv

LIST OF TABLES ix

LIST OF FIGURES x

CHAPTER 1 INTRODUCTION 1

CHAPTER 2 THE STATE OF THE ART IN SCOUR MONITORING 5

2.1 Introduction 5

2.2 Background 5

2.3 Point Scour Measurement Methods 8

2.3.1 Sounding Rods 8

2.3.2 Float-Out Devices 10

2.3.3 Magnetic Sliding Collars 13

2.3.4 Sonar/Fathometer 17

2.3.5 Time Domain Reflectometry 23

2.3.6 Fiber Optics 31

2.3.7 Temperature Measurements 37

2.3.8 Piezoelectric Film Sensors 40

2.3.9 Mercury Tip Switches 42

2.4 Distributed Scour Measurement Methods 43

2.4.1 Radar 43

2.4.2 Bridge Vibration Measurements 47

2.4.3 Advanced Sonar Techniques 53

2.5 Summary 59

CHAPTER 3 DEVELOPMENT OF A NEW SCOUR MEASUREMENT INSTRUMENT 65

3.1 Introduction 65

3.2 Numerical Proof of Concept 68

3.2.1 Modeling of Open Channel Turbulent Flow 69

3.2.2 Modeling of VTP Dynamic Response: 72

3.2.3 Numerical Model Results 74

3.3 Experimental Setup 78

3.4 Results and Discussion 81

3.4.1 Verification of the Hypothesis behind VTP 82

3.4.2 Assessing Performance of VTP in Scour Hole 85

3.4.3 Precision Assessment 86

3.5 Summary 91

CHAPTER 4 OPTIMIZATION OF THE VIBRATION-BASED TURBULENT PRESSURE DEVICE FOR FIELD DEPLOYMENT 93

4.1 Introduction 93

4.2 Modeling Approach 94

4.2.1 Model for Prediction of RMS Values of Fluctuating Turbulent Velocity 97

4.2.2 Spectral Model for Turbulence 100

4.2.3 Dynamic Pressure 103

4.2.4 Structural Response 105

4.3 Model Verification, Calibration, and Validation 110

4.3.1 Model Verification 110
4.3.2 Model Calibration 112
4.3.3 Model Validation 122
4.4 VTP Optimization for Field Deployment 125
4.5 Field Prototype Performance 127
4.5.1 Measured Energy Content Profile 129
4.5.2 Measured and Predicted Sensitivity to Flow Misalignment 130
4.6 Summary 131
CHAPTER 5 ROBUSTNESS OF THE SELECTED SCOUR MEASURING DEVICES 133
5.1 Introduction 133
5.2 Previous Studies of Factors Affecting Sonar 134
5.3 Previous Studies of Factors Affecting TDR 139
5.4 Test Setup 143
5.4.1 Sonar Experimental Setup 143
5.4.2 TDR Experimental Setup 145
5.4.3 VTP Experimental Setup 146
5.5 Sonar: Temperature Effects 148
5.6 Sonar: Salinity Effects 150
5.7 Sonar: Turbidity Effects 151
5.8 Sonar: Topography and Beam Width Effect 156
5.9 TDR: Temperature Effects 158
5.10 TDR: Salinity Effects 161
5.11 TDR: Turbidity Effects 162

5.12 VTP: Turbidity 162
5.13 VTP: Flow Misalignment 164
5.14 VTP: Flow Velocity 165
5.15 VTP: Bed Sediment Type 166
5.16 Summary 167
CHAPTER 6 FIELD INSTALLATION AND DATA COLLECTION 170
6.1 Introduction 170
6.2 Selection Criteria of Field Sites 170
6.3 Field Site 1 171
6.4 Field Site 2 175
6.5 Installation and Data Collection Procedure 177
6.6 Bed Elevation Results from Field Site 1 179
6.6.1 Bed Elevation History Using TDR 179
6.6.2 Bed Elevation History Using VTP 183
6.6.3 Performance Comparison between TDR and VTP 187
6.7 Bed Elevation Results from Field Site 2 189
6.7.1 Bed Elevation History Using Sonar 189
6.7.2 Bed Elevation History Using TDR 194
6.7.3 Performance Comparison between TDR and Sonar 198
6.8 Summary 199
CHAPTER 7 CONCLUSIONS 200
7.1 Summary of the Research 200
7.2 Recommendations 203
BIBLIOGRAPHY 207

LIST OF TABLES

Table Page

Table 2-1: Soil properties pertinent for radar EM techniques, adapted from Millard et al. (1998). 47

Table 2-2: Proposed severity ratings for FMEA analysis of scour monitoring system. 60

Table 2-3: Proposed occurrence ratings for FMEA analysis of scour monitoring system. 60

Table 2-4: Proposed detectability ratings for FMEA analysis of scour monitoring system. 60

Table 2-5: Example FMEA analysis for TDR system. 61

Table 2-6: Summary of scour monitoring devices. 61

Table 4-1: Model and measured natural frequencies for modes in neoprene. 113

Table 4-2: Flow parameters for CHL flume tests. 114

Table 5-1: Range of percent relative error in water depth, and comparison with theoretical model. 151

Table 5-2: Range of percent relative error in water depth for various turbidities. 152

Table 5-3: Experimental results for case A. 157

Table 5-4: Experimental results for case B. 157

Table 7-1: FMEA analysis for the selected instruments. 204

Table 7-2: Recommendations for the selection of an instrument for field deployment. 206

LIST OF FIGURES

Figure Page

Figure 2.1: Example of float-out device installation. Highlights buoyant floats, tethered-buried switches, and wildlife tracker based transmitters. Based upon Yao et al. (2011) and Zabilansky (1996). 12

Figure 2.2: Example of a magnetic sliding collar installation. This figure is adapted from Richardson et al. (1996) and Nassif et al. (2002), and shows the first embodiment of the MSC device. 15

Figure 2.3: Typical sonar system installation. Based upon Nassif et al. (2002). 18

Figure 2.4: Typical TDR waveform. 25

Figure 2.5: Piezoelectric film sensor. Based upon Lagasse et al. (1997). 41

Figure 3.1: Model response for the prototype VTP based upon SDOF model and turbulent spectrum. The units for displacement, velocity, and acceleration autospectra are ft Hz^{-1}, ft $s^{-1}Hz^{-1}$, ft $s^{-2}Hz^{-1}$, respectively. 75

Figure 3.2: Circular and square VTP normalized mean square response as computed from the response spectrum from 10 to 400 Hz for circular and square VTPs, for various plate areas, and material types. Each result is normalized by the deflected mode shape as given by Equation (3.13). 77

Figure 3.3: Prototype VTP configuration. Components include: (1) the compression fitting, (2) the vibrating membrane, (3) a washer, (4) toroid disk, (5) accelerometer, and (6) the support pipe. 80

Figure 3.4: Prototype VTP array installed in the flume. VTPs 1-4 are shown above the sand bed. The instrument is anchored to the flume wall. 81

Figure 3.5: Energy content of prototype VTPs as a function of distance from the water/sediment interface. Flow rates varied from 2.12 to 4.94 cfs. Mean values plotted along with ± 1 standard deviation and the unscoured bed level. 82

Figure 3.6: VTP energy content of prototype device versus flume flow rates. 83

Figure 3.7: Turbulent energy content of prototype VTPs in unscoured and 0.18 ft deep scour hole. The mean values are denoted by the points while the

dotted lines represent the ± 1 standard deviation of the measured results around the mean value. 86

Figure 3.8: Energy content of prototype VTPs in scour holes of various sizes. The mean profile with ± 1 standard deviation is plotted alongside the slope of the mean profile, scaled by a factor of 1/10. The VTP and the independently measured scour hole depths are indicated for each experiment. 88

Figure 3.9: VTP estimated scour depth versus actual scour values. The scour values determined from the VTP setup are based on the point of maximum slope. An ideal sensor would fall on the 1:1 line. 90

Figure 4.1: Channel parameters relevant to the Navier-Stokes equations. 95

Figure 4.2: Sample turbulent velocity time history. 96

Figure 4.3: Area integration of dynamic turbulent pressure distribution across VTP disk. 104

Figure 4.4: Components of the joint acceptance for the 1st mode of the plate..... 109

Figure 4.5: Variation in VTP turbulent pressure as a function of number of elements. 111

Figure 4.6: Distribution of velocity as a function of depth in the channel for run 1. 115

Figure 4.7: Distribution of $u'v'$ as a function of depth in the channel for run 1..... 116

Figure 4.8: Measured and model root mean square of u' normalized by friction velocity as a function of relative depth in the channel (run 1). 117

Figure 4.9: Comparison of model turbulent velocity fluctuation spectrum with published results from Figure 7b of Kironoto and Craf (1994). 118

Figure 4.10: Comparison of model turbulent velocity fluctuation spectrum with published results from Figure 4.15 of Nakagawa and Nezu (1993). 118

Figure 4.11: Power spectral density of u' at y/h of 0.1 from run 1. 119

Figure 4.12: Power spectral density of u' at y/h of 0.2 from run 1. 120

Figure 4.13: Power spectral density of u' at y/h of 0.3 from run 1. 120

Figure 4.14: Measured and model acceleration response spectra for run 3 at y/h of 0.35. VTP plate is neoprene (0.063 inch thick, 0.787 inch radius). 124

Figure 4.15: Measured and model acceleration response spectra for run 3 for y/h of 0.66. VTP plate is neoprene (0.063 inch thick, 0.787 inch radius). 124

Figure 4.16: Optimization of VTPs' size and thickness for field deployment. 127

Figure 4.17: Schematic of field VTP configuration..... 128

Figure 4.18: Field prototype. 128

Figure 4.19: Performance of the field prototype in CHL flume at different velocity..... 129

Figure 4.20: Measured and analytical model response as a function of flow misalignment..... 131

Figure 5.1: Relative error in distance measurements due to temperature changes, relative to the value at 68°F ($c = 4920$ ft/s). 135

Figure 5.2: Relative error in distance measurements due to salinity, relative to the speed of sound at 68°F. 136

Figure 5.3: Density variation in the channel flow, adapted from Robins (1990). 137

Figure 5.4: Reflection coefficient versus (a) sediment unit weight, (b) suspended sediment concentration. The reflection coefficient is calculated for density ratios according to the Robins (1990) model with a water density of 62.4 lb/ft^3 139

Figure 5.5: Effect of varying channel salinity levels and temperature on the dielectric constant and TDR measurements. (a) Dielectric constant, per Stogryn (1971). (b) Relative percentage error in TDR measurements. 141

Figure 5.6: Effect of varying suspended sediment concentration on the dielectric constant and TDR measurements. (a) Impact on dielectric constant per Yu and Yu (2011). (b) Relative error in TDR measurements. Sediment types as shown in Das (1998). 142

Figure 5.7: Schematic of the turbidity stratification test..... 144

Figure 5.8: Schematic of the scour hole/beam ratio tests. 145

Figure 5.9: Schematic of the test using TDR. 146

Figure 5.10: VTP setup as installed in CHL flume for channel effects study. 147

Figure 5.11: Variation in relative error of sonar measurements with temperature for water depth of 3 ft. 148

Figure 5.12: Variation in relative error of sonar measurements with temperature for a water depth of 4.1 ft. 149

Figure 5.13: Variation in relative error of sonar measurements with temperature for a water depth of 5.1 ft. 149

Figure 5.14: Relative error in the sonar reading for various turbidity concentrations and velocities. 153

Figure 5.15: Average standard deviation of sonar readings based on Figure 5.14..... 153

Figure 5.16: Standard deviation of sonar for various stratification concentration and velocities..... 155

Figure 5.17: Sonar beam to scour hole size experimental setup. 156

Figure 5.18: TDR waveform in various water temperatures for water depth 1.92 ft. 158

Figure 5.19: Relative error in the TDR readings for various temperatures and water depth of 2.41 ft. 159

Figure 5.20: Relative error in the TDR readings for various temperatures and water depth of 1.92 ft. 160

Figure 5.21: Sensitivity of TDR waveform to salinity. 161

Figure 5.22: Effect of turbidity on TDR. 162

Figure 5.23: VTP energy content for various turbidity levels and channel flow velocities. 163

Figure 5.24: VTP energy content as a function of the flow misalignment. 165

Figure 5.25: Variation of VTP energy content with channel velocity. 166

Figure 5.26: Variation of VTP energy content for various bed sediment types. 167

Figure 6.1: Satellite view of Field Site 1 (Source: Google Earth). 172
Figure 6.2: Solar panel and data acquisition system at Field Site 1. 173
Figure 6.3: SCDOT crew assisting in running the cable at Field Site 1. 173
Figure 6.4: Instruments mounted on the face of the footing pad at the pier. 174
Figure 6.5: TDR (on the right) and VTP (on the left) at Field Site 1. 174
Figure 6.6: TDR and sonar at Field Site 2 (Source: Google Earth). 175
Figure 6.7: SCDOT crew assisting in running the cable at Field Site 2. 176
Figure 6.8: Installed TDR (on the right) and sonar (on the left) at Field Site 2. 176
Figure 6.9: Bank view showing the pier located in the middle of the river. 177
Figure 6.10: Bed elevation from TDR in March 2014. 180
Figure 6.11: Bed elevation from TDR in April 2014. 180
Figure 6.12: Bed elevation from TDR in May 2014. 181
Figure 6.13: Bed elevation from TDR in June 2014. 181
Figure 6.14: Bed elevation from TDR in July 2014. 182
Figure 6.15: Bed elevation from TDR in August 2014. 182
Figure 6.16: Bed elevation from TDR in September 2014. 183
Figure 6.17: Bed elevation from VTP in March 2014. 184
Figure 6.18: Bed elevation from VTP in April 2014. 184
Figure 6.19: Bed elevation from VTP in May 2014. 185
Figure 6.20: Bed elevation from VTP in June 2014. 185
Figure 6.21: Bed elevation from VTP in July 2014. 186
Figure 6.22: Bed elevation from VTP in August 2014. 186
Figure 6.23: Bed elevation from VTP in September 2014. 187

Figure 6.24: Comparison of bed elevation obtained from TDR and VTP for scour event 1. 188

Figure 6.25: Comparison of bed elevation obtained from TDR and VTP for scour event 2. 189

Figure 6.26: Bed elevation from sonar in March 2014. 190

Figure 6.27: Bed elevation from sonar in April 2014. 191

Figure 6.28: Bed elevation from sonar in May 2014. 191

Figure 6.29: Bed elevation from sonar in June 2014. 192

Figure 6.30: Bed elevation from sonar in July 2014. 192

Figure 6.31: Bed elevation from sonar in August 2014. 193

Figure 6.32: Bed elevation from sonar in September 2014. 193

Figure 6.33: Bed elevation from TDR in March 2014. 194

Figure 6.34: Bed elevation from TDR in April 2014. 195

Figure 6.35: Bed elevation from TDR in May 2014. 195

Figure 6.36: Bed elevation from TDR in June 2014. 196

Figure 6.37: Bed elevation from TDR in July 2014. 196

Figure 6.38: Bed elevation from TDR in August 2014. 197

Figure 6.39: Bed elevation from TDR in September 2014. 197

Figure 6.40: Comparison of bed elevation obtained from sonar and TDR. 198

CHAPTER 1

INTRODUCTION

One of the most significant financial investments in any transportation infrastructure system are the bridges that connect otherwise geographically isolated communities. Failure of these structures can have significant impacts, both in financial and human terms. The leading cause of failures in the United States is due to the removal of bed material surrounding the foundations of bridge piers and abutments, a process known as scour. Scour failures, accounting for 60% of all bridge failures (Lagasse et al., 1997), have resulted in the direct loss of lives, and have accounted for hundreds of millions of dollars in repair damage. Additionally, bridge failures due to scour can have a dramatic impact on the local community, with the financial impact estimated to be five times the actual repair cost (Rhodes and Trent, 1993). Therefore, it is necessary to protect these critical infrastructure elements against scour damage.

Local scour is the process by which bed materials around the piers and abutments of a bridge are continuously removed by natural flow. Damage due to scour can be reduced by armoring or replenishing bed materials or by regulating the peak flow so that the scour is restricted to a certain threshold. This threshold depends on the design consideration of the bridge in concern. Thus, scour monitoring around the bridge piers and abutments is essential. When the scour depth approaches the threshold value, protective measures need to be implemented.

There are generally three types of scours that affect the performance and safety of bridges, namely, local scour, contraction scour, and scour due to general aggradation and degradation of a channel reach (Parker et al. 1997). Local scour is the removal of sediment around bridge piers and abutments and is the result of a flow pattern that develops around an obstacle placed in the flow. Water flowing past a pier and/or abutment may remove sediment around the structure forming a scour hole. Contraction scour is the removal of sediment from the bottom and sides of the river. It is caused by an increase in the flow velocity as the water moves through a bridge opening that is narrower than the river upstream. Scour arising from aggradation and degradation is due to long-term removal/deposition of sediment in a river reach. Sediment removal and resulting lowering of a river bottom are natural processes, however, near bridge abutments and piers large amounts of sediment may be removed over time (Deng and Cai, 2010). The total scour depth is determined by adding three scour components which includes the long-term aggradation and degradation of the river bed, contraction scour at the bridge, and local scour at the piers or abutments.

Scour damage can be prevented by armoring the bed to reduce the amount of scour or by adjusting the river hydraulics to reduce the peak flow, requiring significant amounts of time and financial resources for implementation. Scour monitoring, however, can be implemented relatively quickly and at reduced cost relative to the other preventative measures. For this reason the Federal Highway Administration's Highway Engineering Circular No. 23 lists scour monitoring as a viable countermeasure for scour critical bridges (Lagasse et al., 2009). Scour at bridges occurs over time, with peak flow

events progressively adding to the scour around the pier or abutment. Thus, by monitoring the history of scour at a bridge, it is possible to determine if the scour depth is approaching the critical value determined during the bridge design. As the scour depth approaches this critical value, planning for protection of the bridge site may begin. Given the importance of scour monitoring in determining the health of the bridge, it is necessary to understand and advance the state of the art in scour monitoring. To that end, a study has been conducted with the following objectives:

Objective 1: Understand the state of the art in scour monitoring, highlighting the physical principles behind the operation of the devices, review of the documented field performance of the devices, and evaluation of sensitivities to environmental factors that can influence the scour measurement accuracy;

Objective 2: Evaluate the best in class scour monitoring instruments under simulated field conditions to explore their sensitivity to common environmental factors in natural channels, such as salinity, temperature, and suspended sediment;

Objective 3: Evaluate the feasibility of a novel scour monitoring method that exploits the natural turbulence in open channels as a mean to determine the water/sediment interface;

Objective 4: Optimize the novel method for field deployment;

Objective 5: Confirm the performance of the novel method with laboratory experiments.

Objective 6: Evaluate the performance of the best in class scour measuring instruments with the novel scour monitoring method in field condition.

This report outlines the work conducted to accomplish these objectives. In Chapter 2, the state of the art in scour monitoring is explored by evaluating the currently available measurement techniques, of which the best in class devices were determined to be the sonar fathometer and the time domain reflectometry (TDR) method. Chapter 3 focuses on the feasibility study of the novel. Chapter 4 outlines the optimization of a prototype device (VTP) for field deployment. Chapter 5 discusses the results of several experiments that were conducted to evaluate the performance of sonar, TDR, and VTP under common channel conditions. Chapter 6 presents the scour monitoring data collected by sonar, TDR, and VTP at two bridge sites in South Carolina. Finally, Chapter 7 summarizes the study and provides recommendations.

CHAPTER 2

THE STATE OF THE ART IN SCOUR MONITORING

2.1 Introduction

Scour damage to bridges, a widespread and costly threat to transportation infrastructure, can be countered with appropriate monitoring of the riverbed as pointed out in the U.S. Federal Highway Administration HEC-23. The available monitoring methods however, are sensitive to conditions in natural channels, such as temperature, turbidity, etc. Thus, understanding the impact of these conditions on the performance of existing scour monitoring methods is essential for successful deployment of these instruments in the field.

2.2 Background

Scour around bridge piers and abutments occurs when high velocity flows impinge on the riverbed, leading to the removal of bed material, which undermines the structural stability of bridge elements located in the flow. Scour monitoring, in turn, is important as it allows the infrastructure owner to monitor the health of the bridge hardware. Additionally, scour monitoring is an approved countermeasure, similar to traditional physical countermeasures such as rip-rap (Lagasse et al., 2009). Therefore, it is necessary, to understand the physical operating principles and past field performance of any device deployed to monitor scour.

This chapter is adapted from the article published by Fisher et al. (2013a) based on the work done for this project.

The degradation of the channel bed around bridge piers and abutments occurs in natural channels around the globe and has historically caused failure of bridges. The damage to bridge infrastructure due to scour is costly to repair, and the failures can result in the loss of lives. Several bridge failures have been directly attributed to scour including the I-90 Bridge over the Schoharie Creek in New York in 1987, the U.S. 51 Bridge over the Hatchie River in Tennessee in 1989, and the I-5 Bridge over the Arroyo Pasajero River in California in 1995. The NTSB investigated both the Schoharie Creek and Hatchie River Bridge failures and concluded that scour was the cause of failure. The I-90 Bridge failure was attributed to inadequate protection of a pier footing leading to the formation of a scour hole that undermined the pier, while the U.S. 51 failure was attributed to the migration of the main channel, which undermined a bridge column, leading to the collapse of the bridge (NTSB, 1987; NTSB, 1989). The I-5 collapse was attributed to a 9.8 ft scour hole, which developed over the long-term, and led to the collapse of the bridge columns (Arneson et al., 2012). Additionally, the United States Geological Survey (USGS) reported that the number of bridges damaged during flood events ranged from 17 in the U.S. Northeast in 1987 to more than 2,500 in the Midwest during the 1993 flood season (Mueller, 2000). Murillo (1987) reported that during 1961-1974, 46 of the 86 major failures of bridges in the U.S. were due to scour, more than any other cause. Lin et al. (2004) reported that 68 bridges in the U.S. were damaged due to scour from 1996 to 2001. Furthermore, Richardson and Price (1993) reported that in 1993, 109,464 bridges in the U.S. were scour critical or scour susceptible and required countermeasures. Hunt (2009) reported that of the 590,000 bridges in the U.S., 20,904 are

scour critical. Overall, estimates place scour as the leading cause of bridge failure, accounting for approximately 60% of all events (Lagasse et al., 1997).

Scour around bridge piers and abutments is unavoidable, it can result in significant human loss and financial costs. The human impact is associated directly with the loss of life during a bridge collapse as well as the indirect costs associated with loss of infrastructure. During the Schoharie Bridge collapse, 10 individuals lost their lives (NTSB, 1987). The U.S. 51 Bridge collapse in Tennessee cost 8 lives, while the I-5 Bridge failure over the Arroyo Pasajero River cost the lives of 7 individuals (NTSB, 1989; Arneson et al., 2012). In addition to the direct cost of human lives, the indirect human impact is felt through the loss of critical infrastructure, which can impede both evacuation routes (e.g., during a hurricane) or relief and recovery efforts after a flood. Butch (1996) reported that the cost of flood repairs during the 1980s was estimated to be $300 million. More recently, the USGS reported that from 1993 to 1995, floods in the Midwest, Georgia and Virginia cost $178 million, $130 million and $40 million, respectively (Mueller, 2000). These figures account for the total cost of damage from floods. Brice and Blodgett (1978) estimated the cost of repairing a bridge with scour damage to be $100 million per event during 1964-1972. Lagasse et al. (1997) reported that $30 million is spent annually on scour related bridge repairs. In addition to the cost of the failures and associated repairs, the economic impact of a bridge failure to the local community is estimated to be as much as five times the repair costs (Rhodes and Trent, 1993).

Thus, given the widespread nature of scour damage, the rapid time frame in which a scour hole can form, and the ancillary costs of repair, an adequate methodology for monitoring the formation of scour holes around bridge structural elements is essential. In an effort to accomplish this goal, 32 states have deployed scour monitoring systems and employed 164 sonar fathometers on 48 bridges (Lagasse et al., 1997). In addition, several state level Departments of Transportation and the Federal Highway Administration have funded various scour monitoring programs. In order to make use of the field information gained from these and other projects, it is necessary to review the performance of the various devices used in scour monitoring campaigns.

2.3 Point Scour Measurement Methods

2.3.1 Sounding Rods

Sounding rods and sounding weights, adapted from depth finding methods on naval vessels, have been used since the early 19th century to monitor the depth to the riverbed from bridge platforms (Lagasse et al., 1997). The latest embodiment consists of a solid rod and base plate that rests on the riverbed surface (Zabilansky, 1996). As the scour hole develops, the rod moves down with the bed surface from inside its support housing. This motion is tracked with a chain that connects the rod to the support housing, but does not provide any resistance to motion. The downward movement of this chain is then tracked from the bridge deck or another fixed datum, permitting measurement of the maximum scour underneath the rod location. During a refill event, the base plate and rod will be buried and will not provide information about the aggradation of material in the scour hole. The ability to record refill is important for scour monitoring as it provides

information that is not obtained via regular bridge inspections. Refill typically occurs with material of different properties than the native bed. Thus, a refilled scour hole can appear as acceptable during a survey, but in reality the foundation is undermined.

Sounding rods were tested during both scaled laboratory and full-scale field testing as part of the National Cooperative Highway Research Program (NCHRP) 21-3. During the laboratory testing, two base plate sizes (3 inches and 5 inches) were tested for multiple channel bed materials. Overall, the results showed that with either base plate, the scour readings were within +/- 10% of the scour depth (Lagasse et al., 1997). During the field installation at the Orchard Bridge site in Colorado, the device provided readings of the location of the channel bed; however, various challenges were encountered with the device.

The sounding rod tests indicated several factors that should be considered in scour measurements. In both the laboratory and the field environments, the experimental results indicated that the rod itself could penetrate the riverbed and gave a false depth reading. In the scaled testing, this was overcome via the addition of a larger base plate, which in the scaled model was three times the diameter of the rod. Adding the larger base plate, however, influenced the scour hole development. During the field campaign, measurements showed that the device had significant self-burial problems with the standard base plate. Additionally, a total failure of the device occurred during a major scour event in which the sounding rod moved out of the bottom of the support pipe and, in the process, damaged the encoder chain. Even during normal operation of the device

the encoder that logged the depth of the rod was problematic; further tests with this device were therefore abandoned (Lagasse et al., 1997).

Overall, sounding rods are limited in that they can only record the maximum scour, the device itself can penetrate the bed, depending upon the base plate size it is possible that the scour hole formation may be influenced, and the device is not robust as a large scour hole can result in total loss of the device.

2.3.2 Float-Out Devices

The devices that fall into this category vary greatly from basic buoyant floats to sophisticated radio transmitters that measure movement. Some of the commonly used float devices are shown in Figure 2.1. The simplest float-out devices are colored or numbered floats connected by a tether to a weight that acts as an anchor (DeFalco and Mele, 2002). Multiple floats and anchors are buried at various layers in the sediment, and as a scour event occurs, the float corresponding to the depth of degradation rise to the water surface. Field staff can then review those floats that have reached the surface to determine the depth of scour. In addition to the basic buoyant floats, several researchers have developed automated devices. Yao et al. (2011) reported on the use of switches that are tethered to a rod buried in the sediment, denoted as tethered-buried switches. The device consists of a switch housed inside a sealed aluminum tube that triggers when the unit orientation changes to a horizontal position. As the scour develops and uncovers the device, drag forces pull the sensor along the sediment surface, triggering the device. Zabilansky (1996) developed a more sophisticated form of a float-out device based upon wildlife movement tracking units consisting of a wireless transmitter that emits a timing

pulse, which varies if the device is in motion. These transmitters are instrumented along a support rod that is then buried in the sediment. If a transmitter is buried, it is not subject to any of the turbulent flow and therefore the timing pulse is stable. After a scour event, in which the transmitter is exposed, the water flowing past the transmitter causes it to move and vibrate, which changes the timing pulse. Thus, by monitoring the signal from each transmitter, it is possible to determine the depth of the scour hole present in the channel bed. In the field setup, each transmitter is assigned an individual frequency and the timing pulse of each is monitored by a telemetry system and data logger located on the bridge. A minimum flow velocity of 0.33 ft/s past the transmitter is required in order for the transmitter to register movement. An advantage of the transmitter based device over the other float-out devices discussed earlier is that during a refill event, where material is deposited in the scour hole, the transmitters will be re-buried. Thus, the wildlife tracker based transmitters can record maximum scour and refill, while the buoyant floats and tethered-buried switches can only provide information on the maximum scour.

The tethered-buried switches were deployed at two bridges in Texas; the US 59 Bridge over the Guadalupe River and the SH 80 Bridge over the San Antonio River. During the reported measurement period for both bridges, the device failed to trigger due to a lack of scour hole formation (Yoa et al., 2011). As a part of an ice and scour monitoring project (Zabilansky, 1996), fifteen wildlife based tracking transmitters were deployed around a bridge pier at the Bridge Street Bridge over the White River junction in Vermont. The transmitters were distributed over four rods and were placed at an

interval of 0.50 ft. Though two transmitters were lost due to potential damage during the field campaign, one transmitter recorded a scour event for nine hours before it was reburied after the breakup of the surface ice.

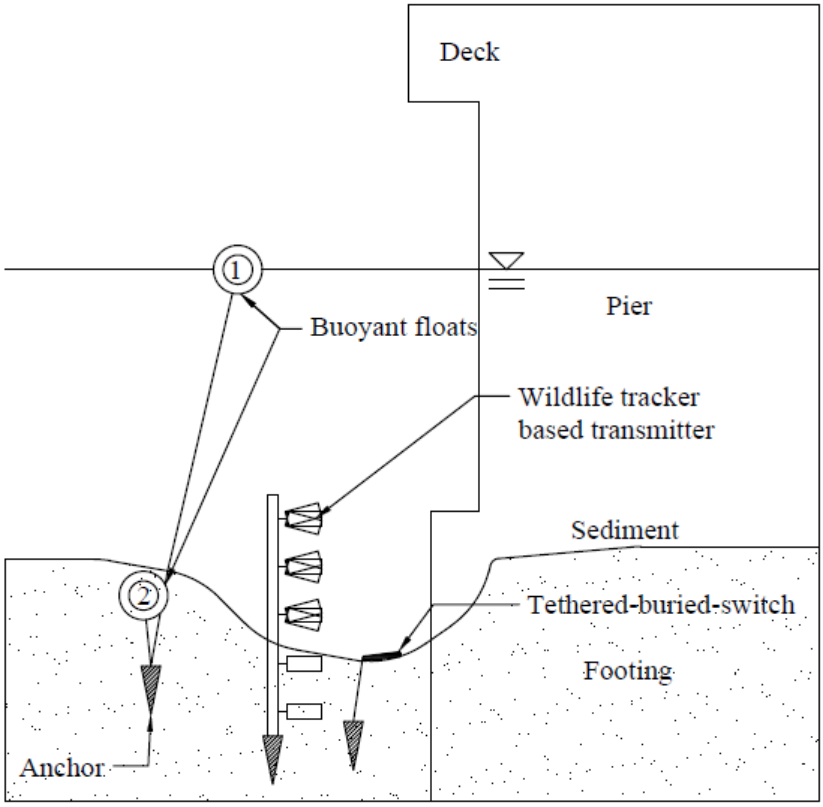

Figure 2.1: Example of float-out device installation. Highlights buoyant floats, tethered-buried switches, and wildlife tracker based transmitters. Based upon Yao et al. (2011) and Zabilansky (1996).

While the field performance of the float-out devices is limited, several potential factors that could influence the performance of these devices are anticipated. Since the tethered-buried switches lie on the riverbed once exposed by the scour, debris in the flow can damage the unit. Additionally, if the depth of scour exceeds the depth of the anchor

for the tethered-buried switches, the entire device can fail. The removal of the anchor by scour is also a potential problem with the buoyant floats and the wildlife tracker based transmitters. Furthermore, failure of individual devices due to debris is a concern as reported in the Vermont field tests, where two transmitters were lost.

Overall, for all float out devices in general, and for the buoyant floats and the tethered-buried switches in particular, the main disadvantage is that they require reinstallation after a scour event and thus, can only record the maximum scour depth. This difficulty was resolved with the wildlife tracker based transmitters that remain tethered to the support rod, allowing for reburial of the transmitters during a refill event. With the exception of the transmitter units, the use of float out devices during a long-term campaign is problematic and requires extensive use of field staff. Finally, as with all devices mounted in the channel bed, float-out devices are susceptible to debris damage and they also only provide information about the scour depth at the point immediately surrounding the location where they are installed.

2.3.3 Magnetic Sliding Collars

The magnetic sliding collar, MSC, is one of the several rod-and-collar based scour monitoring devices. MSC consists of a rod buried in the riverbed with an attached collar. The collar rests on the river bed and during a scour event the collar slides down the rod, thus measuring the bed scour. The MSC device was preceded by a rod equipped with a collar housing a radioactive element (Lagasse et al., 1997). A detector capable of sensing the presence of the radioactive element is used to track the movement of the collar. This detector is lowered inside the rod from the bridge deck, through a guide tube. Due to

environmental concerns regarding the use of a radioactive element on the collar, this device was abandoned in favor of a similar device that relies upon a magnetic element installed on the collar (Lagasse et al., 1997). To monitor the location of the collar, two variations of the MSC device were developed and patented (Richardson et al., 1996). In the first embodiment, the location of the magnet is detected by lowering a magnetic switch on a chain from the bridge deck inside a guide tube that is connected to the rod mounted in the riverbed, see Figure 2.2. When this switch nears the collar, the field from the collar's magnet trips the switch. The position of the chain at this point is then recorded, and thus, by knowing the chain length, the depth of scour can be determined. This approach however, is difficult to automate for remote monitoring applications. To overcome this weakness, a second version was developed that equipped the rod with magnetic switches located every 1.0 ft along its length. As the collar moves down the rod, these switches are tripped; the time and location of each tripped switch during an event is recorded by a data acquisition system located on the bridge. Typically, a 0.5 ft magnet is fixed to the collar, resulting in scour depth measurements at intervals of +/- 0.5 ft (Lagasse et al., 1997).

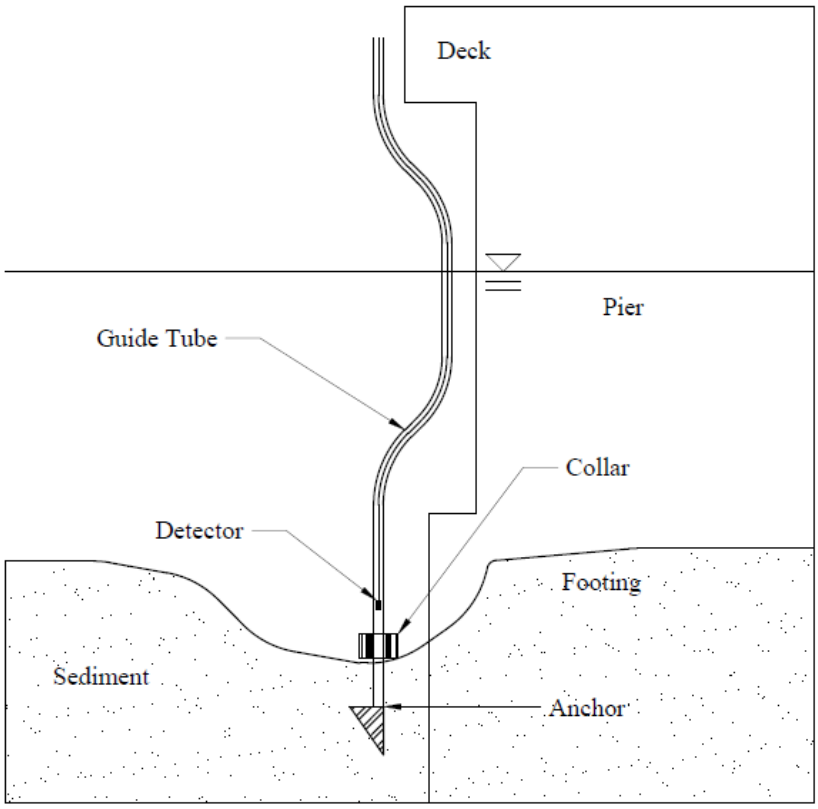

Figure 2.2: Example of a magnetic sliding collar installation. This figure is adapted from Richardson et al. (1996) and Nassif et al. (2002), and shows the first embodiment of the MSC device.

MSC rods were deployed for scour monitoring as part of the NCHRP 21-3 Research Program, as well as in separate projects by the New Jersey and Indiana State Departments of Transportation. The first embodiment of the MSC device was installed at two bridges, one located in Colorado and one in New Mexico. A 4.92 ft scour event was measured with this device in Colorado while a 2.82 ft scour event was recorded in New Mexico (Lagasse et al., 1997). Two automated MSC devices were installed on the Kersey Bridge Abutment in Colorado and the Nassau Sound Bridge in Florida. A 1.97 to 2.95 ft scour event was recorded with the automatic device in Colorado while no scour was

observed during the Florida field tests (Lagasse et al., 1997). Additional tests were conducted in Michigan, Minnesota, and Texas by various state Departments of Transportations or the FHWA as part of the broader NCHRP project. Though various installation issues were encountered, scour events were measured in these additional field tests from 0.787 to 4.92 ft in depth. Automatic MSC devices were also installed on two bridges in New Jersey, which recorded a 1.48 ft deep scour event on the Passaic Bridge (Nassif et al., 2002). Cooper et al. (2000) discussed the performance of both MSC and sonar devices on two bridges in Indiana. During the program, several scour events were recorded with the MSC collars ranging from 0.5 to 1.48 ft in depth, which were also typically well correlated with the sonar readings taken during the same period.

During the field operation of the first MSC embodiment in Colorado, debris impacted the guide pipe needed to route the detector from the bridge deck, through the water column, and to the rod. This damage, however, did not prevent the operation of the device (Lagasse et al., 1997). In the New Jersey study, subsequent analysis of the available data revealed that while the MSC collar was able to record scour events, the success of the entire campaign was highly dependent upon a reliable data logger (Nassif et al., 2002). In the Indiana study, the most significant issue encountered in the field was the survival of the sensors (Cooper et al., 2000). At the Wabash River site, the MSC rod was lost entirely, which was attributed to debris colliding with the sensor. At the Wildcat Creek site, though the rod survived debris damage, the cable to the data acquisition system was damaged resulting in the loss of the data. Additionally, during the development of the MSC device, it was reported that the space between the collar and the

rod could fill with sediment, causing the collar to stick and give a false reading (Lagasse et al., 1997).

Based upon these results, the main channel condition that can affect the survivability of MSC devices is the presence of debris. As indicated, several devices or the cable connecting the rods to the data acquisition units were damaged. An additional problem with a collar based system is that the collar/rod clearance must be controlled to prevent sediment from impeding the collar's movement. Finally, as the collar rests on the bed surface, if the scour hole were to refill with additional material after the high flow event, the collar would become submerged. Any subsequent scour events with a magnitude less than the event that submerged the collar would not be recorded.

2.3.4 Sonar/Fathometer

A sonar based scour monitoring system consists of a sonar transducer (or an array of transducers), often called fathometers or echo sounders, and the associated data collection and processing equipment. A typical installation is shown in Figure 2.3. Sonar transducers employ piezoelectric crystals that are either connected to a membrane or diaphragm. When an electric potential is applied across the crystal, an electric field is induced, which causes strain and thus, displacement of the crystal and the membrane. This field is then cycled, yielding an acoustic wave that is generated in the surrounding fluid (Jaffe and Berlincourt, 1965; Guo et al., 1992). As the sound wave propagates through the channel, it will encounter various surfaces and objects that will cause a portion of the signal to reflect, called the echo signal. The time between when the original signal was emitted and when the echo is received, t_{ER}, can be recorded. Typically, this

measurement is made at the point at which the pulse is emitted, called the zero line (Hayes and Drummond, 1995). During this time, the signal traveled twice the distance to the object, D, as it traveled out to the object and back to the receiver. This wave travels at the speed of sound, c, in the water. From the measured travel time, the distance D can be calculated, as shown in Equation (2.1) (Burczynski, 1982).

$$D = \frac{c \cdot t_{ER}}{2} \tag{2.1}$$

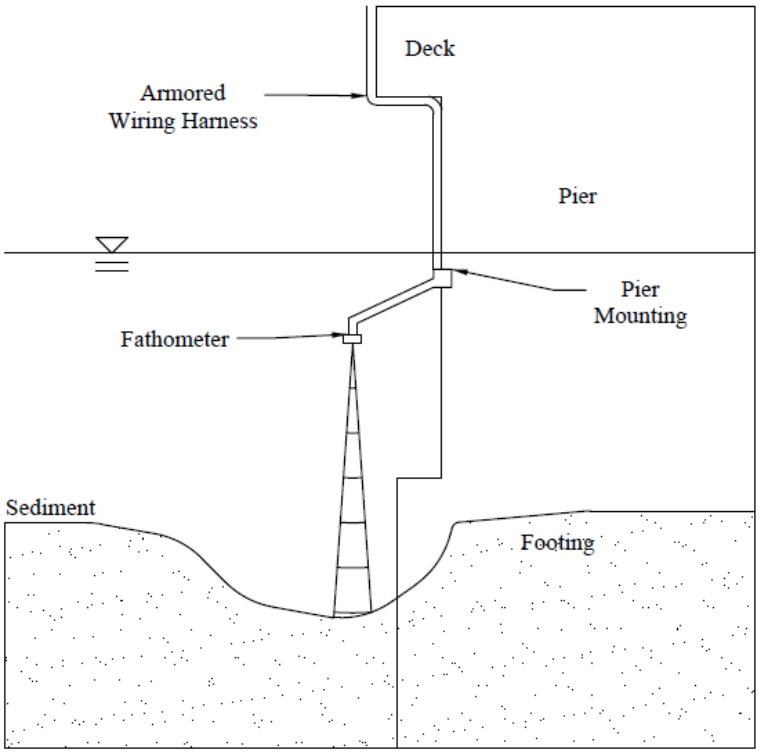

Figure 2.3: Typical sonar system installation. Based upon Nassif et al. (2002).

The resolution of the sonar system is a function of pulse duration, t_D, the time during which the transducer emits its pulse, and the pulse frequency, f. The effect of the pulse duration can be determined from Equation (2.1), by replacing the echo time with

the pulse duration. For example, if the speed of sound in water is 4920 ft/s and the pulse duration is 0.1 milliseconds, the resolution of the device is limited to 0.25 ft. The ability to resolve the riverbed features is also a function of the frequency of the acoustic wave. For example, if the pulse consisted of only a single complete cycle of vibration of the transducer, then the resolution would become a function of the period of the wave. The period of the wave is inversely proportional to the frequency, thus as the frequency increases, the minimum size of an object that can be resolved by the device decreases. For example, a 50 kHz signal can resolve objects greater than 0.6 inch where as a 200 kHz signal can resolve an object down to the size of 0.14 inch.

While increasing the sonar frequency improves the ability to resolve small-scale structures in the riverbed, it also affects the attenuation of the sonic pulse. Attenuation occurs due to the scattering and absorption from the presence of particles in the flow (both suspended particles and the fluid particles) as well as due to friction (Burczynski, 1982; Urick, 1975). As the frequency increases, the attenuation increases, and the amount of signal returned to the transducer is reduced, limiting the distance of the sonar to the bed.

Sonar systems were evaluated as part of several research projects. Lagasse et al. (1997) instrumented several bridges with fathometers, including the Orchard Bridge in Colorado, the San Antonio Bridge test site in New Mexico, Johns Pass Bridge in Florida, and the Kersey Bridge Abutment in Colorado. During these field measurements, the sonar units recorded scour events of 0.75 ft, 3.94 ft, 2.98 ft, and 1.64 ft, respectively, as well as refill at some of the sites. The Florida site also showed that the sonar system

could operate in a marine environment and flows generated during Hurricane Opal. In a study for the New Jersey Department of Transportation, Nassif et al. (2002) reported on the performance of sonar systems on two bridges. During the 23 months of testing, two scour events were observed; the initial event resulted in the development of a 1.64 ft deep scour hole, followed by aggradation of material that refilled the hole within 2 hours. A subsequent scour event of approximately 0.98 ft in depth was observed. Hunt (2005) reported on the development and installation of several sonic fathometer systems in New York and in the District of Columbia. The channel depths made installation of MSC unfeasible. Though some of these devices had been operational for seven years at the time of the report, the reliability of the data or any conclusions regarding the magnitude of scour events were not discussed. Mason and Sheppard (1994) collected data from a sonar monitoring system installed at the Herbert C. Bonner Bridge in North Carolina. The system consisted of 16 different sensors installed 4.92 ft from the channel bed and 5.9 to 13.12 ft below the water surface. During Hurricane Emily, the system recorded the development of a 1.97 ft scour hole followed by refill, as well as 3.28 ft of erosion and refill of the main channel. The performance of the system was also compared with several calibration measurements taken by divers at the measurement sites. The results from the sonar systems and the divers were well correlated. In addition, De Falco and Mele (2002) reported on the performance of two sonar scour monitoring systems installed at two separate railway bridges in Italy. Their results indicated scour hole developments of 4.92 to 6.56 ft at the Mezzana Corti Bridge and 2.95 ft at the Borgoforte Bridge. These results were then compared to prediction models with a 7% difference for the Mezzana

Corti Bridge and 10% difference for the Borgoforte pier between the measured and predicted scour depths. Finally, Holnbeck and McCarthy (2011) reported on the performance of a USGS sonar monitoring system at the I-90 Bridge over the Blackfoot River in Montana. A downstream dam was removed from this reach in 2008 resulting in an increase in the flow velocity through the bridge contraction. To monitor the performance of several scour countermeasures and to record the overall bed/foundation health, four sonar fathometers were installed on the two piers in the channel. A scour event of 3.94 ft was observed, which was later confirmed by a follow-up survey.

Sonar fathometers have shown the ability to record both maximum scour and refill, it is necessary therefore to evaluate their performance under typical natural channel conditions. Since the operation of the sonar device relies upon measuring the time between signal emission and echo reception, any false echoes recorded by the device can lead to errors in the measurements. These false echoes can occur due to air entrainment or debris in the channel. In addition to the field test discussed previously, Lagasse et al. (1997) also conducted laboratory tests and showed that sonar fathometers are susceptible to air entrainment, which prevented the sonar device from determining the depth to the bed. Similarly, DeFalco and Mele (2002) reported that during their field campaign, the sonar results often showed peaks in the time history data of approximately 16.4 ft in depth, which were not correlated to scour but instead to the presence of air bubbles, sediment load, and turbidity in the channels. Holnbeck and McCarthy (2011) reported that air entrainment and channel turbulence was responsible for failure of three out of the four installed sensors. Debris in the channel can also provide false echo signals, leading

to measurement errors. To overcome this problem, Nassif et al. (2002) reported on the development of a debris detection algorithm that helped to eliminate false readings. In addition to the false readings that can occur from debris, sonar devices are also susceptible to debris damage. Cooper et al. (2000) reported that the sonar instrument itself was susceptible to debris, as was the cable connecting the sonar to the data acquisition system. Indeed, in one case, the sensor and cable were completely removed from the pier due to debris impacting the hardware. In addition to debris damage, the environmental conditions that affect the speed of sound within the channel, including water temperature and salinity, can also affect the performance of sonar systems. At the John's Pass Bridge site in Florida, Lagasse et al. (1997) reported that it was necessary to correct the measured signal, with an average correction of 1.51 ft, for these two parameters. Additionally, since the sonar pulse expands with distance from the transducer, the beam width may exceed the scour hole dimensions. It is then possible to have multiple echoes from the edge of the hole, the sides of the hole, and the bottom of the scour hole itself. As part of the NCHRP 21-3 project, testing was conducted on the ability of a sonar unit to observe the scour hole. This was accomplished with a Lowrance X-25 sensor subjected to unit steps in depth in a series of tests in a swimming pool. During the analysis, it was determined that the sonar unit recorded the depth at the center of the beam and not an average over the entire beam width (Lagasse et al., 1997). Finally, low levels of reliability from some sonar fathometer installations have been attributed to electronic interference issues and cross talk between multiple sensors (Mason and Sheppard, 1994).

As indicated previously, the sonar systems can provide reliable measurements of the river bottom including the maximum scour and refill during peak flow periods. Sonar systems, however, are also susceptible to the environmental conditions in the channel (i.e., salinity, temperature of the water, the level of channel turbulence, the amount of air entrained, electronic noise, debris damage, false echoes, and the size of the scour hole relative to the sonar beam). Some of these parameters can be accounted for either by calibration methods or by measuring additional channel parameters, e.g., salinity and temperature. Other factors, such as debris, can cause device failure directly. Despite these complications, sonar devices are one of the most commonly deployed units because of their ability to record both maximum scour and refill.

2.3.5 Time Domain Reflectometry

A time domain reflectometry (TDR) scour monitoring system consists of a coaxial cable and scour probe connected to an electro-magnetic (EM) pulse generator and signal analyzer. The latter component is referred to as the TDR device itself, which emits a sharp rising voltage pulse into the cable. As the pulse travels along the cable it encounters various changes in material surrounding the cable that cause reflections, which then travel back to the pulse emitter. The scour probe typically consists of two or three metal rods of various thicknesses separated by a non-conducting material. The device employed by Yankielun and Zabilansky (1994) consisted of two black iron pipes of 1.2 inch in diameter and 2.82 ft in length with the ends held together with Plexiglas clamps. Yu and Yu (2011) used commercially available soil moisture probes, such as the Campbell Scientific CS605, consisting of three probes of 0.4 inch in diameter and 0.67 ft

in length, spaced 0.22 ft apart. The TDR pulse emitting devices used in the literature vary from the Tektronic 1502 B, 1503C TDRs to the Campbell Scientific (CS) TDR100. Of these instruments, the currently commercially available unit is the CS TDR100, which employs a rising voltage pulse of 250 mV in amplitude that lasts for 14 microseconds. The rise time of the signal is less than 300 picoseconds (Campbell Scientific, 2011).

The EM pulse travelling through the TDR cable and the scour probe will reflect a portion of the emitted pulse at each change in interface. The first reflection occurs at the cable/probe interface. If the impedance of this interface is poorly matched, a large portion of the signal can be reflected back to the emitter, preventing a sufficient portion of the signal from entering the probe (Yankeilun and Zabilansky, 1999). Additional reflections will occur at the air/water interface (should it occur), at the water/sediment interface, and the end of the probe, see Figure 2.4.

As with a sonar device, the velocity of the EM pulse through the scour probe depends upon the material surrounding the probe. The EM pulse is affected by the apparent dielectric constant, K_A, of the media, through which it travels. In some media the pulse will travel faster than in others. The actual travel speed of the pulse, v, is the ratio of the speed of light in a vacuum, c_L, to the square root of the dielectric constant, as shown in Equation (2.2) (Yankeilun and Zabilansky, 1999).

$$v = \frac{c_L}{\sqrt{K_A}} \tag{2.2}$$

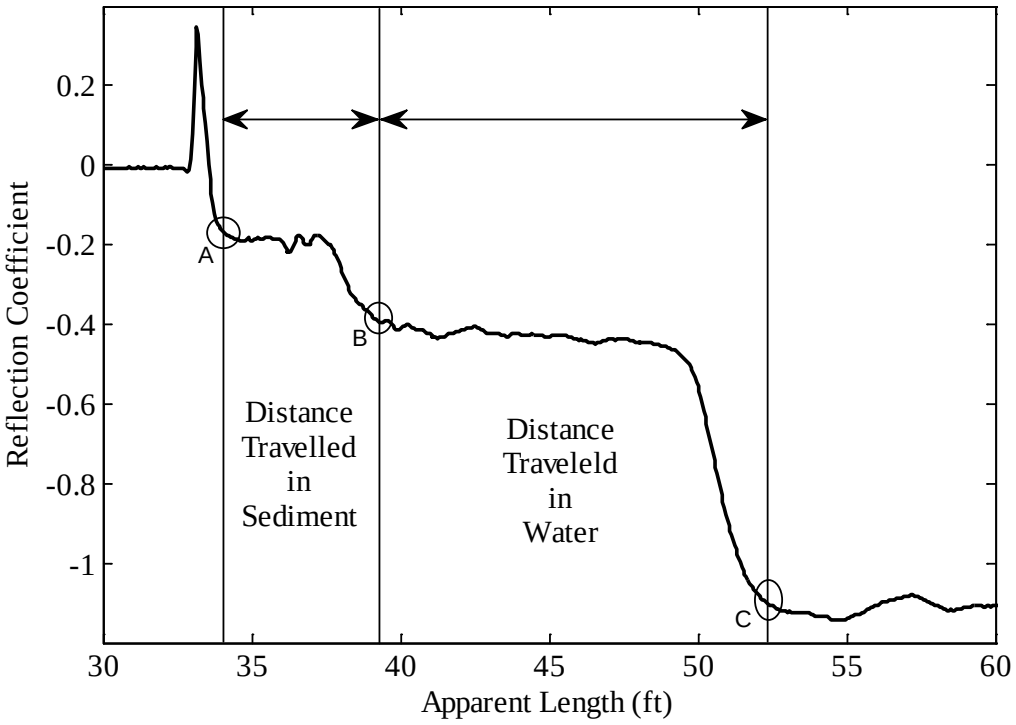

Figure 2.4: Typical TDR waveform.

If the speed of the pulse is known, then the depth to the sediment can be determined by analyzing the TDR signal for the time when the reflection occurs from the start of the probe, 'A', the water/sediment interface, 'B', and the end of the probe, 'C', as shown in Figure 2.4. For each point in the waveform in Figure 2.4, the pulse travels from the TDR emitter, to the point of the reflection, and then the reflected wave travels back to the TDR unit, covering twice the physical distance to this interface. Therefore, assuming that the wave travels at the speed of light, then the product of one half of the travel time from points 'B' to 'C' in Figure 2.4, and the speed of light represents the distance covered during this period, known as the apparent length of the probe in the water, L_{A1}.

The length is called the apparent length since it assumes that the pulse traveled at the speed of light. A similar expression for the apparent length of the probe in the sediment, L_{A2}, is computed from the product of the speed of light with one half of the travel time between 'A' and 'B'. Both of these apparent lengths are related to the actual length by the apparent dielectric constant of the water and saturated sediment, $K_{A,W}$ and $K_{A,S}$ respectively, (Yankeilun and Zabilansky, 1999), as shown in Equations (2.3) and (2.4).

$$L_1 = \frac{L_{A1}}{\sqrt{K_{A,W}}} \tag{2.3}$$

$$L_2 = \frac{L_{A2}}{\sqrt{K_{A,S}}} \tag{2.4}$$

While it has been argued that the apparent dielectric constant for water has a narrow range, the value for the sediment is dependent upon the nature of the riverbed and cannot be known *a priori*. Therefore, for the three unknowns, L_1, L_2, and $K_{A,S}$, it is necessary to add an additional equation. Two equations are available, either based upon the total apparent length, L_A, or the physical lengths, L, of the probe, as shown in Equations (2.5) and (2.6). The apparent length, L_A, is based upon the travel time between 'A' and 'C' and the speed of light.

$$L_A = L_1\sqrt{K_{A,W}} + L_2\sqrt{K_{A,S}} \tag{2.5}$$

$$L = L_1 + L_2 \tag{2.6}$$

In the method outlined above, an apparent dielectric constant for the water in the channel must be assumed. Yu and Yu (2011) developed another method that calibrates

the response of the TDR signal/system for the conditions expected in the field. Their method is based on the volumetric mixing model for dielectric materials proposed by Birchak et al. (1974), which defines the apparent dielectric constant of the mixture, K_M, as the sum of the product of the volume fractions of each layers, f_i, with the apparent dielectric constant for that layer, K_i, as shown in Equation (2.7).

$$\sqrt{K_M} = f_1\sqrt{K_1} + (1 - f_1)\sqrt{K_2} \tag{2.7}$$

Yu and Yu (2011) extended this model to the water and saturated sediment surrounding a TDR probe by replacing the volume fractions with the lengths of each layer, which is valid assuming that the EM pulse passes through the same interface area in each layer. To use the model, as shown in Equation (2.8), the mixture dielectric constant is needed, which can be found from the TDR waveform as the ratio of the apparent length to the physical length of the total probe.

$$L\sqrt{K_M} = L_1\sqrt{K_{A,W}} + L_2\sqrt{K_{A,S}} \tag{2.8}$$

Using Equation (2.6), Yu and Yu (2011) manipulated Equation (2.8) into a linear form that can be calibrated to the specific sediment in place in the riverbed, the modified form of which is shown in Equation (2.9), where X_R is the ratio of the sediment length to the total probe length.

$$\frac{\sqrt{K_M}}{\sqrt{K_{A,W}}} = X_R\left(\frac{\sqrt{K_{A,S}}}{\sqrt{K_{A,W}}} - 1\right) + 1 = aX_R + b \tag{2.9}$$

Using this model, it is possible to measure the slope of Equation (2.9) experimentally by using sediments similar to those in the riverbed as a calibration test.

Such measurements require measuring the apparent dielectric constant of the water and the saturated sediment for different layer lengths. Yu and Yu (2011) also developed a method to calculate the slope of the Equation (2.9), again using the Birchak et al. (1974) volumetric model, but here they applied it to the saturated sediment only, as shown in Equation (2.10). The additional parameters introduced include the porosity of the sediment, n, and the apparent dielectric constant of the dry sediment, $K_{A,DS}$. This model assumes that the porosity and apparent dielectric constant of the dry sediment are known for the riverbed material from sediment surveys of the riverbed.

$$\sqrt{K_{A,S}} = n\sqrt{K_{A,W}} + (1-n)\sqrt{K_{A,DS}} \tag{2.10}$$

In addition to providing the soil/water interface location, the measurements made with a TDR system can also reveal information about the soil properties. Topp et al. (1980) showed that the volumetric water content, θ, of the soil/sediment could be calculated from the dielectric constant, as shown in Equation (2.11). Similarly, Drnevich et al. (2001) showed that the gravimetric water content, w, could also be determined from the measured dielectric constant of the sediment layer, provided that the dry soil density, ρ_D, is known, as shown in Equation (2.12). They also hypothesize that for most soils, the values for the constants a and b in Equation (2.12) are approximately 1 and 8, respectively. These two water content relationships are related as shown in Equation (2.13), where ρ_W is the density of water.

$$\theta = 4.3\cdot10^{-6}K_A^3 - 5.5\cdot10^{-4}K_A^2 + 2.92\cdot10^{-2}K_A - 5.3\cdot10^{-2} \tag{2.11}$$

$$w = \frac{1}{b}\left(\frac{\rho_W}{\rho_D}\sqrt{K_A} - a \right) \tag{2.12}$$

$$w = \theta \frac{\rho_W}{\rho_D} \tag{2.13}$$

The laboratory and field performance of TDR probe under various environmental factors must also be evaluated. Yankielun and Zabilansky (1999) validated their method, Equations (2.5) and (2.6), in the laboratory for several sediment types ranging from sand to pea gravel to cobble stones. The results from the experiments conducted revealed that for depths up to 3.28 ft, the linearity of the results were within 5-7% of the independently measured scour depth. Similarly, in the tests conducted by Yu and Zabilansky (2006), the TDR and independently measured lengths of the sediment were well correlated, with a linear fit through the data yielding an R^2 value of 99 %. Using the second measurement method, Equation (2.9), Yu and Yu (2011) showed that for a saturated sediment dielectric constant of 6, the slope measured experimentally and the slope calculated using Equation (2.9) were within a 5%. In addition to the measured sediment depth, Yu and Yu (2006) also tested the performance of the methods for predicting the soil properties for volumetric and gravimetric moisture contents in the range of 0.023 to 0.145 and 0.014 to 0.092, respectively, and found reasonable agreement between the TDR and independently measured parameters. The listed mean squares of the errors were of the order of 10^{-3} with equally small standard deviations of the errors listed. An analysis of these results determined that the percentage error for the values listed varied greatly for different soil conditions from as little as less than one percent to as much as several tens of percent and beyond. While the available literature on TDR systems performance in laboratory and

simulated cases is extensive, there is limited field performance data. The US Army Corps tested seven TDR probes to record the impact of ice formation on channel stability at the Highway 16 Bridge site in Missouri, as reported in Zabilansky and Ettema (2002) and Ettema and Zabilansky (2004), and observed several instances of scour and refill on the order of 0.5 ft.

While the experimental results have shown primarily that the TDR device works well in the laboratory, it is necessary to consider conditions in the field that can impact the performance of the method. These include the variability of the sediment dielectric constants present in natural channels, and the impact of water salinity and temperature. To consider the impact of the riverbed conditions on the 2^{nd} post processing method, Equation (2.9), it is possible to evaluate the impact of the dry sediment dielectric constant on the results. Yu and Yu (2011) used a value of 6 for the dry sediment, though the range can vary from 3 to 8 (Yankielun and Zabilansky, 1999). If the full range of the apparent dielectric constant of the dry sediment is used, the slope can vary by 6 to 11%, versus the data from Yu and Yu (2011). Such discrepancies indicate that in order to use the linear slope model, the system must either be calibrated onsite with the actual sediment in the riverbed, or samples must be obtained so as to determine the actual value for the dry sediment. Also, given that the scour hole refill typically consists of a material of a different porosity and sediment type, the ability to record significant refill with the linear fit method should be verified experimentally. In addition to the impact of sediment, TDR results can also be influenced by the water conditions. Yu and Yu (2011) tested the performance of the TDR probe in saline solutions up to 750 parts per million (ppm) of

sodium chloride. Based on the tests, the TDR results typically fell within 5% of the independently measured results. However, some conditions exceeded this 5% error range. It should be noted that the salinity range tested is limited, since in estuarine environments the salinity can vary from a yearly average of approximately 50 to 17,500 parts per million concentration (USGS, 2006a; USGS, 2006b), well above the range tested in the laboratory. The temperature effect can be evaluated theoretically by adjusting the dielectric constant for the temperature in the channel (Stogryn, 1971). For example, if a 2.62 ft scour probe is buried 2.3 ft deep in sediment, a temperature change of 68 °F may cause an error of 7%.

Though TDR systems can provide detailed information about the riverbed condition including the water/sediment interface, the soil dielectric constant and the volumetric constant, water and sediment based parameter must either be known or assumed. These assumptions, whether they are for the dielectric constant of the sediment or the water, can result in errors between 5 and 10%.

2.3.6 Fiber Optics

Fiber optic sensors have been used for scour measurement in recent years, consisting of either wavelength or intensity based measurement methods. Wavelength based devices are the most common type of fiber optic sensor employed for scour analysis. These include the devices developed by Ansari (2010) and Lin et al. (2004; 2006), which are discussed after a brief overview of the physical operation of wavelength and intensity based fiber optic methods. The wavelength based sensors consist of Fiber Bragg Gratings (FBG). The FBG consists of a length of fiber in which a series of periodic

changes to the refractive index of the fiber core have been made. When broadband light is incident to the FBG, based upon the pitch of the FBG, the reflected light is narrowband with a discrete, measureable wavelength. The reflected wavelength then shifts when the FBG is strained, and is correlated to the amount of strain in the fiber, as shown in Equation (2.14) (Guemes and Menendez, 2006; Manzoni et al., 2011a). The wavelength shift, $\Delta\lambda_R$, is related to the original reflected wavelength and the amount of mechanical and thermal strain in the fiber, ε_M and ε_T, respectively. A gauge specific constant, K_G, is used to calibrate the device. Additionally, it is necessary to consider the thermal strain in the fiber, given by the linear expansion coefficient of the refractive index, α_F, and the temperature change, ΔT.

$$\frac{\Delta\lambda_R}{\lambda_R} = K_G\left(\varepsilon_M + \varepsilon_T\right) + \alpha_F \Delta T \tag{2.14}$$

In contrast to measuring the reflected wavelength, intensity based measurements compare the amount of light emitted into the fiber relative to the amount reflected back from the fiber termination. Based upon Fresnel's Law, it is possible to predict the reflection index, R, based upon the refractive index of the core and the external environment at the fiber termination, n_{CORE} and n_{ENV} respectively, as shown in (2.15) (Guemes and Menendez, 2006).

$$R = \left(\frac{n_{CORE}/n_{ENV} - 1}{n_{CORE}/n_{ENV} + 1}\right)^2 \tag{2.15}$$

In order to apply these two techniques to monitor scour, several researchers have developed methods that utilize fiber sensors in instruments buried in the riverbed. FBG

based devices will be reviewed first, followed by intensity based methods. Ansari (2010) developed an instrument consisting of a buried rod instrumented with FBG sensors acting as dynamic strain gauges. The rod vibrates at a certain natural frequency depending upon the depth of burial, which can be predicted based upon material and geometric properties of the rod and surrounding soil. As the scour hole develops, the length of rod that is buried beneath the riverbed will decrease and the natural frequency of the rod will change. In order to relate the change in natural frequency to the amount of exposed rod, the method proposed by Ansari (2010) relies upon the use of a finite element model for calibration. Lin et al. (2004; 2006) proposed several additional measurement techniques that employ FBG sensors. In the first configuration, sensors are attached at discrete points along a flexible rod buried in the riverbed. As the rod is uncovered due to scour, it deflects with the flow, inducing a strain in the FBG sensors located further down the rod. The depth can then be recorded by the distribution of strain along the rod. In the second configuration, a series of thin, cantilevered plates are distributed on a rod covering the length of the pier. The deflection of the plates is greater in the flow than in the sediment, thus the scouring process can be recorded by monitoring the time history of the strain distribution along the rod. A modified version of the second device was developed by Lin et al. (2006) and deployed on bridges in Taiwan. This modified approach consists of encasing the FBG sensors in a button housing that deflects due to the water pressure, causing strain on the FBG. The arrays of FBG units are housed within two concrete-steel tubes (CSTs) for protection of the fiber. By measuring the strain of each FBG along the

length of the CSTs, it is possible to determine which positions are surrounded by water, and therefore it is possible to locate the riverbed surface.

In addition to the wavelength based devices, a scour monitoring device that exploits the intensity based method was proposed by Isley et al. (2006) and consists of a rod with multiple fibers embedded within. These fibers terminate into the surrounding media at discrete points along the length of the rod. By monitoring the intensity of the light reflected back in each fiber, it is possible to distinguish whether the material surrounding each fiber termination is water or sediment.

Considering the experimental performance of the FBG units, Ansari (2010) reported on both laboratory and field results of the dynamic FBG based method that monitored the natural frequency of a buried rod. The laboratory tests were conducted in a tank with a sediment layer submerged in flowing water, circulated by a pump. Bed material was removed and deposited from the region surrounding the rod to simulate scour and refill, which was measured by the rod and independently by a fixed, graduated ruler. Based upon the measured results, the correlation coefficients (R^2) of the rod based to actual scour hole depths were 0.89 and 0.96 for the degradation and aggradation process, respectively. Two short term field tests were also conducted, the results of which indicated that the device was able to resolve the riverbed surface location to within 1.0 inch (Ansari, 2010).

Laboratory and field experiments were conducted on the various systems developed by Lin et al. (2004; 2006). The results for the cantilevered rod approach revealed that the amount of strain recorded by an FBG, as it was exposed, resulted in a

step change in the strain signal; however this change was small compared to the apparent noise in the signal. For the cantilevered plate method, the laboratory results indicated that the presence of flowing water around the plate resulted in a step change of 6.56×10^{-11} ft in the reflected wavelength, while the increase in strain due to scour only added an additional 1.64×10^{-11} ft, again resulting in a small signal-to-noise ratio. Lin et al. (2004) reported on the performance of the cantilevered plate based FBG system during the I-Li Typhoon in August of 2004. However, only wavelength shifts were reported and neither the actual scour depths were measured, nor any attempt was made to correlate the FBG results with an independent scour measurement. Lastly, Lin et al. (2006) also reported the performance of the CST based method during Typhon Aere in 2004. One CST was installed upstream of pier 12 and an additional unit was located downstream of the same pier on the Dadu Bridge over the Wu River in Taiwan. During Typhoon Aere, the upstream CST recorded the development and refill of a 9.8 ft scour hole while the downstream unit recorded a 1.64 ft scour hole. As with the other field installation, no independent scour monitoring device was deployed to verify these results. Lastly, for the intensity based scour monitoring technique, Isley et al. (2006) reported the results of various laboratory experiments. The results showed that while the device could distinguish if the surrounding material was water or sediment, it was not able to distinguish the sediment/water interface when the water was a turbid mix.

Performance data for the various fiber optic based scour monitoring devices is limited, thus evaluating the reliability of the device in changing environmental conditions in the field is not possible. However, the potential impacts that numerous conditions

could have on the performance of the various fiber optic based scour monitoring methods can be examined. Beginning with the natural frequency based method proposed by Ansari (2010), the main weakness of the approach lies in the reliance upon a finite element model to correlate the natural frequency to the depth of burial. Since the riverbed material will change from site to site (and even within a site) the accuracy of the finite element model for each installation location must be assured before the results can be deemed reliable. Additionally, the natural frequency of the rod can change for reasons unrelated to the development of a scour hole, such as temperature changes of the rod or water. Thus, the monitoring of the natural frequency to determine the scour depth is complicated. Similarly, the responses of the FBG based methods proposed by Lin et al. (2004; 2006) were shown in the laboratory experiments to be sensitive to the flow temperature. Additionally, the cantilevered beam method will have limited performance during a refill event, since it will remain in its deflected shape. Finally, as with most rod based devices, any instrument located in the channel has the potential to suffer from debris impact damage. Given the protection provided by the CST housing, it is likely that this device could withstand field deployment for long-term monitoring campaigns.

Overall, both the laboratory and field performance data suggest that it is possible to measure scour with fiber optic techniques. It is possible to develop devices that will relate the strain on the sensor to the change in the bed conditions. These devices are subject to debris impact damage, as are other rod based devices. However, it is possible to provide additional protection, as with the CSTs. The natural frequency based method proposed by Ansari (2010) is also dependent upon the accuracy of the field calibration

and potentially the temperature. Lastly, the intensity based methods fail to perform in turbid water, a common characteristic of natural channels.

2.3.7 Temperature Measurements

Temperature variations across a riverbed have also been used to measure the water/sediment interface and thus, scour. Camp et al. (1998) developed a thermocouple based scour monitoring system consisting of a series of thermocouples located every 2 inches along a partially buried rod. The device operates on the premise that the water temperature in the saturated sediment is at a consistently lower value than the water in the river. Thus, by measuring the temperature gradient along the length of the rod, it is possible to determine the location of the riverbed, and the amount of scour. In addition to the thermocouple based measurement methods, a method developed by Manzoni et al. (2011a; 2011b) utilized FBG sensors as thermocouples instrumented along the length of a rod buried in the sediment. A heating element located next to each FBG on the rod is activated periodically, leading to a temperature change within the fiber. The fibers in the sediment are surrounded by stagnant, saturated sediment and the only source of heat loss is via conduction into the surrounding media. For the FBGs in the flow, the dominant heat loss mechanism is accomplished via convection. As such, the rate of heat loss in the flow exceeds that in the sediment. Therefore, for a uniform heat load, the steady state temperature change between unheated and heated states in the sediment will exceed the temperature change in the portion of the rod in the flow.

The thermocouple based method, developed by Camp et al. (1998), was tested in laboratory conditions and in a short term field operation. During the laboratory tests, the

rod was partially buried in a tank of sediment while heated water flowed past the partially exposed upper portion of the device. The thermal gradient along the length of the rod was measured and revealed that thermal diffusion from the flowing water into the bed only occurred in the upper 2 inches of the sediment. Thus, by observing the location of the largest thermal gradient, it was possible to determine the location of the water/sediment interface. Additionally, as sediment was removed, the thermocouples recorded a temperature change from that of the sediment to that of the water. A field unit was also deployed and revealed a fluctuating time history for the thermocouples that corresponded with the atmospheric temperature fluctuations. The daily variation in the thermocouples located in the riverbed was of the order of 34.7 °F, while the thermocouples in the flow varied from 41 to 45.5 °F (Camp et al., 1998). Despite this variation, it was still possible to determine the presence of the water/sediment interface and thus monitor scour.

Manzoni et al. (2011a; 2011b) also reported the experimental verification in the laboratory of the heat load based method. They observed that for heat loads greater than 3.05-4.57 W/ft, the resulting temperature change was large enough to be detected, with a 95% confidence, and that the uncertainty in the temperature difference measurements was ±35.1 °F. The FBG sensors were also capable of recording the time constant associated with the transient temperature change that occurred at the start of the heating cycle. The laboratory results showed that for flow rates of 1.3 ft/s, the time constant for the FBGs in the sediment was between 9 to 14 s while the time constant for the FBG sensors in the flow was 4-6 s, for 1.52-15.24 W/ft. Thus, it was shown that heat load based method also

provides a means of recording the water/sediment interface and could therefore monitor the development of a scour hole.

The research on temperature based scour measurements to date has focused on evaluating the feasibility of the methods, with limited data to evaluate the field performance. Despite this deficiency, it is possible to estimate the potential impact that changes in channel conditions will have on the two methods discussed earlier. The environmental conditions that often affect the performance of scour monitoring methods are debris, turbidity, and the presence of a live bed. As with all scour monitoring methods anchored in the channel bed, any debris that impacts the device can damage the measurement rod or its attached power source and cables. The two temperature based methods are sensitive to this factor. The two methods are expected to be insensitive to suspended sediment load in the channel. If the channel conditions, however, are such that there is a live bed, it is possible that the presence of this mobile sediment layer will affect the thermal gradient between the channel and the riverbed. Since the live bed temperature is likely to be between the riverbed and channel flow temperatures, the sharpness of the thermal gradient may be lessened, and thus the determination of the point of maximum gradient, may become less distinct as this region increases in size. Without the experimental data from either the laboratory or the field, it is difficult to determine how significant this impact could be on the results. In a similar manner, the presence of a live bed around the heat load based scour measurement rod may also affect the step change and the time constant for any measurement points in the region of moving sediment. It is expected that these values will be between the channel flow and the riverbed, again

making the exact point of the transition between the water and the sediment less distinct. Finally, for the heat load based method, the research to date has not considered at what minimum flow rates the temperature change between the sediment and the channel flow is still valid. Additionally, no attempt is made to correlate the flow speed with the time constant for the heated condition.

In summary, temperature based methods that exploit either the amount of heat lost or the natural temperature variation between the channel flow and riverbed are available to monitor scour. These devices have been tested in laboratory conditions to evaluate the feasibility of the methods. However, field data available to assess the performance of temperature based methods in natural channels is scarce. In addition, it can be anticipated that debris impact or the presence of a live bed may affect both temperature based measurement devices.

2.3.8 Piezoelectric Film Sensors

A novel sensor consisting of a flexible fin like structure attached to a rod has also been used to measure scour (Lagasse et al., 1997). A flexible piezoelectric film is attached to each fin that generates a voltage when subjected to the turbulent fluctuations of the flow past the rod, which can be measured by a standard voltmeter or data logger. An instrumented rod with multiple films attached on the downstream side is then buried in the sediment around a pier. The sensors in the flow will vibrate, generating a measureable voltage, which in turn indicates the water/sediment interface location, see Figure 2.5.

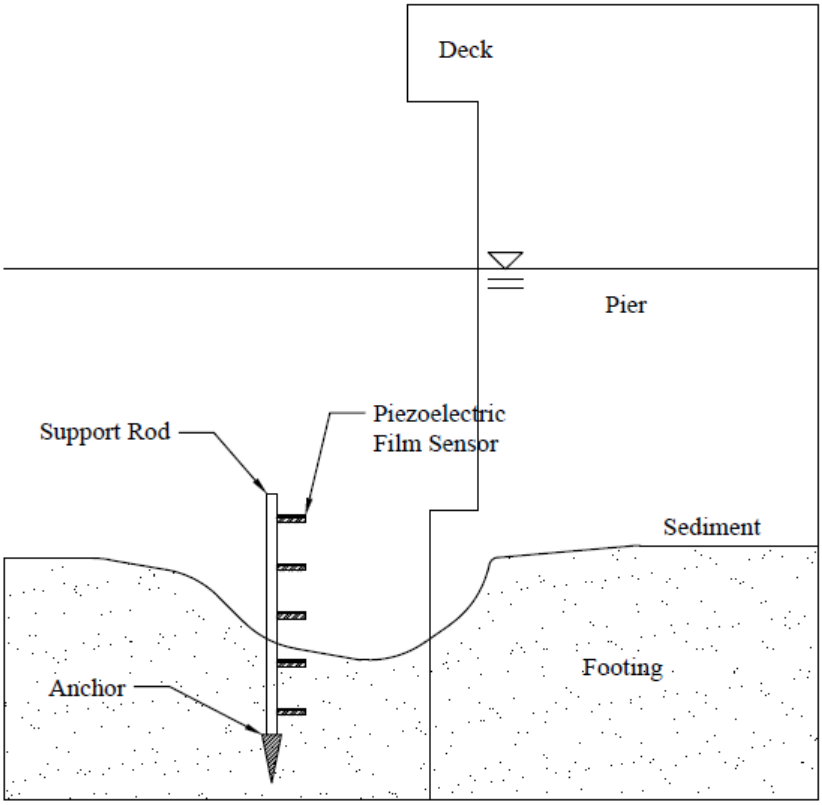

Figure 2.5: Piezoelectric film sensor. Based upon Lagasse et al. (1997).

During laboratory testing, several additional measures were undertaken to improve the long-term survival rate of the devices with the optimal configuration being to bond the film sensor to a section of flexible silicone tubing (Lagasse et al., 1997). The devices were also field tested at the Orchard Bridge and Sandy River sites in Colorado as part of NCHRP project 21-3. At the Orchard Bridge site, a rod was instrumented with six sensors spaced 6 inches apart for the bottom four sensors and 1.0 ft apart for the top two sensors. During the testing, voltage readings were observed from all the sensors. It was determined that the bridge structural vibrations led to movements of all of the piezoelectric films, which caused erroneous results. The Sandy River site revealed the

ability of the device to measure scour even after being hit by debris. The USGS did not indicate the scour depth during this event.

In terms of environmental factors that can affect the device, it has already been shown that structural vibrations of the bridge can influence the reliability of the results. In addition, the piezoelectric film can de-bond from the fin or the device itself can degrade over time, leading to a failure of the sensor. In addition, as with any rod-based device, they also suffer from susceptibility to debris damage. The overall conclusion of the NCHRP project 21-3 was not to use these devices for future field tests.

2.3.9 Mercury Tip Switches

A mercury tip switch system consists of commercially available mercury switches, with each switch consisting of small chambers housing two terminals. The chamber contains a small amount of liquid mercury and is attached to a buried rod. As the switch is rotated, gravity pulls the mercury around the chamber and either closes or opens the circuit between the two terminals. In the scour application, the initial position of the sensors is such that it is folded up against the rod. As the scour hole develops, these switches are exposed and fold down, opening the circuit. By monitoring the condition of each circuit on the rod, it is possible to determine the depth of maximum scour in the riverbed. Due to the deployment of the switch during a scouring event, it is only possible to record the maximum scour with this device since the switch is not returned to its neutral position by the refill of material into the scour hole.

The results of laboratory tests performed on this device indicated that the switch often tripped as the scour depth approached the sensor position, but before the actual

depth had reached the sensor (Lagasse et al., 1997). This is likely due to the buoyant force of the chamber pushing out on the layer of soil holding it in place. An additional disadvantage of this device is that it contains mercury, which is a hazardous substance and should not be released into the environment. Due to the limitations of this device and contamination potential, mercury tip switches were eliminated from further testing as part of the NCHRP project (Lagasse et al., 1997).

2.4 Distributed Scour Measurement Methods

2.4.1 Radar

In addition to TDR, other techniques are available that employ electromagnetic (EM) waves. Specifically, a Ground Penetrating Radar (GPR) system uses the EM waves similar to a sonar system that uses sonic pulses. As with the sonar method, the incident wave is reflected back. The radar system has emitting and receiving transducers, called antennae, to send and receive EM waves, typically designated Tx and Rx, respectively. This technique has been adopted from traditional non-destructive testing (NDT) and geotechnical surveys methods and applied to scour monitoring. Typical NDT testing on concrete or masonry send EM pulses with frequencies in the range of 500 MHz to 1 GHz, while geotechnical surveys employ frequencies in the range of 50 to 300 MHz, the main difference being the desired resolution of the reflected signals (Millard et al., 1998). For NDT, a higher frequency signal is used in order to increase the resolution of the Radar image at the cost of depth of penetration. Geotechnical surveys uses lower frequencies as determining the nature of various layers of soil/rock in the subsurface is more important that the resolution. Both ranges have been employed in scour monitoring applications

(Millard et al., 1998; Webb et al., 2000; Paczek and Haeni, 1995). As with the TDR system, the speed of propagation is governed by the dielectric constant of the medium through which the EM pulse is transmitted, see Equation (2.2). Thus, by knowing the time between emitting and receiving a pulse as well as the speed of light, the distance to the object that causes the reflection can be determined.

GPR can provide an image of the riverbed, recording depth as the unit is traversed across the channel. Typically this can be accomplished at rates of 3.28 ft/s for handheld units and up to 45.56 ft/s for vehicle based systems (Manzoni et al., 2011b). The reflections are processed by the GPR unit into depth values by first assuming the EM wave propagated with the speed of light. These initial images are then reprocessed into actual depth values by accounting for the dielectric constant of the channel flow. Unlike the TDR method, it is necessary to use an assumed dielectric constant of water and river bed material, since the actual dielectric constant is not determined as part of the post processing. Given the unknown dielectric constant below the river bed, any depth values below the water/sediment interface are only relative values and cannot be regarded as true depths. For a scour hole this is not a hindrance to the method since the depth can be determined directly as the EM wave only travels in the water column. This is not the case when the scour hole has been refilled with additional sediment. Therefore, it is only possible to qualitatively observe the presence of a refilled scour hole, the magnitude of which cannot be quantified exactly.

As mentioned previously, GPR systems have been deployed in NDT and geophysical site surveys. In order to evaluate the performance of GPS systems for scour

monitoring, several laboratory and field measurements have been conducted to assess their performance. Millard et al. (1998) conducted laboratory tests using GPR to measure scour holes around concrete piers and to profile the sub bottom of a refilled scour hole. Though the GPR recorded the profile, no quantitative measure of the precision was provided. Also, the presence of the concrete pier resulted in additional reflections, complicating the results during the laboratory testing. It was found that the nature of the refill material could complicate the profile of a refilled scour. If the infill and riverbed materials have similar dielectric constants, it is difficult to discern the presence of a refilled scour hole. In field surveys conducted in the Dee, Ribble, Severn, and Coln Rivers in the U.K, Millard et al. (1998) evaluated the performance of various GPR frequencies of the GSSI SIR-2 system, which varied from 300 to 500, 900 MHz and 1 GHz. The reported results indicated that 300 and 500 MHz are optimal due to increased attenuation at higher frequencies, reducing the strength of the reflected wave. A scour hole was observed around a local bridge pier on the River Ribble and was confirmed with a sonar fathometer survey. However, a quantitative comparison of the two depths was not provided. In a report on the performance of a GPR unit at measuring scour holes and riverbed profiles at ten bridges in Missouri, Webb et al. (2000) used equipment consisting of a GSSI SIR-10B GPR unit with 200 MHz and 400 MHz antennas, which were traversed across the channel either from the bridge deck or from a boat. Survey scans conducted at a rate of 50 scans per second with traces of 125 to 350 ns in length found that this method was adequate for measuring scour hole depth (holes up to 2.4 ft deep

were recorded), for detecting the presence of refilled scour holes, and in some cases for identifying multiple layers of scoured and refilled material in one hole.

Similarly, in their study of the field performance of GPR and sonar systems on six bridges in Connecticut, Placzek and Haeni (1995) found that their GPR units were effective in measuring the refilled scour holes or subsurface gravel layers in the channel profiles. For the 80, 100 and 300 MHz units tested, the resolution achieved in the field were 2.5, 2.0 and 1.0 ft, respectively, the corresponding penetration depths were reported to be 49.2, 39.4 and 9.8 ft. into the sub bottom. The performance of the system was equivalent to the Continuous Seismic-Reflection Profilers (CSP) also employed in this field-testing program, which are discussed in a subsequent section.

One of the challenges in using a radar system for scour monitoring is that the speed of the EM pulse is altered by changes in the temperature and salinity of the water column as discussed earlier for TDR. In addition to these effects, the attenuation coefficient of the medium, α, is correlated to the conductivity. As the conductivity of the medium increases, so does the attenuation coefficient (see Table 2-1). The attenuation of the signal can be modeled as shown in Equation (2.16), where E_O is the initial signal amplitude, and E_X is the attenuated amplitude of the EM pulse at a depth d. Thus, in salt water the maximum depth is of the order of several centimeters, while Millard et al. (1998) reported achieving measurements at depths of up to 26.2 ft in freshwater river.

$$E_X = E_O e^{-\alpha d} \tag{2.16}$$

Table 2-1: Soil properties pertinent for radar EM techniques, adapted from Millard et al. (1998).

Material	Dielectric Constant	Conductivity [S/ft]	Attenuation Coefficient [ft^{-1}]
Air	~1	0	0.0
Freshwater	77-87	3.05×10^{-4}	0.012
Saltwater	65-75	1.22	~22.56
Saturated Sand	15-25	3.05×10^{-7}	0.16
Saturated Clay	15-60	0.03 – 0.305	1.40
Gravel	22	0.006-0.008	0.64

In addition to the problems of attenuation in saline environments, none of the field measurements conducted to date have consisted of fixed GPR installations. Instead, all of the measurements have consisted of traversed systems, which are reliant on operators to reposition and monitor the equipment. Despite these challenges, the benefits of a GPR scour monitoring system lies in its capability to provide sub bottom information, including the presence of a scour hole even after refill has occurred. Temperature and salinity effects also pose problems, as with the TDR method. However, these effects can be accounted for by measuring the temperature and salinity in the river. Finally, in order to generate a 2D profile or a 3D contour, a means of tracking the unit across the channel is necessary, which adds complications for a long-term deployment of the scour monitoring system.

2.4.2 Bridge Vibration Measurements

The objective of all scour monitoring systems is to measure indicators of the bridge health in order to determine conditions under which a bridge may become

unstable. With traditional measurements, determining the margin to the stability limits is accomplished by comparing the current scour depth to a previously determined maximum allowable scour depth, which is based upon model or experimental data that indicates at what point the foundation becomes unreliable. Another approach, which focuses on determining the 'health' of the bridge pier directly, measures the ambient vibration of the bridge to assess changes in the vibration response resulting from a change in the foundation stability.

Samizo et al. (2007; 2011) developed a method for measuring the response of the bridge piers to microtremors, excitation forces derived from either man-made or natural sources that lead to a general background vibration of the bridge and surrounding sediment. The system consists of two vibration sensors located on the upstream and downstream sides of the bridge pier. The units measured the vibration of the bridge in three axes at 100 Hz for 5 minutes, occurring once every hour (Samizon et al., 2011). The measured vibrations were then transformed from the time domain into the frequency domain using a moving window with 2/3 overlap of 30 seconds each. The average spectral shape during the five minutes was monitored to observe changes in the natural frequencies of the pier, which were assumed to correspond to changes in its stability (Samizo et al., 2007).

In a similar approach, Ko et al. (2011) proposed to monitor both the natural frequency of the bridge as well as changes in the mode shape, which they argued could be attributed to changes in the amount of material surrounding the foundation, that is, scour. Yao et al. (2011) proposed an additional vibration parameter that could be

monitored to indicate changes in the pier foundation. Their approach consisted of computing the ratio of the root mean square (RMS) of each accelerometer axis with its orthogonal axes $\left(\sqrt{\ddot{x}^2}/\sqrt{\ddot{y}^2}, \sqrt{\ddot{x}^2}/\sqrt{\ddot{z}^2}, \text{ and } \sqrt{\ddot{y}^2}/\sqrt{\ddot{z}^2} \text{ for example}\right)$.

Several field and laboratory experiments were conducted to evaluate the utility of the vibration-based method to determine changes in the pier's vibrations due to scour. Integral to the method proposed by Samizo et al. (2007, 2011) is the ability to use microtremors as the source of excitation for the pier, which then allows for the determination of the first natural frequency of the pier from the accelerometer measurements. This hypothesis was tested on bridge A (an unidentified Japanese railway bridge), where the first natural frequency of the bridge was measured with both traditional impact and microtremor based measurements before and after a 13.1 ft excavation, a simulated scour event. The impact testing results indicated that the natural frequency of the bridge shifted from 14.6 Hz in the unscoured condition to 5.9 Hz in the scoured condition. For the microtremor based measurements, the broad spectral response of the bridge in the unscoured condition was characterized by a lack of discernable peaks, while the scoured case exhibited a clearly distinct peak at 6 Hz.

On a separate bridge, Bridge B, impact and microtremor testing on the bridge also revealed that the natural frequencies were consistent with each other, 11.3 and 11.5 Hz, respectively (Samizo et al., 2007). They concluded that microtremors were capable of providing adequate input to the pier to excite the structure as well as indicating that the first natural frequency of the pier declined as the scour depth increased. To verify these results, experiments were conducted on a model pier consisting of steel beams (12.63 ft

long) and a single concrete bridge pier (4.92 x 0.82 x 2.5 ft) supported on a bed of crushed stone less than 0.79 inch in diameter (Samizo et al., 2011). Initially buried 1.64 ft below the sediment surface, the stone surrounding the foundation was progressively removed in order to simulate various scour states. For both impact testing and microtremors, the results of the vibration testing indicated that the first natural frequency of the bridge decreased with increasing amounts of pier foundation exposure. For the fully exposed foundation the natural frequencies declined by as much as 60 to 80%, depending upon the bearing capacity of the sediment, which was also varied (Samizo et al., 2011).

In addition to this fundamental work on the use of pier natural frequencies to detect scour, Ko et al. (2011) conducted field measurements on the Wensui Bridge and Hsichou Bridge in Taiwan. The measured results, the natural frequency and mode shape, were compared with a finite element model of the simply supported, single span bridge units for this site. The foundation was modeled with springs around the piers and the depth of support was varied to correspond to different scour events. During the model evaluation, it was determined that the horizontal-longitudinal (HL) and horizontal-transverse (HT) mode shapes were useful for determining scour. Measurements were then conducted on the two bridges in the field during various reconstruction efforts when the pier foundations were exposed by varying amounts. The measurements were conducted for 10 to 20 minutes on each bridge during non-peak traffic periods. The measurements were taken at a sampling rate of 200 Hz and the average spectra were computed using overlapped windows.

For the Wensui Bridge, two piers were partially exposed with Pier Three (P3) being exposed 19.68-22.96 ft while Pier Two (P2) was only partially exposed. The spectral response, in the HT direction, showed a peak at 1.7 Hz for both piers. The response on P3 had a larger amplitude compared to P2, indicating more scour at this location than on P2. For the Hsichou Bridge, Pier 36 (P36) was exposed 14.76 and 24.6 ft before and during renovations on the bridge, respectively. The HT spectral response indicated a frequency of 2 and 1.5 Hz for the 14.76 and 24.6 ft exposed cases, respectively, a shift of 20%. Yao et al. (2011) also reported on the use of vibration sensors to monitor bridge pier health during laboratory and field experiments in Texas. During the laboratory testing, a simulated pier was instrumented with three axis accelerometers, sampling at 124 Hz. The first natural frequency of the pier in each direction was monitored during a transient scour event along with the ratio of the RMS time histories of each axis. The results indicated a shift in the first vertical natural frequency after the initial formation of the scour hole. In addition, the RMS ratios for the main flow direction versus the lateral direction and for the main flow direction versus the vertical direction showed a shift when the scour hole reached the base of the foundation, at which point an ancillary tilt meter detected settling of the pier.

From the various laboratory and field tests conducted it is possible to conclude that the proposed methods show promise in determining the changes in the health of the bridge pier associated with scour. Various factors can affect the measured vibration characteristics including changes in the flow rate, the ambient temperature, and potentially the background vibration level. Samizo et al. (2007; 2011) addressed the first

of these conditions by conducting long-term experiments on Bridges B and D (unidentified Japanese railway bridges) to determine the relationship between the flow rate and the natural frequency of the pier. On Bridge B, the spectral shape at low and high flow rates consisted of similar natural frequency peaks, with the only difference being the amplitude of various peaks. This result indicated that as the flow rate increases, the amplitudes of the main peaks become increasingly apparent, improving the ability to detect changes during high flow periods typically associated with rapid scour hole formation (Samizo et al., 2007). Bridge D spectra results indicated that the peak frequency from the microtremor measurements occurred between 2.5 and 3 Hz for low and high flow rates, respectively. Additional modes occurring at 3.1 and 2.8 Hz, determined during impact testing on Bridge D, made it impossible to assign a particular frequency to the pier (Samizo et al., 2007). Despite this complication, the overall trend observed at Bridge D indicated a convergence of microtremor results with a corresponding increase in water depth. These results suggest that as the flooding progresses, the pier natural frequency increases in amplitude and become more apparent. Thus, a shift occurring in this frequency during a flood is a likely indicator that scour has occurred.

Additional field measurements were conducted by Yao et al. (2011) on the US 59 Bridge over the Guadalupe River and the SH 80 Bridge over the San Antonio River in Texas. The reported results indicated that the RMS ratio was the only vibration-based measurement that yielded usable results on the US 59 Bridge. The ability to detect the natural frequencies was complicated due to background noise from traffic. For the SH 80

Bridge, the data was reportedly unusable and the vibration-based systems were removed in favor of tilt sensors. In addition to problems with the background noise, variations in the ambient temperature, traffic loading or possible migration of the main channel in the river can lead to changes in the natural frequency of a pier that are unrelated to scour. While it is possible to decouple these shifts from those due to scour, this is a complicated endeavor that requires sophisticated pattern recognition techniques. Therefore, monitoring just the natural frequency and mode shape alone as the sole indication of the formation of a scour hole is complicated at best.

Overall, the results of the various vibration-based measurements indicate the potential for using microtremors to monitor the health of the pier directly. The main challenge is to determine which of the frequencies can be associated with the pier itself. It is necessary to have a distinct peak for the pier that can be monitored over time. The RMS ratio of the various axes also proved useful in the lab, with only limited success in the field. Additionally, monitoring the natural frequency and making a correlation to scour depth is complicated at best since changes in measured frequencies can occur from temperature variations, changes in traffic or loading patterns, wind loading patterns, etc., that make a direct cause and effect relationship difficult to quantify.

2.4.3 Advanced Sonar Techniques

In addition to the standard fixed fathometers discussed previously, there are other sonar based systems that can be deployed to provide detailed information about the riverbed. These vary from fixed frequency fathometers that are tracked during a traverse to provide a profile, side scan sonar units, sector scanning sonar, lens based multi-beam

sonar, and continuous seismic-reflection profilers (CSP). Each of these units will be discussed briefly below, along with a summary of their performance in various field tests.

Fixed fathometer units only provide information about the bed level at one position. To obtain information from more than one position, it is possible to traverse the sonar unit across the channel, either in a boat or from the bridge deck. In either case, an additional tracking unit is required, and is typically accomplished with robotic/automatic total-stations. However, this additional equipment is not well suited for long-term monitoring of scour hole formation.

Side-scan sonar can achieve a 2-D profile and consist of a linear array of sonar units, resulting in a sonar pulse that is narrow in the azimuthal direction (direction of travel of the sonar unit) while it is very wide in the elevation direction (Spindel, 1998). Typically these units also employ a second array of units to act as a receiving array to allow for differential time measurements, and thus depths. The frequencies employed typically range from 80 to 800 KHz (Browne, 2011). The wide angle of the sonar beam allows for a quick survey of a large profile and if used in a fixed orientation does not require a traverse to provide a 2D profile. Typically, the units are traversed using a boat and allow for the determination of a 3D contour of the riverbed. While the additional information is beneficial it is also complicated by the need to account for the position of the unit with time and for roll and pitch of the boat or float housing the unit.

A modification to the side-scan sonar technique is the sector-scanning sonar method, which employs a fan shaped acoustic pulse from a rotating head. The unit emits a pulse, waits for a set period to receive the reflected signals, and then rotates to a new

position and repeats the process. Post-processing of the reflections permits the determination of 2D channel bottom images. These units typically operate in the 330 KHz to 2.25 MHz range with the most commonly deployed units operating at 675 KHz (Browne, 2011). Hayden and Puleo (2011) have proposed a two unit scanning sonar arrangement that can be installed on bridge piers and utilize 250 KH transducers with a beam width of 3°, housed inside an oil filled lens. The units are mounted to motors that can rotate 180° in both azimuth and tilt, leading to a full hemispherical view of the river bottom. The device records 40,000 data points during the measurement sequence which are then interpolated onto a 6.56 x 6.56 ft grid to provide a full 3D contour map of the scour hole development over the entire channel bed.

The final advanced sonar technique that has been deployed in the field to measure scour holes around bridge elements is the CSP unit, which has been adopted from geotechnical surveys. The main difference between these sonar units and standard fixed fathometers is the operating frequency of the acoustic pulse. CSP units typically operate in the 2-20 KHz range as opposed to the 50 to 300 KHz range registered by fathometers (Placzek and Haeni, 1995). This lower frequency means that less of the signal is attenuated and stronger reflections are obtained from subsurface features in the riverbed. In addition, CSP units employ either fixed or variable frequencies, called chirp frequencies. The fixed units typically come in 3.5, 7, and 14 KHz units while chirp CSP units typically use an increasing frequency pulse from 2 to 16 KHz (Placzek and Haeni, 1995). The variable frequency units combine the benefits of a low frequency CSP, i.e., greater depth penetration, with the improved accuracy of a higher frequency CSP. The

downsides of the variable frequency are multiple side lobes and a subsequent increase in noise due to scatter from piers, etc. (Browne, 2011).

While the physical principles behind the operation of the advanced sonar techniques are not significantly different from that of a fixed fathometer, it is still useful to review the field performance of these devices. Eilertsen and Hansen (2008) reported the use of side-scan sonar systems for measuring general river scour in the Øyeren Delta in Norway. The system used a 250 KHz Geoswath interferometric side-scan sonar to record both depth and the amount of reflected signal, which can be correlated to the sediment type. Fourteen scour events were recorded throughout the delta, the largest being a 78.7 ft deep scour hole adjacent to a sandbar that constricted the main channel flow. Hayden and Puleo (2011) reported on the deployment of two lens based sonar systems on the Indian River Inlet in Delaware, which is a scour prone site. Throughout their field campaign, the performance of this system was compared with both the Army Corps of Engineers (USACE) and University of Delaware surveys conducted with a 500 KHz, single unit fathometer linked with a GPS unit and motion tracker. While the USACE data was conducted three years prior to the installation of the two sensors, the interpolated dataset indicated that 82% of the results were within 9.84 ft of the each other. Using the University of Delaware data conducted on the same date as a dataset from the two scanning units resulted in a linear correlation with a slope of 0.98 and an R^2 value of 0.84, indicating a well correlated data set.

Lastly, Placzek and Haeni (1995) conducted several field tests of multiple sonar and GPR technologies at six bridge sites in Connecticut. At the old Baldwin Bridge over

the Connecticut River, a 200 kHz fathometer survey was conducted that revealed several scour holes around the bridge piers. A 10.0 ft hole was recorded upstream of a pier, which was then surveyed with a 3.5 kHz CSP system and measured a 2 ft gravel refill layer. Similar measurements were conducted at the new Baldwin Bridge site and indicated 21 and 15.1 ft scour holes at the bridge piers using the 200 KHz fathometer. The findings were confirmed by a 3.5 KHz fixed frequency CSP survey that also indicated 4.92 ft of refill in a scour hole upstream of one of the bridge piers that was not detected by the fathometer. A swept frequency CSP unit was also used to survey the same bridge as the fixed frequency unit and indicated the same results, with an improved accuracy. The I-84 Buckley Bridge over the Connecticut River was also surveyed as part of this USGS project. The 200 KHz fathometer survey revealed the presence of an 80 ft x 150 ft scour hole upstream of pier four. The survey data was used to generate a 3D contour of the riverbed and scour hole. CSP units and a 100 MHz GPR were also deployed at this site and confirmed the fathometer results, adding details regarding the amount of refill at the bridge section.

Two additional bridges were surveyed with fathometers and CSP units and indicated the presence of scour holes without any refill material or significant sub bottom characteristics. The overall performance results of the Placzek and Haeni (1995) testing revealed that the 20 and 200 KHz fathometers had a resolution of 1.0 ft and 0.5 ft, respectively, while the CSP performance indicated a resolution of 1.0, 2.0, 2.50, and 1.0 ft for the 14, 7, 3.5, and 2 KHz units, respectively. The depth of penetration into the bed

varied from 20, 25, 50, and 50 ft for the same CSP units, respectively (Placzek and Haeni, 1995).

As far as environmental conditions are concerned, only one research team reported on the performance of the advanced sonar techniques under non-ideal conditions. Hayden and Puleo (2011) attributed some of the variability in the measured datasets for the Indian River Inlet to the nature of the active bed and the turbidity of the inlet. In addition to the impact of a live bed on the measured results, the amount of time required for post-processing of the signal was not indicated (the data were collected once a day). Since a long-term monitoring campaign necessitates obtaining multiple measurements within an hour, the frequency of the measurements must be increased before the system can be used for long-term monitoring. In addition to these factors, since the operation of the devices considered is very similar to that of standard fathometers, factors that affect the performance of the latter, such as temperature, salinity, and debris, may also impact the results obtained with the advanced sonar techniques.

Overall, the advanced sonar techniques provide additional information about the riverbed, such as 2D and 3D profiles, as well as sub bottom information and refill. Typically, these systems either require a tracking unit and traverse or complicated data interpolation routines. With the exception of the installation of the two lens-based sonar units on the Indian River Inlet, none of the instruments discussed have been deployed for long-term monitoring.

2.5 Summary

The Failure Modes and Effects Analysis (FMEA), often used in evaluating product designs, can be used by engineers in the design of a scour monitoring system, taking into consideration the potential factors that can influence the field performance. The FMEA consists of evaluating a system or device against a known failure mode. For each failure mode, the effects of the failure are reviewed and given a severity rating (SEV) between one and tem, with one being a failure mode that has little effect, and ten being a failure that prevents the ability to monitor scour entirely. After evaluating the severity of the failure mode, the likelihood of occurrence is evaluated next (OCC) and also given a rating on a 1–10 scale. Next, the ability of the system or operator to detect the failure mode (DET) is assessed. Scores are given to the detectability also on a scale of 1–10. The three ratings, SEV, OCC and DET are then multiplied together to come up with a Risk Priority Number (RPN). The RPN can then be used to evaluate the potential failure modes for the scour monitoring systems and to highlight the areas that should be considered before any field installation begins. The identification of these risk factors is a critical aspect of the FMEA. Ranking scales for each of the FMEA components are identified in Tables 2-2, 2-3, and 2-4, followed by an example analysis on a hypothetical TDR based scour monitoring system in Table 2-5. Through FMEA, it is possible to utilize the information discussed previously for each measurement system to determine their ability to monitor scour under intended field conditions.

Table 2-2: Proposed severity ratings for FMEA analysis of scour monitoring system.

Ranking	Severity Rating (SEV)
1	Impact to scour monitoring system is minor
2-4	Increasing inaccuracies in measured scour results
5	Scour results are available. Magnitude may be incorrect
6-9	As failure mode increases, results become harder to obtain
10	Scour results not available

Table 2-3: Proposed occurrence ratings for FMEA analysis of scour monitoring system.

Ranking	Occurrence Rating (OCC)
1	Event with a 50 year return period (P=0.02)
2-4	Increasing probability of event (P>0.02, P<0.10)
5	Event with a 10 year return period (P=0.10)
6-9	Increasing probability of event (P>0.10, P<0.50)
10	Event with a 2 year return period (P=0.50)

Table 2-4: Proposed detectability ratings for FMEA analysis of scour monitoring system.

Ranking	Detectability Rating (DET)
1	Scour monitoring device can detect failure mode itself
2-4	Increasing inaccuracy of device to detect failure mode
5	Failure mode can be detected via additional instrumentation
6-9	Decreasing ability of additional instrumentation to detect physical failure, i.e., interpreting based on associated parameters
10	Failure mode cannot be detected, except by user onsite

Table 2-5: Example FMEA analysis for TDR system.

Instrument	Failure Mode	Effect of Failure	SEV	OCC	DET	RPN
TDR System	Water Turbidity Changes	Dielectric constant changes a small amount	1	7	8	56
	Water Temperature Changes	Dielectric constant changes significantly	1	9	5	45
	Salinity	Unidentifiable interfaces	10	5	8	400

Table 2-6: Summary of scour monitoring devices.

Device	Max Scour	Refill	Debris		Temp.	Salinity	Other Factors
			D	O			
Sounding Rods	Y	N	M	L	L	L	Bed penetration
Float-Out Devices	Y	Y-N	L-M	L	L	L	NA
MSC	Y	N	H	L	L	L	Fouling of collar clearance
Sonar Fathometer	Y	Y	H	H	M	M	Air entrainment, pulse versus scour hole size, electronic noise
TDR	Y	Y	M	L	M	H	Sediment dielectric constant
Fiber Optics	Y	Y	M	L	L	L	Location specific calibration
Temperature	Y	Y	M	L	NA	L	Live bed
Piezoelectric Film	Y	Y	M	L	L	L	Structural vibrations
Mercury Tip Switch	Y	N	M	L	L	L	Mercury
Radar	Y	Y	L	L	M	H	Attenuation in brackish waters
Pier Vibrations	Y	Y	L	L	M	L	Changes in loading patterns
Advanced Sonar	Y	Y	M	L	M	M	Live Bed

To facilitate the FMEA analysis for a potential bridge scenario, the apparent sensitivities of each of the scour measurement device are reviewed in Table 2-6. Each device is rated against a scale of high (H), medium (M), and low (L) to represent their relative sensitivity to the environmental parameters discussed. The maximum scour and refill measurement capabilities are indicated by yes (Y) and no (N). The level of damage (D) and obstruction (O) caused by the debris is also shown in the table.

Thus, all of the scour monitoring systems can be analyzed with the FMEA process, leading to a more robust field system. A summary for each of the various techniques for monitoring scour is reviewed below.

Rod based devices typically suffer from two main weaknesses. The rods themselves and any attached cabling are subject to damage by debris impacting the hardware, and measurements are made at only one point in the channel bottom.

In its simplest form, the fixed sonar fathometer units provide both maximum scour and refill information for one position in the channel bed. Additional information can be obtained by including tracking units or traversing the unit across the channel bed. However, this increases the system complexity and post processing requirements. In all of their forms, sonar devices are subject to various environmental conditions that can hamper the performance of the unit in the field. These conditions include:

- Temperature variations;
- Salinity in near coastal waters;
- Sediment loads and turbidity;
- Air entrainment;

- Debris, either impacting the device or causing false echoes;
- The relative size of the scour hole and the sonar beam width.

Further study should be conducted into the effects of these environmental parameters on the sonar system results in order to develop means of accounting for these effects.

EM based techniques, both TDR and GPR, can be used to determine the depth of scour holes and refill present in a river profile. The technique is sensitive to environmental parameters, particularly temperature and salinity and data on the field performance of these units is limited. Further study should focus on the performance of these units in the field as well as in the laboratory to identify the impact of the various environmental parameters on the TDR results.

The vibration-based measurement methods discussed provide information about the overall health of the bridge and do not directly measure the scour hole size. The use of this method requires the determination of trends in the vibrational characteristic of the pier, which are complicated in practice due to temperature variations and traffic pattern shifts, as well as channel conditions.

There also exists a series of novel and unique scour monitoring systems that exploit various facets of the channel flow from the temperature gradient within the sub bottom to movement of devices, which can be linked to the presence of the channel flow. These devices have typically been employed in the laboratory and in limited field campaigns. Further work on these devices should focus on translating these ideas into robust methods that can be used in the field.

Available scour monitoring methods are reviewed, including both single point techniques, covered in Section 3, and distributed techniques, discussed in Section 4. The operating principle for each of the devices is discussed along with pertinent performance results from the various field deployments. A review of the environmental factors that affect the operation of the devices are also included, with the goal of highlighting the strengths and weaknesses of each device, and to provide the engineering community with a solid understanding of the tools at their disposal for scour monitoring.

By evaluating the various scour monitoring methods available, it will be possible to determine the operating principles, strengths, and weaknesses of each device, and to highlight the channel conditions that may favor one device over another. Engineers designing future bridge monitoring campaigns can use the information provided herein to select the optimal measurement systems for their particular field conditions and install a more robust system with improved scour monitoring capabilities.

CHAPTER 3

DEVELOPMENT OF A NEW SCOUR MEASUREMENT INSTRUMENT

3.1 Introduction

During the last decade, various projects have been undertaken to evaluate existing scour monitoring techniques, the majority of which have involved the investigation of sonar fathometers and other riverbed mounted sensors. Sonar fathometers, mounted on the bridge piers or abutments, use acoustic signals to record the distance to the riverbed (Nassif et al., 2002). In previous experiments, fathometers have been used in the field to monitor both the maximum scour and subsequent refill during an event (Nassif et al., 2002; Cooper et al., 2000). These field studies, however, were typically hampered by various environmental and operational conditions, specifically channel debris, which interrupted the signal reflected from the river bottom at bridges in Indiana (Cooper et al., 2000) and in New Mexico (Lagasse et al., 1997). Debris can also directly impact the sonar unit or cabling, resulting in a loss of the unit and/or signal altogether (Cooper et al., 2000). Aside from debris, turbulent water can further hinder the operational environment of sonar devices. Holnbeck and McCarthy (2011) reported that of the four sonar units installed at the I-90 Bridge on the Blackfoot River in Montana, only one provided operational data due to highly turbulent water and air entrainment through the bridge section. Temperature and salinity in the channel also significantly

This chapter is adapted from the article published by Fisher et al. (2013c) based on the work done for this project.

affect sonar results. Lagasse et al. (1997) reported that for the John's Pass Bridge in Florida, it was necessary to adjust the measured signal by approximately 1.64 ft on average to account for the temperature and salinity effects. Another commonly used instrument in scour observation is the magnetic sliding collar (MSC), a device consisting of a rod driven into the riverbed with a collar that rests on the bed surface and slides down the rod during a scour event (Lagasse et al., 1997). As the scour hole refills, however, the magnetic collar is buried under the refill material and becomes incapable of recording any refill of the scour hole (Lagasse et al., 1997). As with sonar systems, MSC devices are also vulnerable to debris impacting the device that in turn damages the monitoring unit. It is also possible for sediment in the riverbed to clog the space between the collar and rod and prevent the collar from moving during a scour event (Lagasse et al., 1997).

The time domain reflectometry (TDR) method, which uses EM pulses transmitted through pipes buried in the riverbed, is another rod-based method used for scour observation (Yankeilun and Zabilansky, 1999). TDR is not affected by the debris accumulation around the instrument and can measure refill of the scour hole. However, TDR is susceptible to temperature and salinity changes. Even though Yu and Yu (2009, 2010) reported that varying salinity levels from 0 to 750 ppm did not adversely affect the performance of the TDR method, these ranges are unsuitable for use in near coastal waters. In estuarine environments, for instance, the temperature can vary by 68°F or more and the specific conductance, a measure of the salinity, can vary from a yearly average of

approximately 50 to 17,500 parts per million (USGS, 2006a; USGS, 2006b), well above the range tested in the laboratory.

As shown in the relevant literature, available scour monitoring techniques (e.g., sonar fathometers, TDR, MSC) are susceptible to environmental and flow conditions, including temperature, salinity, turbidity, air entrainment, and debris. Furthermore, MSC devices can only record the maximum scour depth and cannot record refill. In this report, the authors propose a novel technique that is more resilient to environmental and flow conditions and is capable of measuring both scour development and refill.

In the proposed method, several dynamic sensors mounted on thin, flexible plates, referred to as vibration-based turbulent pressure sensors (VTPs), are distributed along the length of a sealed pipe that is driven into the riverbed near the pier or abutment. The VTPs in the river are subjected to the natural turbulence of the river flow and are excited by the associated time varying dynamic pressure. The VTPs in the flow vibrate at amplitude levels detectable by accelerometers. Conversely, a VTP in the sediment, which is not exposed to the flow turbulence, vibrates at much lower amplitudes than those experienced by the VTPs in the flow. The time history of the vibrations of each sensor can be recorded by an accelerometer mounted on the inside surface of the plate. The recorded signals can then be processed to quantify the mean squared acceleration response in the time domain, which is related to the signal energy content. By monitoring the energy content associated with several VTPs distributed throughout the depth of the pier or abutment, it is possible to correlate the changes in vibration response to the

changes in the bed level. Determining the changes in the bed level allows the assessment of not only scour development but also the refill process.

The VTP mechanism is robust against many of the environmental conditions that plague existing scour monitoring devices. Whereas debris in the channel causes false echoes in a sonar system, the VTP method is perceived to be unaffected by floating debris, since debris accumulation does not affect its ability to determine the water/sediment interface. Turbidity, which hinders the performance of sonar fathometers, has a favorable effect on the performance of the VTP due to the additional momentum contributed by the particles impacting the VTP surface. By the same argument, salinity, which has adverse effects on the TDR method, has a minimal influence on turbulent dynamic pressure and hence on the VTP method. Finally, given the anticipated temperature range in natural rivers, which can affect both the TDR and sonar based methods, the response of the VTP method is likely to remain unchanged if thin flexible plates with a low coefficient of thermal expansion are used as vibrating membrane.

Starting in Section 2, the underlying principle behind the VTP device is discussed along with the practical aspects related to the development of a prototype VTP system. The laboratory experimental campaign is discussed in Section 3 and the results are reviewed in Section 4. Pertinent conclusions drawn from the laboratory experiments in preparation for field implementation of the VTP method are discussed in Section 5.

3.2 Numerical Proof of Concept

A simplified numerical proof-of-concept model is built based upon the principles of dynamics for a plate subjected to an applied pressure distribution. It will be established

that a single degree of freedom (SDOF) system provides an adequate means for estimating the dynamic response of the proposed VTP to the varying pressure caused by turbulence in the channel flow. It is useful to define the response of the VTP in the frequency domain since models for the response of a SDOF system are readily available. In addition, the turbulent dynamic pressure in the channel is also described well in the frequency domain. By combining these models, it will be possible to predict the response of the VTP to the pressure associated with the turbulent fluctuation in the channel.

3.2.1 Modeling of Open Channel Turbulent Flow

Several features of the nature of turbulence within open channels lend themselves to being exploited by the VTP method. In particular, the distribution of the turbulent fluctuations in the mean flow direction, $\sqrt{\overline{u'^2}}$, peaks near the riverbed in the wall region, at y^+ of 15 (Nakagawa et al., 1975). The parameter y^+ is equal to the product of the vertical position in the channel, y, and the friction velocity, U_*, divided by the kinematic viscosity of the fluid, υ. Additionally, for open channel flows, once the flow is fully developed, the power spectral density of the turbulent velocity fluctuations, $\Phi_{UU}(f)$, is stationary. The power spectral density is related to the correlation function, $R_x(r)$, as shown in Equation (3.1), for two turbulent velocity measurements, $u'(x)$ and $u'(x+r)$, spaced a distance r apart (Nezu and Nakagawa, 1993). The Taylor's hypothesis of frozen turbulence makes it possible to convert a spectrum, $\Phi_{UU}(k)$ from wave number space, k, to frequency space, f, as shown in Nezu and Nakagawa (1993). In addition, since

$R_x(r)$ can be determined from measurements of the velocities in open channel flows, it is possible to develop experimental representations of the power spectrum, through the use of the Fourier Transform. The resulting power spectrum can be non-dimensionalized for the range of flow conditions typically found in open channels. Thus, various attempts have been made to develop models that match the experimentally measured spectra.

$$\left.\begin{aligned} R_x(r) &= \frac{u_x'(x)\cdot u_x'(x+r)}{\overline{u'^2}} = \int_0^\infty \Phi_{UU}(k)\cos(k\cdot r)\,dk \\ \Phi_{UU}(k) &= \frac{2}{\pi}\int_0^\infty R_x(r)\cos(k\cdot r)\,dr \end{aligned}\right\} \tag{3.1}$$

One such model was developed by von Karman (1948) for isotropic turbulence at high Reynolds number and is valid from the production to the inertial sub-range of the turbulent energy spectrum, Equation (3.2). Another model was developed by Heisenberg (Nakagawa and Nezu, 1975) and is shown in Equation (3.3), which is valid form the inertial sub-range to the point of viscous dissipation. These two models are used to predict the magnitude of the turbulent pressure impinging on the VTP. The reader is directed to Nakagawa et al. (1975), Nezu and Nakagawa (1993), and von Karman (1948) for further details on the development of these models.

$$\overline{u'^2}\Phi_{UU}(f) = \overline{u'^2}\,\frac{4L_X}{U}\left(1+\left(\frac{f}{f_O}\right)^2\right)^{-5/6} \tag{3.2}$$

$$\overline{u'^2}\Phi_{UU}(f) = \left(\frac{2\pi}{U}\right)^{-2/3} C\varepsilon^{2/3}\left(1+\gamma'\left(\frac{2\pi f}{U}\right)^4\right)^{-4/3} \tag{3.3}$$

These models depend upon the mean eddy macroscale, L_X, the characteristic frequency, k_O, the dissipation rate of turbulent energy, ε, the mean flow velocity, U, the root of the mean of the squared turbulence level, $\sqrt{\overline{u'^2}}$, the constants γ' and C, and finally the Kolmogorov length scale, η. The mean eddy macroscale, shown in Equation (3.4), is a function of vertical position in the channel, the channel depth, h, and an empirically determined constant, B_1, which varies from 1 to 1.1.

$$\left.\begin{aligned} \frac{L_X}{h} &= B_1\left(\frac{y}{h}\right)^{1/2} \quad \text{for } y/h < 0.6 \\ \frac{L_X}{h} &= 0.77B_1 \text{ for } y/h > 0.6 \end{aligned}\right\} \tag{3.4}$$

The additional parameters in Equation (3.2) can be determined from the universal function for the turbulence intensity in open channels, which for the mean flow direction are shown in Equation (3.5) (Nezu and Nakagawa, 1993). Equation (3.5), in turn, is dependent upon the friction velocity, the friction Reynolds number, $\mathrm{Re} = hU_*/\upsilon$, y^+ (defined previously), and various empirical constants ($D_U = 2.3$, $B = 10$, and $C_1 = 0.3$).

$$\left.\begin{aligned} \frac{\sqrt{\overline{u'^2}}}{U_*} &= D_U \exp\left(\frac{-y^+}{\mathrm{Re}_*}\right)\Gamma + C_1 y^+\left(1-\Gamma\right) \\ \Gamma &= 1-\exp\left(\frac{-y^+}{B}\right) \end{aligned}\right\} \tag{3.5}$$

The dissipation rate for isotropic turbulence can be modeled as shown in Equation (3.6) (Nakagawa et al., 1975). Finally, the microlength scales (η and ε) can be correlated to the macrolength scales via the relations in Equations (3.7) and (3.8) (Nezu

and Nakagawa, 1993), with $\mathrm{Re}_L = \sqrt{\overline{u'^2}}\, L_X \big/ \upsilon$ and K as given in Equation (3.9) (Nezu and Nakagawa, 1993).

$$\varepsilon = \frac{15\upsilon\sqrt{\overline{u'^2}}}{\lambda^2} \tag{3.6}$$

$$\frac{L_X}{\lambda} = \left(\frac{K}{15}\right)^{1/2} \mathrm{Re}_L^{1/2} \tag{3.7}$$

$$\frac{L_X}{\eta} = K^{1/4}\, \mathrm{Re}_L^{3/4} \tag{3.8}$$

$$K = 0.691 + \frac{3.98}{\sqrt{\mathrm{Re}_L}} \tag{3.9}$$

Given the spectrum for the turbulent velocity fluctuations, the corresponding spectrum for the associated pressure on the flexible plates is constructed as the product of the velocity spectrum and the flow density, ρ, as shown in Equation (3.10).

$$\Phi_{PP}(f) = \frac{1}{2}\rho\overline{u'^2}\Phi_{UU}(f) \tag{3.10}$$

3.2.2 Modeling of VTP Dynamic Response:

Given the nature of the turbulent dynamic pressure in the channel, it is necessary to describe the response of a plate to this dynamic forcing function. Following the method developed by Blevins (1990), it can be shown that the response of a plate, w_i, for each mode i, to the dynamic turbulent pressure, P_i, is governed by Equation (3.11), where ζ_i is the modal damping factor and J_i is the joint acceptance between the mode shape and the pressure distribution.

$$\frac{1}{\omega_i^2}\ddot{w}_i + \frac{2\zeta_i}{\omega_i}\dot{w}_i + w_i = J_i P_i \tag{3.11}$$

The joint acceptance governs the manner in which the modal displacement response of the plate corresponds to the spatially varied pressure distribution for a given mode. Under the condition that the mode shape and the pressure distribution are aligned, the joint acceptance is one (Blevins, 1990), and the solution to Equation (3.10) for a sinusoidal pressure distribution becomes the classical harmonic excitation response of a SDOF system. Given that the turbulence in open channels is stationary and random, the autospectral density of the displacement response of the VTP, $\Phi_{XX}(\omega)$, can then be computed from the mean square of the classical harmonic excitation response to the autospectral density of the pressure distribution, as shown in Equation (3.12). What remains, is then to describe the means square response of the VTP, and couple that response function with the previously discussed turbulent pressure spectrum given by Equation (3.10).

$$\Phi_{XX}(\omega) = \left|H(\omega)\right|^2 \Phi_{PP}(\omega) \tag{3.12}$$

The steady state response function $\left|H(\omega)\right|^2$ can be described from the modal damping, and the natural frequency, ω_N, of the SDOF system, as shown in Equation (3.13) (Blevins, 1990; Craig, 1981).

$$\left|H(\omega)\right|^2 = \frac{1}{\left(1+\left(\frac{\omega}{\omega_N}\right)^2\right)^2 + \left(2\zeta\frac{\omega}{\omega_N}\right)^2} \tag{3.13}$$

A closed form solution for the first natural frequency of a circular plate fixed at its circumference is given below in Equation (3.14) (Blevins, 1979), where r is the radius of the disk, E is the Young's modulus, ν is the Poisson's ratio, ρ is the density, and t is the plate thickness.

$$\omega_N = \frac{10.22}{r^2}\frac{Et^3}{\sqrt{12\rho t\left(1-\nu^2\right)}} \tag{3.14}$$

3.2.3 Numerical Model Results

The SDOF model and the input forcing function, discussed previously, are used to model the response of the VTP to the dynamic excitation from turbulent flow. The flow situation considered has a mean flow speed of 0.98 ft/s and a depth of 9.84 ft with a VTP located at y/h of 0.1 (a representative case for natural channels).

The displacement response spectrum from the VTP model is shown in Figure 3.1, along with the velocity and acceleration spectra, computed from derivatives of Equation (3.11). The turbulent spectrum of the forcing function (due to turbulent pressure) is also shown in Figure 3.1, including both the production and inertial sub-ranges. The spectrum exhibits a broad peak at low frequencies, less than 0.1 Hz, associated with the large eddy structures in the flow. The inertial sub-range encompasses approximately 0.1 to 40 Hz, at which point the declination in the amplitude of the input spectrum is observed. This reduction is associated with the transition to the viscous sub-range. Accordingly, an ideal VTP would be sensitive to the turbulent pressure within the 0.1 - 40 Hz frequency range.

The first natural frequency for a representative circular plate made from neoprene rubber, calculated using Equation (3.14), can be seen in all three response spectra at

approximately 250 Hz. The relative magnitudes between the acceleration, velocity, and displacement spectra reveal the frequency range various sensors would be useful in recording the response of the VTP. In the low, near DC, frequency range, less than 10 Hz, the results indicate that a position sensor would be optimal. However, in the range of 10 to 400 Hz, the figure indicates that an accelerometer would be better suited to measure the response. Accelerometers with sensitivities over the 10 to 400 Hz frequency range are commonly available. Therefore, for the initial prototype these accelerometers are selected for the development of the scaled prototype model.

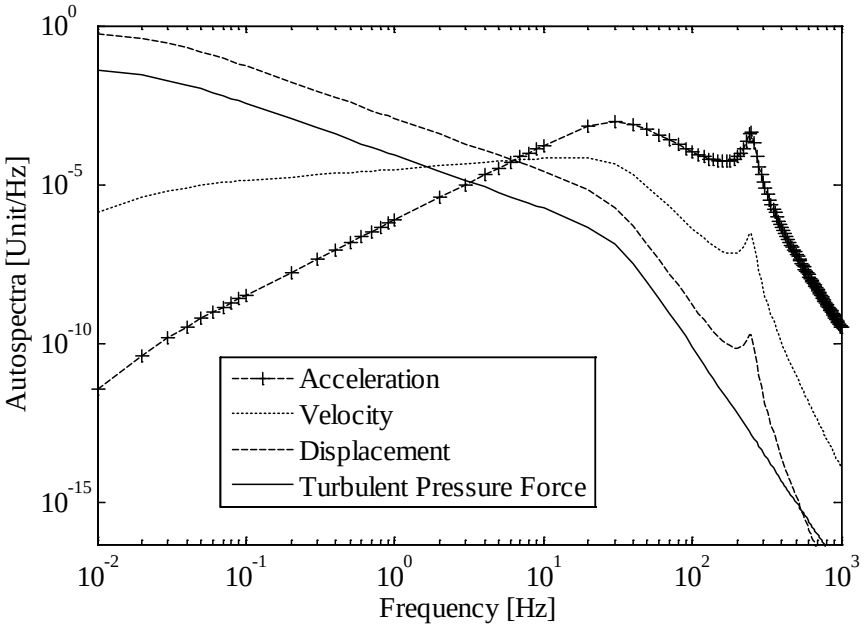

Figure 3.1: Model response for the prototype VTP based upon SDOF model and turbulent spectrum. The units for displacement, velocity, and acceleration autospectra are ft Hz^{-1}, ft $s^{-1}Hz^{-1}$, ft $s^{-2}Hz^{-1}$, respectively.

During operation of the VTP, the variation in the energy content of the flexible plates throughout the depth of the pier or abutment must be monitored with low energy content corresponding to sediment and high energy content corresponding to channel flow. Using the spectra shown in Figure 3.1, it is also possible to compute the mean value of the acceleration auto spectrum of the vibration response over the frequency range of interest (Blevins, 1990). The response spectra computed for various geometric and material configurations can then be used to evaluate the hypothesis behind the operation of the VTP device and to determine the optimal configuration for the prototype.

Based upon the numerical model results, an optimal VTP would respond to low frequency turbulent pressure fluctuations at a level detectable by commercially available accelerometers. The VTP prototype must be designed considering the competing constraints of maximizing the energy content response while keeping the dimensions of the plate small. A smaller size of a VTP sensor will reduce the spacing between the sensors, providing higher scour measurement resolution.

For the VTP prototype, both metallic and nonmetallic materials are considered, including stainless steel (304 Grade), aluminum, (6061-T6), brass, and three plastics, PVC, LDPE, and a neoprene rubber (durometer of 30A). Plates 0.126 inch in thickness with both circular and square geometric forms are considered. The simplified numerical model is used to analyze the response, with an appropriate change in Equation (3.14) for the square geometry (Blevins, 1979). The energy content response computed for various VTP plate areas are plotted in Figure 3.2.

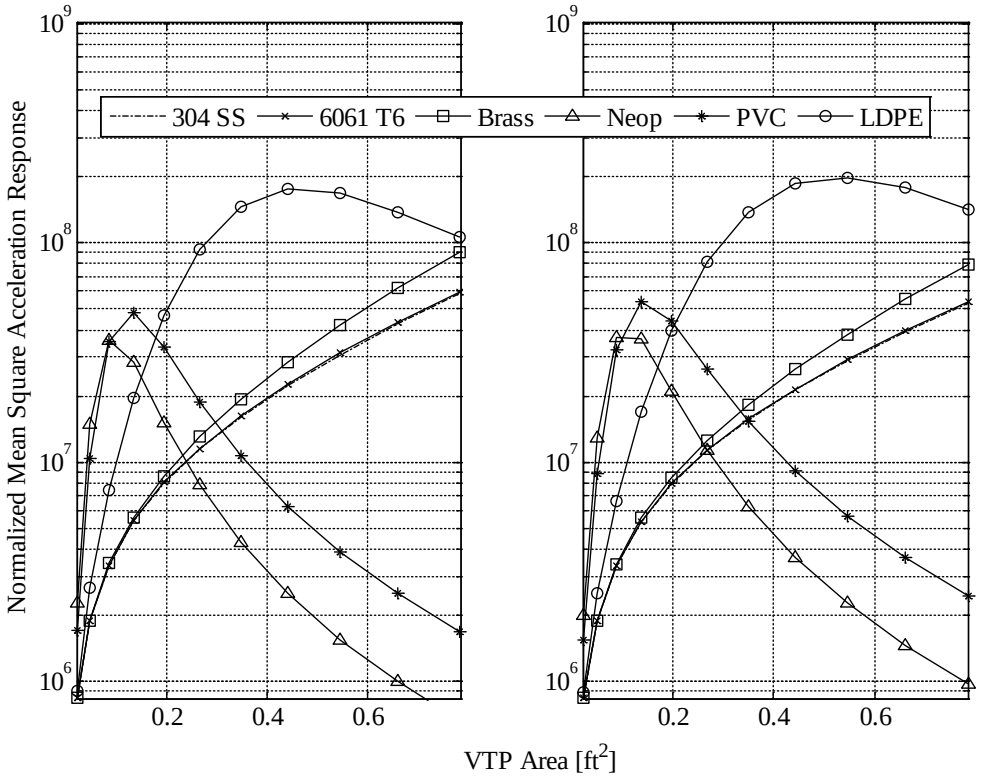

Figure 3.2: Circular and square VTP normalized mean square response as computed from the response spectrum from 10 to 400 Hz for circular and square VTPs, for various plate areas, and material types. Each result is normalized by the deflected mode shape as given by Equation (3.13).

For the metallic materials, the circular VTP consistently has the higher energy content over the square VTP for a given area and material. For the largest VTP, with an area of 0.79 ft^2, the circular aluminum, brass, and stainless steel VTPs have a mean response level 9, 13, and 10% greater than the square VTP. For each geometric shape, the brass VTP responds, on average, at a level 14% above that of the aluminum VTP and 18% above that of the stainless steel VTP. Therefore, for the metallic VTPs, the circular VTP is the preferred configuration, with the optimum metallic material being brass.

For the nonmetallic materials, the optimal geometric configuration depends upon the VTP area. For instance, for the LDPE, the circular VTP at lower areas responds as much as 14% more than the square VTP, for the same area. However, as the area of the VTP increases, this trend shifts. For the LDPE VTP, this transition occurs at areas above 0.32 ft^2, while for the PVC and neoprene VTPs this occurs at 0.086 and 0.053 ft^2, respectively. Within a particular case (lower and higher areas of the plate), the optimal material also is a function of area. At lower VTP sizes (0.022 to 0.086 ft^2), the neoprene VTP responds on average 19% more than the PVC VTP. For the 0.11 ft^2 case, however, the PVC response peaks 68% higher than the neoprene. From 0.22 to 0.75 ft^2, the LDPE response peaks and is several orders of magnitude larger than that of the PVC or neoprene VTPs. Thus, for the nonmetallic VTPs, the optimal geometry and material choice are a function of area. For smaller VTPs, a circular, neoprene VTP is optimal. For larger VTPs, an LDPE, square VTP is optimal.

When considering an optimal VTP configuration for evaluating the hypothesis behind the operation of the VTP devices, it is important to balance the desire to maximize the response level in the turbulent flow with the size of the plate. Therefore, a size limit of 0.11 ft^2 is imposed to keep the spacing in line with the resolution of an MSC device. Based on this limit, it can be concluded that a circular VTP made from neoprene is optimal.

3.3 Experimental Setup

According to the materials and geometric form selected in the previous section, a prototype is constructed with eight neoprene VTPs of 1 inch radius. The VTPs are spaced

approximately 4 inches apart, on center, in a 4-inch diameter PVC support pipe. A schematic of the prototype assembly is shown in Figure 3.3. The assembly consists of a compression pipe coupling mounted in the support pipe with a toroid disk sandwiched between the compression coupling components. The flexible plate is fixed to the toroid disk, as shown in Figure 3.3. Overall, the size of the VTP and the support pipe are small in comparison with the physical dimensions of a pier, which are typically 1.64 to 3.28 ft or more in width. For a typical pier, the equilibrium scour depth predicted with the equation proposed by Neill (1964) is approximately 4.6 ft, while the pipe would only result in a scour hole of 1.0 ft, well within the original scour depth. As such, the presence of the VTP is anticipated to have a limited effect on the flow around the pier and scour around a pier or abutment.

The support pipe is buried below the sediment, with several sensors exposed to the flow and several sensors below the water/sediment interface. The experiments are conducted in the Clemson Hydraulic Laboratory in a 4 x 4 ft square cross section, 60 ft long flume. The flume is equipped with a recess for scour measurements, in which the support pipe and VTPs are located. The support pipe is fixed to the flume frame, as shown in Figure 3.4. The riverbed is simulated with quartz sand of median size (d_{50}) of 0.06 inch. A sand bed represents a worst case evaluation of the VTP method since the pressure waves impinging on the bed from the turbulent flow will have a greater depth of penetration in the quartz sand bed. Energy dissipation of a wave will be greatest in clay or silt bed (Gutowski and Dym, 1976), the turbulent pressures incident on the sand bed will propagate furthest into the sand bed, leading to the highest possible response from a

VTP in the sediment. The flow rates are varied from 1 to 4.94 cubic feet per second, which is measured with an FMG3101 magnetic flow meter.

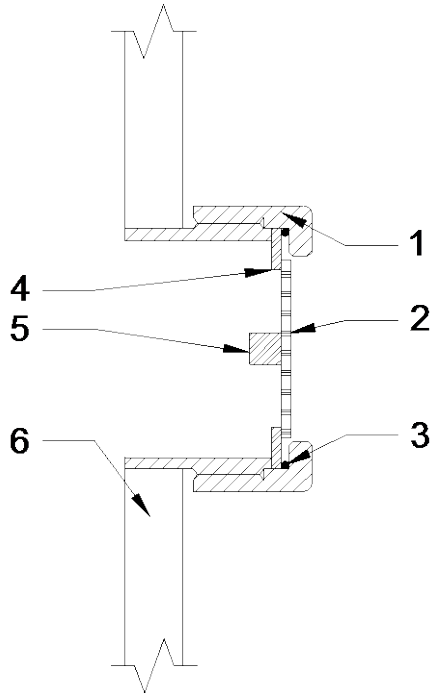

Figure 3.3: Prototype VTP configuration. Components include: (1) the compression fitting, (2) the vibrating membrane, (3) a washer, (4) toroid disk, (5) accelerometer, and (6) the support pipe.

To measure the acceleration of the VTP plate, a B&K 4507 B 006 uniaxial transducer, with a sensitivity of approximately 15.55 mV/ft/s^2, is mounted in the center of the flexible plate inside each VTP sensor. These accelerometers are connected to a B&K LAN-XI 3050A-060 data acquisition system. A sampling frequency of 25.6 kHz yields a converged RMS (root mean square) value of the acceleration response for a given flow condition, and is thus selected as the measurement frequency for the experiments. The

measurements are recorded for 10 seconds each with 10 repeat measurements for each flow condition. The mean squared value is computed for each VTP from the measured signals, which is proportional to the energy of the time domain acceleration. The mean squared value will be referred to as the VTP energy content for the remainder of this report. The experimental setup is shown in Figure 3.4.

Figure 3.4: Prototype VTP array installed in the flume. VTPs 1-4 are shown above the sand bed. The instrument is anchored to the flume wall.

3.4 Results and Discussion

The experiments are conducted with three objectives; (i) to supply a proof-of-concept, (ii) to evaluate the performance of the VTP system in a scour hole and (iii) to determine the precision of the VTPs.

3.4.1 Verification of the Hypothesis behind VTP

During this phase of testing, eight VTPs are used with two in the sediment (VTPs #7 and #8) and two positioned in the flow (VTPs #5 and #6). VTPs #1-#4 in this test are above the water free surface. VTP #8 is situated at the lowest position (0.52 ft below the sediment bed) while VTP #5 is situated at the highest position (0.46 ft above the sediment bed). The results of the tests are shown in Figures 3.5 and 3.6.

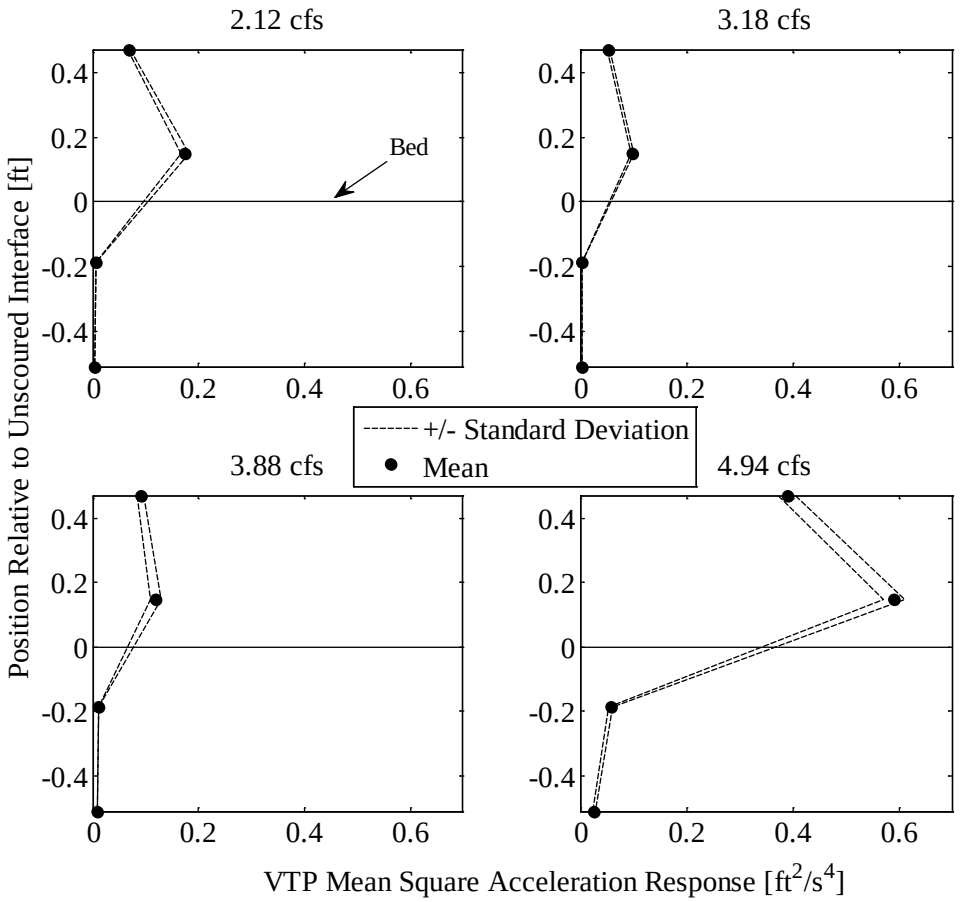

Figure 3.5: Energy content of prototype VTPs as a function of distance from the water/sediment interface. Flow rates varied from 2.12 to 4.94 cfs. Mean values plotted along with ± 1 standard deviation and the unscoured bed level.

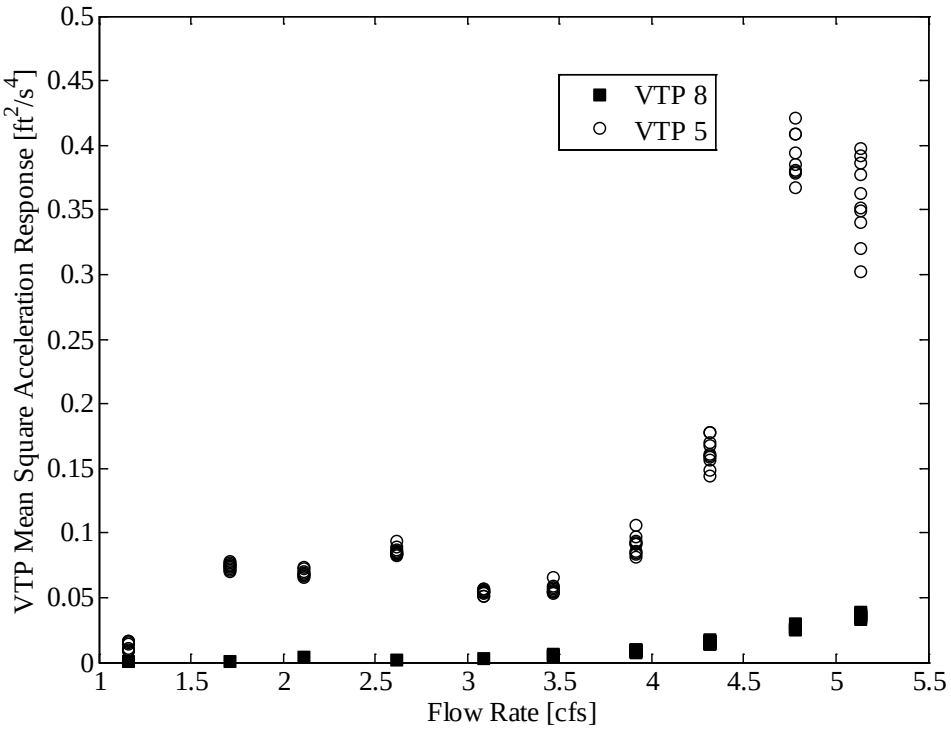

Figure 3.6: VTP energy content of prototype device versus flume flow rates*.

In Figure 3.5, the energy content response is calculated for four different flow rates ranging from 2.12 to 4.94 cfs and plotted against the distance from the sediment interface. The mean and standard deviation of the ten 10-second measurements are plotted to present the central tendency and the variability of the measurements. In Figure 3.5, the VTP within the flow and adjacent to the bed measures the peak energy content. The energy content decreases with increasing distance from the sediment surface, which is in agreement with the expected profile of the flow turbulence across the depth of the

* Note that the energy content of the VTP buried in the sediment also increases in Figure 3.6. Additional experiments reveal that the flume used in the VTP evaluation is excited by the flow and pump used in the laboratory. Thus, the increase in the energy content of the VTP in the sediment is attributed to the vibration of the flume itself. Corrections to the signals to account for this additional structurally borne noise reveal the same trend as shown above. Such structurally borne noise will, of course, not contribute to the field performance of this technique.

channel. On the other hand, the VTP response in the sediment is one to two orders of magnitude lower than the measured energy content in the flow. This difference between the energy content levels of VTPs in the channel and in the sediment is well above the uncertainty bounds of the sensors in the flow. Thus, suggesting that the low-frequency vibration response of the VTP can be used to distinguish between channel flow and sediment.

In Figure 3.6, the mean square of the time domain response of VTP #5, located in the channel flow, is compared against that of VTP #8, located in the sediment, for varying flow rates. For each flow rate, the average for each of the ten 10-second measurements is plotted. For all flow rates, the average difference between the VTPs in the flow and the sediment is 0.3 ft^2/s^4. Depending upon the flow rate, the minimum difference between the two signals is one order of magnitude, while the largest difference increases to two orders of magnitude. Figure 3.6 shows a general trend where the measured energy content increases with flow rate, an observation consistent with expectations since the amplitude of the pressure fluctuations due to turbulence increases with the mean flow speed, and therefore with flow rate. Even at low flow rates, the difference between the mean square response in the flow and sediment is detectable. Thus, as the flow rate, and therefore the flow velocity increases, the difference in energy content levels for VTPs located in the flow versus the sediment increases, aiding in the observation of the water/sediment interface, as shown in Figure 3.6. It should be noted, however, that for the highest flow rate, the energy content level drops slightly from the value at a flow rate of 4.76 cfs. This is attributed to the 10 second averaging time, which

may not fully capture all of the large eddies in the flow. Future field tests should investigate longer averaging times to avoid this complication.

Additionally, Figure 3.6 highlights the potential impact that additional vibration sources can have on this method. The energy content of the VTPs in the sediment, which are dominated by noise vibration sources*, are an order of magnitude below the responses from the VTPs located in the flow, which are also subject to the same noise sources but are dominated by the vibrations due to the turbulent flow.

3.4.2 Assessing Performance of VTP in Scour Hole

The nature of the turbulence in a scour hole varies in magnitude and spatial distribution from that in the channel flow, making it necessary to verify the performance of the VTPs in a scour hole. For this purpose, the response of the VTP located in a manually-developed 2.2 inches deep scour hole is measured (Figure 3.7). The experiments are conducted where VTP #1 is partially submerged in the channel flow, VTPs #2-#4 fully submerged, VTP #5 partially visible in the unscoured bed and VTPs #6-#8 fully in the sediment. The energy content, computed as the mean square of the time domain acceleration response, is computed for each VTP and the mean and standard deviation are plotted against position relative to the bed in Figure 3.7.

Figure 3.7 indicates that VTP #5, which is fully uncovered by the scour hole development, is subject to an excitation level that is greater than the excitation in the main flow. This is expected, since the turbulence intensity should be higher in the scour hole due to flow separation (Dey and Barbhuiya, 2006). Thus, the presence of the scour hole itself improves the ability of a VTP to detect the water/sediment interface.

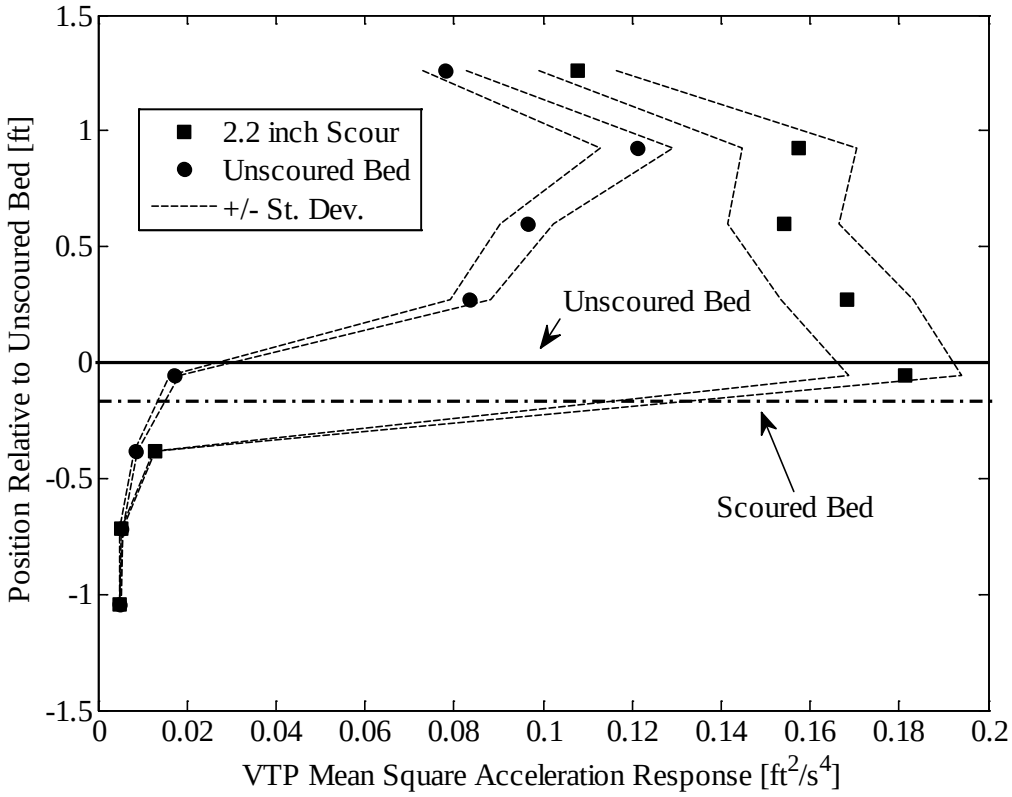

Figure 3.7: Turbulent energy content of prototype VTPs in unscoured and 0.18 ft deep scour hole. The mean values are denoted by the points while the dotted lines represent the ± 1 standard deviation of the measured results around the mean value.

3.4.3 Precision Assessment

The precision of the VTP scour detection is investigated with several experimentally controlled scour holes ranging in depth from approximately 1.56 to 5.5 inches. During these experiments, VTP #1 is partially submerged, VTPs #2-#4 are fully submerged, VTPs #5-#8 are buried in the sediment, and VTPs #5 and #6 are visible due to the various scour holes. The slope of the VTP energy content is computed along the depth, with the maximum gradient used as the determining point for the sediment interface. The depth of the scour hole is determined as the average height between the

two VTPs surrounding the point of maximum gradient. Figure 3.8 shows six profiles for the cases varying from no scour to the 5.5 inches deep scour hole, along with the slope of the profiles. Figure 3.8 reveals that, for the 2.2 to 5.5 inches deep scour holes, the point of maximum slope corresponds to the interface location.

Also shown in Figure 3.8 are the results for the 0 and 1.56 inches deep scour holes, where the point of maximum slope is above the channel bed. Since it is only possible to locate the interface as the mid-height of the two VTP positions around the point of maximum slope, the VTP indicated water/sediment interface is 1.2 inches above the original bed level. Additionally, in the 1.56 inches deep scour hole case, VTP #5 responds at a level between its adjacent VTPs. In this case, VTP #5 is not fully exposed by the scour hole, indicating that a critical depth of scour around the VTP is required to observe enough of the turbulent flow to obtain an accurate measure of the water/sediment interface. As the scour hole deepens and uncovers more surface area of the VTP, the response increases, yielding a more accurate water/sediment interface location.

During the development of the scour hole shown in Figure 3.8, the 5.5-inch scour event occurred prior to the 4.7-inch event, thus the 4.7-inch event results represent a refilling scour hole scenario. For the 4.7-inch event, VTP #6 is partially exposed for approximately 50% of its diameter. Correspondingly, the energy content of VTP #6 (0.017 ft^2/s^4) is between the values for the adjacent VTPs, 0.12 ft^2/s^4 for VTP #5 in the flow and 0.0054 ft^2/s^4 for VTP #7 in the sediment. As the refill process proceeds, however, the response of VTP #6 continues to drop, resulting in a determination of the interface location during refill.

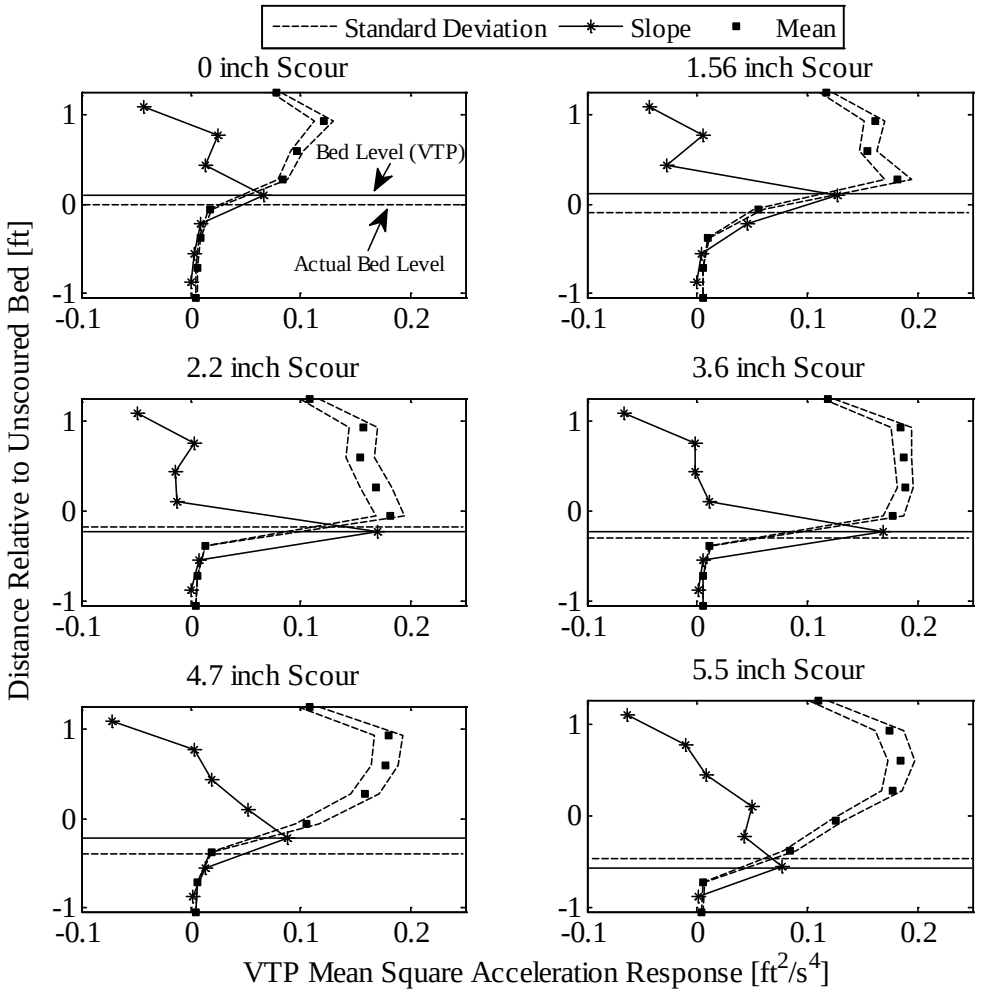

Figure 3.8: Energy content of prototype VTPs in scour holes of various sizes. The mean profile with ± 1 standard deviation is plotted alongside the slope of the mean profile, scaled by a factor of 1/10. The VTP and the independently measured scour hole depths are indicated for each experiment.

The scour depth detected by the VTP is then compared against the independently measured scour depth to assess the precision with which the VTP can determine the water/sediment interface (Figure 3.9). Ideally, this comparison would yield a straight line with a slope of 1:1. The results shown in Figure 3.9, however, highlight the importance of

spacing between the VTP sensors. Error bars plotted for each of the VTP interface locations represent +/- ½ of the spacing. Since the point of scour is determined by the average of the two VTPs above/below the point of maximum slope, having a larger number of closely spaced VTPs would decrease the spacing between detection points. This would lead to an improved precision in determining the scour hole location.

Figure 3.9 also illustrates that for the 4.7-inch scour hole, where VTP #6 is uncovered for approximately 50% of its depth, the VTP determined scour depth, even considering the uncertainty bars, predicts a value below that of the independently measured depth. This result, in conjunction with the result from the 1.4-inch scour case, where VTP #5 was uncovered for approximately 88% of its surface yet still indicated a scour position between VTPs #4 and #5 instead of #5 and #6, indicates that there is a minimum amount of VTP surface that must be uncovered by scour to register the presence of the turbulent flow. This result is attributed to the nature of the dynamic force due to turbulent flow impinging on the VTP surface. Since the magnitude of this force is a function of the exposed area, for a partially exposed VTP the energy content is lower than for a fully exposed VTP. As the scour location is determined by the point of maximum slope, an energy content level between a partially exposed VTP and one in the sediment does not result in a significant change in the slope, leading to an inaccurate reading. Conservatively, this minimum exposure can be taken as the entire surface of the VTP area. Further testing, however, is necessary for the final field version of the VTP device to verify this result.

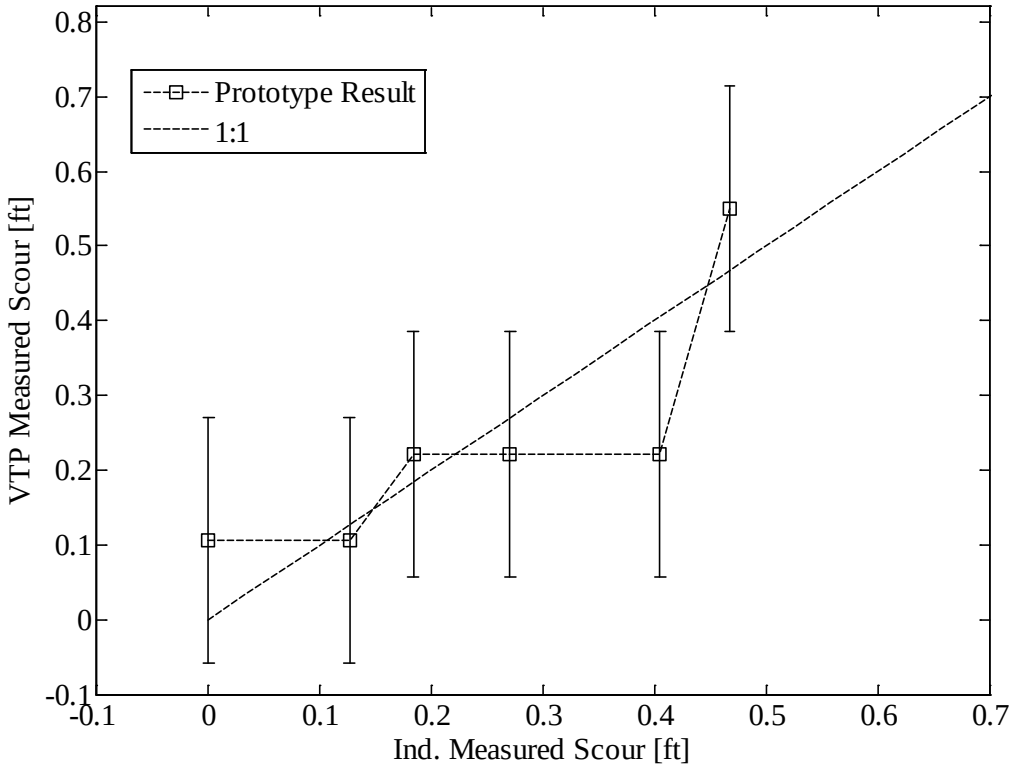

Figure 3.9: VTP estimated scour depth versus actual scour values. The scour values determined from the VTP setup are based on the point of maximum slope. An ideal sensor would fall on the 1:1 line.

The results presented show that the VTP is capable of distinguishing whether the surrounding material is sediment or flowing water in a channel. The results also show that the method is feasible in the presence of a scour hole. The higher level of turbulence in a scour hole results in a dynamic pressure that is higher in magnitude than in the main, unscoured channel. Also, the precision of the method is shown to be within the VTP sensor spacing, which can be improved by reducing the spacing of the VTP units through further refinement of the device.

3.5 Summary

Since measuring scour is of critical importance, and given that traditional devices are susceptible to many of the conditions in natural channels, a novel method is proposed that can determine scour depth in real time and is also insensitive to many of the conditions that cause other monitoring methods to fail. The proposed methodology consists of a series of vibration-based turbulent pressure sensors, referred to as VTPs, mounted along the length of a support pipe that is buried in the channel bed. The VTPs consist of an accelerometer attached to a thin plate, which is exposed to the channel. The mean squared acceleration response of the plate is computed in the time domain and used to determine if the material surrounding the VTP is water or sediment. Since the device is sensitive to the dynamic pressure in the flow associated with turbulent fluctuations, a VTP with high energy content indicates the presence of flowing water in the channel. A VTP in the sediment however, is not subject to the same dynamic pressure as the one in the flow. Therefore, by measuring the profile of the energy content for multiple VTPs mounted along a bridge pier or abutment, it is possible to determine the location of the water/sediment interface.

Based upon the experimental results presented, the evidence demonstrates that the energy content of the VTPs located in the sediment is one to two orders of magnitude lower than that of the VTPs located in the channel flow. Therefore, the original hypothesis that it is possible to exploit the difference between the mean excitation level in the sediment and those in the flow to measure the water/sediment interface is demonstrated to be an effective means of monitoring the riverbed for scour. Additionally,

the measurement results show that the slope of the energy content profile relative to depth is a reliable way of determining the location of the water/sediment interface, located by the point of maximum slope.

The presence of a scour hole is also shown to have little impact on the ability of the VTP method to determine the location of the water/sediment interface. The experimental results, however, reveal that the percentage of the VTP surface that is exposed to the flow affects the VTP response and thus the determination of the water/sediment interface. Even considering this fact, the precision of the VTPs is shown to be better than 4 inches, which is more accurate than the MSC device (which has a precision of 6 inches) but is below that of a sonar/fathometer (which is accurate to within 1.1 inches).

The precision of the device is dependent upon the resolution of the sensors, and thus the VTP size. With further refinement of the sensors, the precision of the system can be improved. Additionally, further testing is needed to identify the critical amount of VTP surface exposure to the turbulent flow required to improve the identification of the presence of turbulent flow surrounding the VTP.

CHAPTER 4

OPTIMIZATION OF THE VIBRATION-BASED TURBULENT PRESSURE DEVICE FOR FIELD DEPLOYMENT

4.1 Introduction

To fully account for the fluid-structure interaction, a 3D flow model and an associated structural analysis model are necessary. To capture the full turbulent flow spectrum, the 3D fluid model must be capable of calculating the instantaneous velocity field. This is required to determine the dynamic response of a structure to both large and small scale turbulent eddies (low and high frequency incident forces). Only Large Eddy Simulation (LES) or Direct Numerical Simulation (DNS) methods are available to fully capture the instantaneous velocity field (Breuer and Münsch, 2008). These models, however, require significant computational time and resources, even without considering the structural analysis component. Hence, these models are generally not applied to design optimization problems.

To solve the fluid-structure interaction involving the dynamic response of a structure and the turbulent flow field, this study aims to develop a semi-empirical model incorporating closed form solutions for the structural response and empirical relationships for the turbulent open channel flow. The applicability of this semi-empirical model is demonstrated by predicting the response of a flexible disk subject to turbulent open channel flows. The flexible disk studied herein is a part of the scour monitoring sensing

This chapter is adapted from the article published by Fisher et al. (2013d) based on the work done for this project.

system as discussed in Chapter 3. The device called a vibration-based turbulent pressure sensor (VTP), measures the vibrational energy content of a flexible disk. The response of a VTP within the flow and in the sediment bed is used to locate the water sediment interface and thus monitor scour.

The objective of this report is to consider the development of a simplified, semi-empirical model that predicts the response of a flexible plate to turbulent open channel flow and to validate the model predictions with appropriate experimental measurements. This is accomplished by considering empirical descriptions for the turbulent flow and analytical solutions to a single degree of freedom oscillator, which are discussed in Section 2. In Section 3, the model developed is verified, calibrated, and validated using experimental data sets obtained from modal tests and vibration measurements conducted in an open channel flume. Section 4 presents a case study application of the simplified model to optimize the VTP device through a parametric analysis. Results from tests on the field prototype are discussed in Section 5, while pertinent conclusions from this work are discussed in Section 6.

4.2 Modeling Approach

The nature of the flows studied in fluid dynamics can be divided into two groups, laminar and turbulent. All natural channels flow under turbulent conditions. The instantaneous turbulent velocity at any given point may be divided into two components; a time-averaged velocity component also called the mean velocity and a fluctuating part. Turbulent flow is characterized by the presence of flow instabilities that are responsible for velocity fluctuations. The root mean squares (RMS) of these fluctuations vary in

magnitude from 5% of the mean flow for turbulent open channels to as much as 10 to 30% in aerodynamic boundary layers (Panton 2005).

Fluctuations are present in all of the velocity components and pressure in any turbulent flow, which can be described through Reynolds' decomposition into the mean component, U, V, and W in the three cardinal directions, as shown in Figure 4.1 (x is along the flow direction, y is normal to the bed, and z is across the channel width), and the fluctuation components, u', v', and w'. Thus, when describing the instantaneous flow velocities, $\tilde{U}$, $\tilde{V}$, and $\tilde{W}$ at any point, it is necessary to include both components as given by Equation (4.1), see Figure 4.2.

$$\begin{aligned} \tilde{U} &= U + u' \\ \tilde{V} &= V + v' \\ \tilde{W} &= U + w' \end{aligned} \tag{4.1}$$

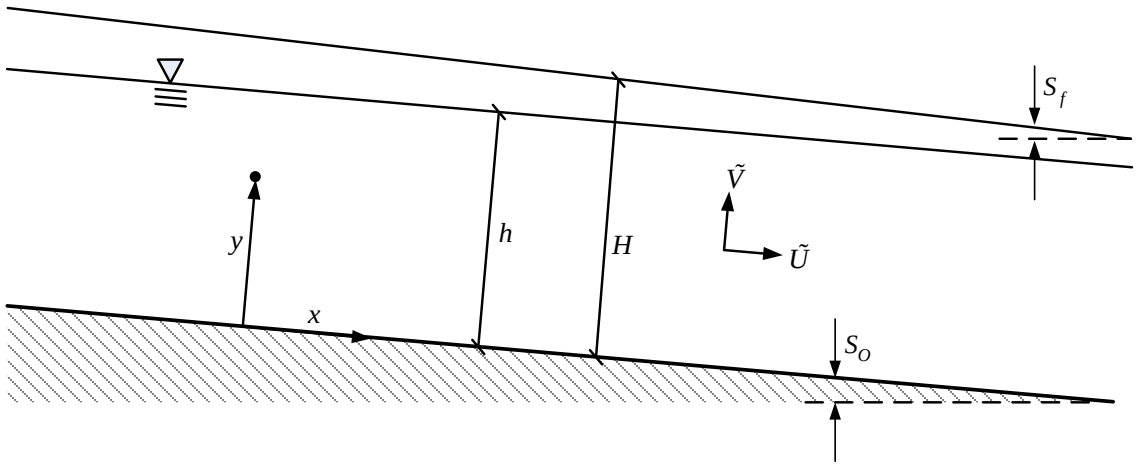

Figure 4.1: Channel parameters relevant to the Navier-Stokes equations.

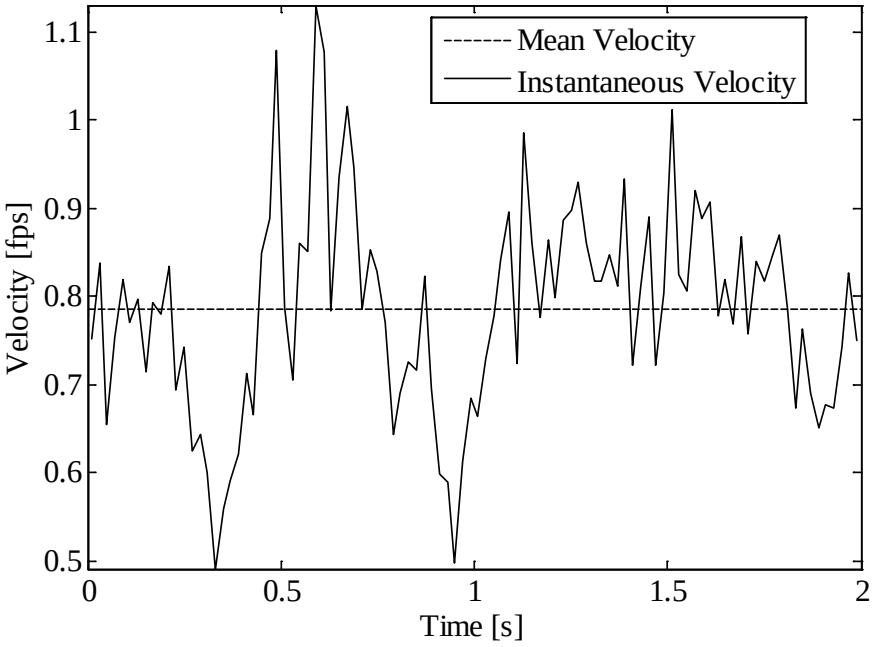

Figure 4.2: Sample turbulent velocity time history.

A similar expression can be developed for the instantaneous pressure in the flow, $\tilde{P}$, which can be decomposed into its mean pressure, P, and the fluctuating component, p'. Based upon these definitions, it is necessary then that the average values of $\tilde{U}$, $\tilde{V}$, and $\tilde{W}$ yield U, V, and W meaning that the long-term averages of u', v', and w' are zero.

Turbulent flows are also characterized by eddy motions. Eddies are instabilities in the flow that are spatially and temporally correlated and are responsible for the velocity and pressure fluctuations. These eddies vary in size, with smaller eddies contained within larger eddies, up to the largest eddy in the flow. These eddies vary in scale from the molecular level where the smallest eddies are dissipated due to viscous forces as heat, to the large eddies which depend upon the size of the channel (Panton 2005). The

distribution of eddy sizes in the flow leads to the energy cascade from the larger eddies, responsible for the production of turbulence, to the smaller eddies. The turbulent flow features discussed above will be utilized in developing a model to predict the response of a VTP under turbulent flow conditions.

4.2.1 Model for Prediction of RMS Values of Fluctuating Turbulent Velocity

Wall bounded turbulent flows can be divided into two regions, the inner region (IR) close to the wall, and the outer region (OR) near the free surface (Nezu and Nakagawa, 1993). For all wall bounded flows, the inner region is further decomposed into the viscous sub-layer (VSL), where viscous forces dominate, the buffer layer, and the log-law layer (LLL). Adjacent to the LLL is the outer region, which for open channel flows is affected by the presence of the free surface. The OR is broken down into the free surface region (FSR) and the equilibrium region (ER), which lies between the inner layer and the FSR. For smooth beds, the thickness of the VSL is defined as $\delta_V = 5\upsilon/U_*$, where υ is the kinematic velocity of the fluid and U_* is the friction velocity, which is typically small, of the order of 0.02 inch (Nezu, 2005). Throughout the inner region $\left(y/h < 0.2\right)$, turbulence is generated by low speed streaks, which are ejected from the near wall region and subsequently burst (Davidson, 2004, Nakagawa et al., 1975). For rough boundary layers, as k_S (equivalent sand roughness) increases the large eddies are interrupted by the roughness elements, leading to an increasingly isotropic turbulence (Nezu and Nakagawa, 1993). Immediately outside the IR lies the ER, $\left(0.2 < y/h < 0.6\right)$, where neither the free surface or wall effects dominate (Nezu and Nakagawa, 1993). In this region, the rates of

turbulent production and dissipation are approximately equal. The remaining OR, $(0.6 < y/h < 1.0)$, corresponds to the FSR, where the viscous dissipation exceeds any production of turbulence and is roughly equivalent to the rate at which turbulence is transported from the IR (Nakagawa et al., 1975).

In the VSL, Prandtl's mixing length model leads to Equation (4.2) (Nezu, 2005, Nezu and Rodi, 1986), where $U^+ = U/U_*$ and $y^+ = yU_*/\upsilon$. In the log-law layer, the mean flow can be described by Equation (4.3). Based upon experimental evaluation, κ and A for open channel flows have been found to be 0.41 and 5.29 for smooth beds, respectively (Nezu and Rodi, 1986). Equations (4.2) and (4.3) are valid for $y/h < 0.2$, additional models are required outside this region.

$$U^+ = y^+ \tag{4.2}$$

$$U^+ = \frac{1}{\kappa}\ln y^+ + A \tag{4.3}$$

Coles (1956) proposed that the deviation from the log-law in boundary layers outside of $y/h < 0.2$ could be accounted for by a wake function, Ψ. The resulting modification to Equation (4.3) are shown in Equation (4.4). The wake function parameter Π is equal to 0.55 for zero-pressure gradient boundary layers (Nezu, 2005).

$$\left.\begin{aligned} U^+ &= \frac{1}{\kappa}y^+ + A + \Psi \\ \Psi &= \frac{2\Pi}{\kappa}\sin^2\left(\frac{\pi}{2}\frac{y}{h}\right) \end{aligned}\right\} \tag{4.4}$$

Thus, from Equations (4.2), (4.3), and (4.4), it is possible to describe U^+ throughout the depth of open channel flows. Also, as $U_* = \sqrt{ghS_O}$ for uniform flow, it is also possible to describe U. Aside from the mean flow distribution in the channel, it is also necessary to describe the nature of the turbulent velocity fluctuations throughout the flow. Nezu (1977) showed that the turbulence intensity terms (RMS values), outside the VSL are independent of the Reynolds number, Re, and Froude number, Fr, and can be described by Equations (4.5), (4.6), and (4.7), with the empirically determined constants $D_U = 2.3$, $D_V = 1.27$, $D_W = 1.63$, and $C_K = 1$ (Nezu, 2005).

$$\frac{\sqrt{\overline{u'^2}}}{U_*} = D_U \exp\left(-C_K \frac{y}{h}\right) \tag{4.5}$$

$$\frac{\sqrt{\overline{v'^2}}}{U_*} = D_V \exp\left(-C_K \frac{y}{h}\right) \tag{4.6}$$

$$\frac{\sqrt{\overline{w'^2}}}{U_*} = D_W \exp\left(-C_K \frac{y}{h}\right) \tag{4.7}$$

The RMS value of u' in the VSL is given by Equation (4.8), which can be incorporated in Equation (4.5) to describe the velocity fluctuations throughout the depth of the flow, as shown in Equation (4.9) (Nezu, 2005), where $\mathrm{Re}_* = hU_*/\upsilon$, B has a value of 10, and $\Gamma = 1 - \exp\left(-y^+/B\right)$.

$$\frac{\sqrt{\overline{u'^2}}}{U_*} = 0.3y^+ \tag{4.8}$$

$$\frac{\sqrt{\overline{u'^2}}}{U_*} = D_U \exp\left(-\frac{y^+}{\mathrm{Re}_*}\right)\Gamma + 0.3y^+\left(1-\Gamma\right) \tag{4.9}$$

4.2.2 Spectral Model for Turbulence

Velocity fluctuations lead to the driving force behind the operation of the VTP method, therefore it is necessary to determine the spectral content of these velocity fluctuations. Experiments have shown that the power spectral density of u', Φ_{uu}, are self-similar when appropriately normalized, even under different flow conditions. An appropriate model is developed to describe Φ_{uu}, which can be leveraged in modeling the response of a structure to turbulent flow.

The power spectral density can be related to the spatial correlation function, $R_x(r)$, as shown in Equation (4.10), for two velocity measurements $u'(x)$ and $u'(x+r)$ separated by a distance r. Note that $R_x(r)$ can be measured experimentally. This correlation function has been shown to be an even function (Meechan, 1958), thus the power spectral density can be determined from the Fourier Cosine Transformation, as shown in Equation (4.11).

$$R_x(r) = \frac{u'(x)u'(x+r)}{\overline{u'^2}} \tag{4.10}$$

$$\Phi_{uu} = \frac{2}{\pi}\int_0^\infty R_x(r)\cos(kr)\,dr \tag{4.11}$$

The power spectral density Φ_{uu} is independent of flow conditions and turbulent flow structure when normalized by the mean eddy macroscale, L_x. Several models for

Φ_{uu} have been proposed to predict power spectral density for the production, inertial, and viscous subranges of turbulent flows. The two models considered in this analysis are the von Karman and Heisenberg models. These models are typically described in wave number space, k. However, under Taylors Hypothesis of frozen turbulence, it is possible to convert the parametric equations to frequency space, f, where $k = 2\pi f/\overline{U}$, where $\overline{U}$ is the depth-averaged mean flow velocity.

The von Karman spectrum, shown in Equation (4.12) (von Karman, 1948) is a function of L_x and the characteristic wavenumber/frequency, k_o.

$$\Phi_{uu} = \frac{2}{\pi} L_x \overline{u'^2} \left(1 + \left(\frac{k}{k_o} \right)^2 \right)^{-5/6} \tag{4.12}$$

The mean eddy macroscale can be determined from the measured correlation function, and corresponds to $L_x = \pi/2\,\Phi_{uu}(0)$ (Nezu and Nakagawa, 1993). The distribution of L_x has been determined experimentally and can be described by the relationship shown in Equation (4.13). The coefficient B_1 varies from 1.1 for an Re_* of 600 to 1.0 for an Re_* of 1600, where $\mathrm{Re}_* = hU_*/\upsilon$.

$$\left.\begin{aligned} \frac{L_x}{h} &= B_1 \left(\frac{y}{h} \right)^{1/2} \quad \text{for } \frac{y}{h} < 0.6 \\ \frac{L_x}{h} &= 0.77 B_1 \quad \text{for } \frac{y}{h} > 0.6 \end{aligned}\right\} \tag{4.13}$$

The characteristic wave number can be determined from mean eddy macroscale as shown in Equation (4.14), where the parameter C is the Kolmogorov constant with a value of 0.5 and K is given by Equation (4.15).

$$k_o = \left(K \left(\frac{2}{\pi C} \right)^{-1.5} \right)^{-0.4} L_x^{-1} \tag{4.14}$$

$$K = 0.691 + 3.98 \left(\mathrm{Re}_L \right)^{-0.5} \tag{4.15}$$

The Reynolds number, Re_L, in Equation (4.15) is based upon the RMS value of u' for the velocity scale and L_x for the length scale. The von Karman model corresponds to the production and inertial subranges of the turbulent energy spectral space, $0 \le k \le \lambda^{-1}$, where λ is the Taylor microscale of turbulence. Roughly, the von Karman model covers the open channel flow from the VSL to the ER. In the VSL, turbulence is produced and transported into the equilibrium region while in the ER the rate of production equals the rate of dissipation (Nakagawa et al., 1975).

Another model is required to overlap the von Karman model from the inertial subrange to the viscous subrange, where the production is zero and the viscous dissipation equals the rate of transport (FSR). This is achieved with the Heisenberg model, shown in Equation (4.16). The new terms introduced in Equation (4.16) include the dissipation rate for turbulent energy, ε, the constant γ', and the Kolmogorov microscale of turbulence, η.

$$\overline{u'^2} \Phi_{uu}(k) = C \varepsilon^{2/3} k^{-5/3} \left(1 + \gamma' (k\eta)^4 \right)^{-4/3} \tag{4.16}$$

The dissipation rate can be determined from Equation (4.17). The u' terms are typically not measured to the resolution required to construct an accurate representation of Equation (4.17). Therefore, it is common to exploit the isotropic turbulent assumption, leading to the right hand side of Equation (4.17) (Nezu and Nakagawa, 1993). This

assumption is an appropriate simplification, since turbulent fluctuations in all three directions are of the same order for open channel flows.

$$\varepsilon = 15\upsilon\left(\frac{\partial u'}{\partial x}\right)^2 = \frac{15\upsilon\overline{u'^2}}{\lambda^2} \tag{4.17}$$

The Taylor and Kolmogorov microscales λ and η are defined as shown in Equations (4.18) and (4.19), respectively. These microscales are practically solved via the fits employed in Equations (4.20) and (4.21). Lastly, the constant γ' is taken as 100, as it gives the optimal fit with measured and published results from Kironoto and Craf (1994) and Nakagawa and Nezu (1993).

$$\lambda = \sqrt{\frac{15\upsilon\overline{u'^2}}{\varepsilon}} \tag{4.18}$$

$$\eta = \left(\frac{\upsilon^3}{\varepsilon}\right)^{1/2} \tag{4.19}$$

$$\frac{L_x}{\lambda} = \left(\frac{K}{15}\right)^{1/2} \mathrm{Re}_L^{1/2} \tag{4.20}$$

$$\frac{L_x}{\eta} = K^{1/4}\,\mathrm{Re}_L^{3/4} \tag{4.21}$$

The aforementioned model describes the RMS values of the turbulent flow quantities with depth, along with the spectral representation of the turbulent quantities. The next step is to calculate dynamic pressure due to these velocity fluctuations.

4.2.3 Dynamic Pressure

In Equation (4.5), the RMS value of u' is defined, which can be coupled with Equations (4.12) and (4.16) to arrive at the spectral representation of the turbulent

fluctuations in the open channel flow. These turbulent fluctuations lead to a time varying dynamic pressure, which excites the VTP. This spectrum is a function of the position across the channel depth. Given the variation of $\sqrt{\overline{u'^2}}$, the dynamic turbulent pressure impinging on the VTP disk can be determined by integrating the pressure distribution across the disk diameter, Figure 4.3.

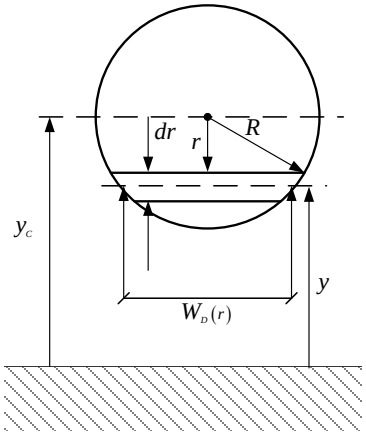

Figure 4.3: Area integration of dynamic turbulent pressure distribution across VTP disk.

At a point in the flow, the dynamic turbulent pressure spectrum is computed as shown in Equation (4.22). By integrating Equation (4.22) across the VTP, the average pressure quantity, $\bar{\Phi}_{PP}$, can be computed as shown in Equation (4.23), where r extends from the center of the VTP to the radius of the disk, R (see Figure 4.3). It is not convenient to integrate $\Phi_{PP}(r)$, however it is possible to replace this term with a function of y, as $y_C = y - r$. Additionally, the integrand in Equation (4.23) can be

replaced with the product of the differential radius dr and the element width, $W_D(r) = 2\sqrt{R^2 - r^2}$. The resulting expression is shown in Equation (4.24).

$$\Phi_{PP} = \left(\frac{1}{2}\rho\overline{u'^2}\right)^2 \Phi_{uu} \tag{4.22}$$

$$\bar{\Phi}_{PP} = \frac{1}{A_{VTP}} \int_{-R}^{R} \Phi_{PP}(r) dA \tag{4.23}$$

$$\bar{\Phi}_{PP} = \frac{1}{A_{VTP}} \int_{-R}^{R} \Phi_{PP}(r) W_D \, dr \tag{4.24}$$

4.2.4 Structural Response

Having established the variation of the dynamic turbulent pressure across the channel depth, it is necessary to relate the dynamic pressure to the response of the VTP. Following the method outlined in Blevins (1990), it can be shown that the response of a plate, for each mode, is described by Equation (4.25), where ω_i is the undamped natural frequency of mode i in radians/second, ζ_i is the modal damping factor, J_i is the joint acceptance, $p_i(t)$ is the turbulent dynamic pressure, and x_i is the displacement for mode i.

$$\frac{1}{\omega_i^2}\ddot{x}_i + \frac{2\zeta_i}{\omega_i}\dot{x}_i + x_i = J_i p_i(t) \tag{4.25}$$

In the case where the joint acceptance is unity, the mode shape and the pressure distribution are spatially correlated for a given mode (Blevins, 1990), and J is equal to 1. This results in the governing equation for a single degree of freedom oscillator. The steady state frequency response function of an oscillator, $\left|H(\omega)_i\right|^2$, to a random,

stationary, ergodic, and Gaussian pressure spectrum can be computed from Equation (4.25) as shown in Equation (4.26) (Blevins, 1990). As turbulence in open channels can be categorized as random, stationary, Gaussian, and ergodic (Blevins, 1990; Nezu and Nakagawa, 1993; Galanti and Tsinober, 2004), the dynamic turbulent pressure determined by these velocity fluctuations can be categorized in the same manner.

$$\left|H\left(\omega\right)_i\right|^2 = \frac{1}{\left(1-\left(\omega/\omega_i\right)^2\right)^2 + \left(2\zeta_i\,\omega/\omega_i\right)^2} \tag{4.26}$$

The response function shown in Equation (4.26) represents the transfer function from the input force to the displacement response of the structure. The power spectral density of the displacement for the VTP can be computed from the product of Equations (4.24) and (4.26). As the joint acceptance is not always unity, Blevins (1977) suggests a correction method that requires the inclusion of the joint acceptance. Also, as the input force is derived from the dynamic pressure, the characteristic modal pressure, $\tilde{P}_{iC}$, is included to arrive at a displacement response spectrum. The characteristic modal pressure at the center of the VTP is shown in Equation (4.27) (Blevins, 1977). The parameters in Equation (4.27) are the density of the VTP disk, ρ_D, the disk thickness t, and the displacement of the VTP center x_{iC}.

$$\tilde{P}_{iC} = \rho_D t\left(\omega_i\right)^2 \left|x_{iC}\right| \tag{4.27}$$

Equation (4.27) is then used to compute the displacement for mode i in physical units, Φ_{xxi}, as shown in Equation (4.28). Further, due to the Central Limit Theorem for random, independent processes, the mean squared sum of these processes is equal to the

sum of the mean square of the individual processes. Thus, given that the turbulence in open channels is stationary and random, the overall displacement response spectrum of the VTP can be computed from the sum of the individual responses of each mode i, shown in Equation (4.29).

$$\begin{aligned}\Phi_{xxi} &= \frac{\bar{\Phi}_{PP}}{\left(1-\left(\omega/\omega_i\right)^2\right)^2+\left(2\zeta_i\,\omega/\omega_i\right)^2}\frac{J_i^{\,2}x_{iC}^2}{P_{iC}^2} \\ &= \frac{\bar{\Phi}_{PP}}{\left(1-\left(\omega/\omega_i\right)^2\right)^2+\left(2\zeta_i\,\omega/\omega_i\right)^2}\frac{J_i^{\,2}}{\left(\rho_D t\left(\omega_i\right)^2\right)^2}\end{aligned} \tag{4.28}$$

$$\Phi_{xx} = \sum_i \Phi_{xxi} \tag{4.29}$$

Lastly, for random processes, the mean squared displacement response $\overline{x^2}$ can be related to the power spectral density, as shown in Equation (4.30) (Blevins, 1990). Velocity and acceleration response spectra and mean squared response values can be derived from Equations (4.29) and (4.30).

$$\overline{x^2} = \int_{f_1}^{f_2} \Phi_{XX}\,df \tag{4.30}$$

To solve Equation (4.28), it is necessary to include the natural frequencies and the modal damping factors. The natural frequency for a circular disk fixed at all boundaries (an appropriate approximation of the VTP device), can be calculated from Equation (4.31), where E_D is the modulus of elasticity for the disk, ρ_D is the density of the disk, υ_D is Poisson's ratio for the disk, and λ^2 varies from 10.22 to 21.26 for the first two modes (Blevins, 1979). An additional mode, which accounts for the mass of the

accelerometer located at the center of the VTP, is also required. The natural frequency for this mode can be calculated from Equation (4.31), where λ^2 equals 5.34, as discussed in Roberson (1951).

$$\omega_i = \frac{\lambda^2}{r^2}\left(\frac{E_D t}{12\rho_D t\left(1-\upsilon_D^2\right)}\right)^{1/2} \tag{4.31}$$

Another component of Equation (4.28) is the modal damping factor. Due to the presence of the fluid around the VTP disk, this damping will consist of the damping from the disk material itself, ζ_s, taken as 0.05 (Berger et al., 2003), and the fluid damping ζ_f. For moving channel fluid, the fluid damping can be estimated from Equation (4.32) with an appropriate substitution of the drag coefficient, C_D, taken as 1.28 for a plate in cross flow, and $\tilde{m}$ as the mass per unit length of the disk (Blevins, 1990).

$$\zeta_f = 2\frac{U}{\omega_i D}\frac{\rho R^2}{\tilde{m}t}C_D \tag{4.32}$$

Finally, it is necessary to consider the assumption regarding the joint acceptance. The joint acceptance can be computed from the mode shape, $\tilde{x}_i\left(r,\theta\right)$ and the pressure distribution, $\tilde{P}_i\left(r,\theta\right)$, (normalized by $m\left(\omega_i\right)^2$ for each mode) as shown in Equation (4.33). The parameters in Equation (4.33) are the mass per unit area m and angle θ, which varies from 0 to 2π.

$$J_i = \frac{\int_A \tilde{P}_i\left(r,\theta\right)\tilde{x}_i\left(r,\theta\right)drd\theta}{\omega_i^2\int_A m\tilde{x}_i^2\left(r,\theta\right)drd\theta} \tag{4.33}$$

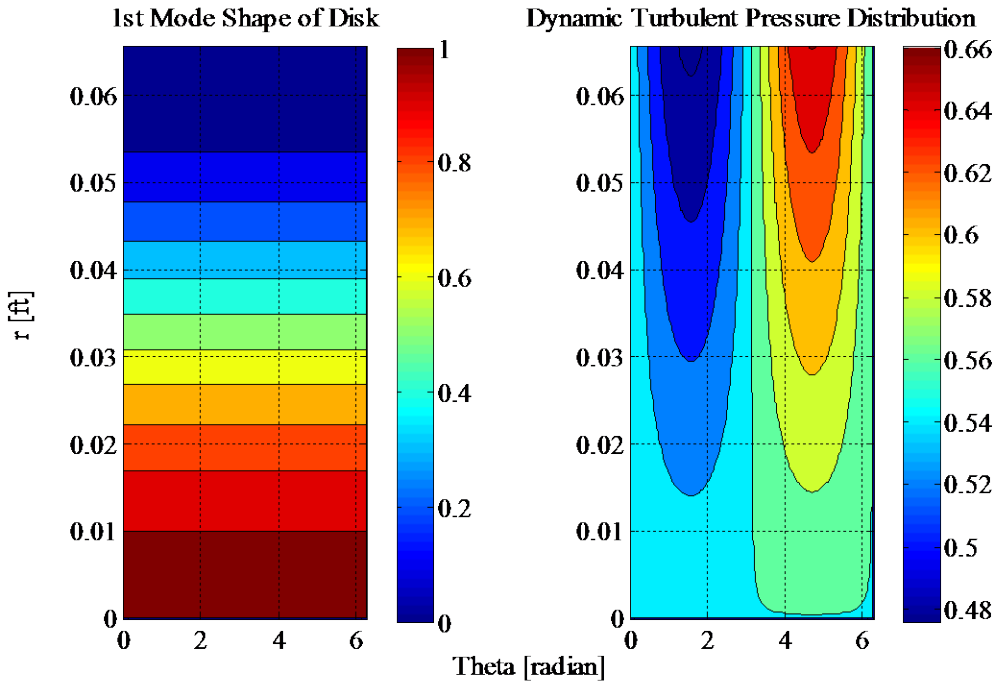

Figure 4.4: Components of the joint acceptance for the 1st mode of the plate.

For the first mode of the VTP disk, the mode shape and dynamic turbulent pressure distribution are shown in Figure 4.4. For the first three modes the joint acceptance values are 1.11, 1.06, and 1.83 respectively. The natural frequency of the subsequent modes, as will be shown in Section 3, are greater than 500 Hz, typically outside the range of the VTP response spectra and subsequently have a negligible impact on the mean squared response value. The joint acceptance values listed above are incorporated into the analytical model, Equation (4.28).

4.3 Model Verification, Calibration, and Validation

A numerical model is prone to errors that originate from the mathematical and the physical approximations of the problem. The errors and uncertainties introduced while solving the mathematical equations include round-off, discretization, and truncation errors. These errors are accounted for under the broad topic of model verification. The second source of error in a model arise from uncertainties introduced from an imperfect model definition of underlying physical principles as well as the imprecise values for the associated parameters of the chosen model (Atamturktur et al., 2012). Models and their associated parameters can be conditioned based on the experimental data to reduce the uncertainties and infer biases in model predictions. It is important to note that validation of a model requires a data set independent from those that are used in the calibration step (Trucano et al., 2002).

The following sections assess the predictive capabilities of the developed semi-empirical model and will be used for optimization of the field prototype. The verification activities involve investigation of the impact of the dynamic pressure integration across the VTP. This is then followed by a calibration of the model performance to an experimental data set in order to account for the variability inherent in the model input parameters. Finally, the model is validated by comparing the predictions against an independent data set.

4.3.1 Model Verification

It has been well documented (Nezu and Rodi, 1986) that the variation of u' across the channel depth is non-linear, with the peak occurring near the bed. Given that the

VTPs are designed to typically operate at $y/h < 0.3$, it is necessary to consider the variation in the turbulent velocity fluctuations across the depth of the VTP surface (generally having a diameter from 1.58 to 2.36 inch). In Equation (4.24) this is accounted for by integrating the pressure distribution, which is dependent on u', across the disk surface. To investigate the effect of the numerical integration step width, dr, for each element, the pressure is integrated with decreasing step width, as shown in Figure 4.5. The results reveal that after 10 element strips, the result for both y/h of 0.15 and 0.35 are within 1% of the 20 element result. From this result, it can be concluded that 15 elements are sufficient to capture the pressure variation across the VTP.

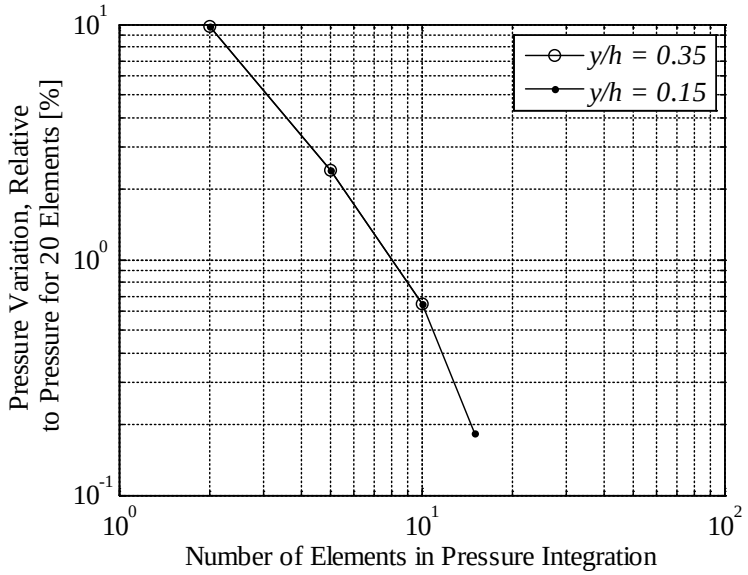

Figure 4.5: Variation in VTP turbulent pressure as a function of number of elements.

4.3.2 Model Calibration

Structural dynamic model: The parameter values used in the development of the model, reviewed in Section 2, are best estimates obtained from literature review. Therefore, it is necessary to condition the parameter values against the actual measured response of the structure. The parameters considered in this calibration include the disk material properties, E_D, ζ_D, and ρ_D, as well as the turbulent flow characteristics, U_*, ζ_F, and $\sqrt{\overline{u'^2}}$. The calibration of the disk parameters is accomplished by conducting an experimental modal analysis on the VTP disk and calibrating the predicted natural frequencies to the measured natural frequencies. The calibration of the turbulent flow quantities is accomplished via experiments conducted in the Clemson Hydraulics Laboratory (CHL) flume.

To calibrate the natural frequency predictions for the various modes in the VTP, model predictions are compared with the measured natural frequencies for a 0.13 inch thick, 1 inch radius, Neoprene rubber VTP. The measured values are obtained by rigidly fixing the VTP and attaching a shaker to the disk surface. The force transmitted to the plate is measured with a Bruel and Kjaer 8200+2646 force transducer, with a sensitivity of –17.78 mV/lb. The acceleration response of the VTP is recorded with a Kistler 8732A500 accelerometer, with a sensitivity of 2.94 mV/g. The neoprene test is conducted with a span of 800 Hz and 6400 lines, leading to a frequency resolution of 125 mHz. The excitation frequency in the shaker ranges from 1 to 1000 Hz bi-directionally at a rate of 125 Hz/s.

The comparisons between the calculated and measured natural frequencies are shown in Table 4-1 for the first six modes. For the higher modes, the prediction results are within 10% of the measured frequencies. The first mode is calculated including the presence of the accelerometer as a point mass. Model calibration can be completed to minimize the disagreements between the measured and calculated natural frequencies considering all six modes. However, the disagreement observed for the first mode is believed to be due to the stringer connecting the shaker to the VTP sensor. Also, the third observed mode is believed to be a spurious mode resulting from the interaction between the stringer and the VTP, which is not included in the model. Therefore, the first and the third modes are excluded from the calibration activities.

Table 4-1: Model and measured natural frequencies for modes in neoprene.

Mode Shape	Neoprene 30A			Calibrated Results	
	Model	Meas.	% Error	Model	% Error
1[1.]	80.17	70.3	14		
2	248	292	-15	260	-11
3[2.]	NA	366	NA	NA	NA
4	515	534	-3.6	540	1.1
5	845	773	9.3	886	15
6	963	903	6.6		

[1.] Affected by stringer mass & stiffness. [2.] Stringer/plate coupled mode.

The natural frequencies presented in Table 4-1 are dependent upon the model parameters E_D, ρ_D, t, and R. The geometric parameters t and R are design parameters, which can be controlled during the manufacturing of the prototype, and thus are known with high certainty. Furthermore, the density parameter can be measured with relative ease and high accuracy. The only other parameter that needs to be quantified is

the Young's Modulus of the plate, which nominally is selected as 1.73×10^5 psf. An optimal fit is achieved considering modes 2, 4 and 5 with a 10% increase in the modulus of the disk while all other parameters remain at their nominal values. The results of this analysis are also shown in Table 4-1. As indicated, the predictions for modes 2 and 4 improve with the calibration in the model parameters. This represents an optimal fit since the contribution of each mode to the overall response is not equal. Mode 2 contributes 100 times more to the overall measured acceleration response than mode five. Thus a 4% reduction in the percent error for mode 2 is significant.

Turbulence Model: To calibrate the turbulence characteristics developed in the semi-empirical model, channel velocity is measured in the CHL flume with a Sontek acoustic Doppler velocimeter (ADV), A701F, at 50 Hz. The sample time of five minutes is found to adequately capture all eddy scales. The flume bed consists of quartz sand with a median grain size of 0.06 inch. The velocity measurements are made throughout the depth, from y/h of 0.10 to 0.60. Pertinent flow parameters for each of the three runs are provided in Table 4-2.

Table 4-2: Flow parameters for CHL flume tests.

Run	h [ft]	U [ft/s]	U_* [ft/s]	Re_* [N.A.]
1	0.96	1.17	0.07	6360
2	0.87	1.02	0.05	3710
3	1.07	0.90	0.052	4560

It is also necessary to determine the value for U_*, an input for the turbulent channel flow model. This can be accomplished from the measured results in two ways.

Equation (4.3) can be fit, using the least squares method, to the measured values of U within the LLL. The coefficient of this fit is equal to the quotient of U_* and κ. Since the von Karman constant is known, this coefficient can be solved for the friction velocity. A second approach considers the contribution of the velocity gradient and the turbulent shear stress to the bed shear stress. The offset of a liner fit through the product $-\rho u'v'$ as a function of y is equal to the bed shear stress, τ_o, which can be related to the friction velocity as shown in Equation (4.34). These two methods yield similar results for runs 1-3. The friction velocity values shown in Table 4-2 are based on the first method. The fitted curves through these data points are shown in Figures 4.6 and 4.7.

$$U_* = \sqrt{\frac{\tau_o}{\rho}} \tag{4.34}$$

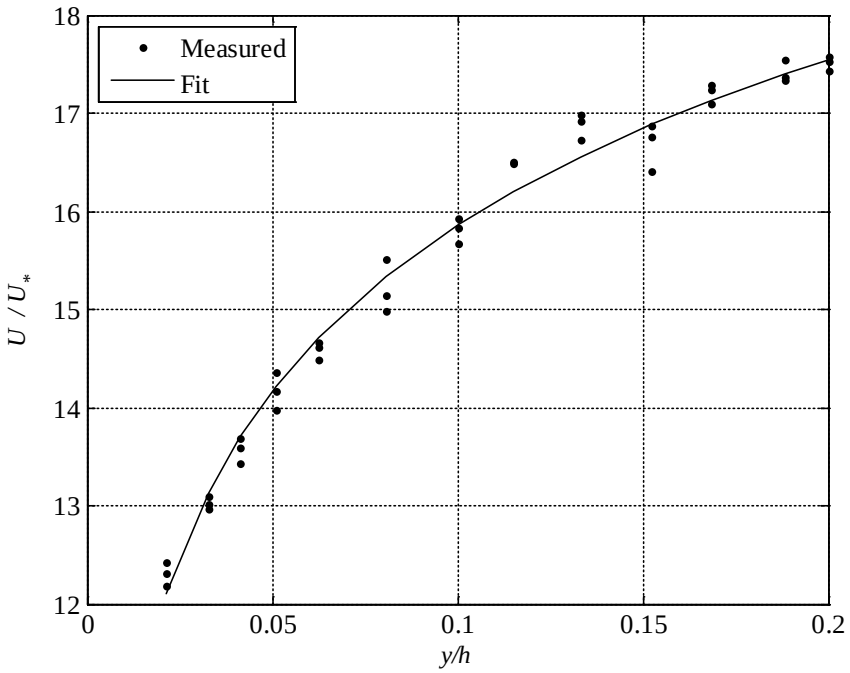

Figure 4.6: Distribution of velocity as a function of depth in the channel for run 1.

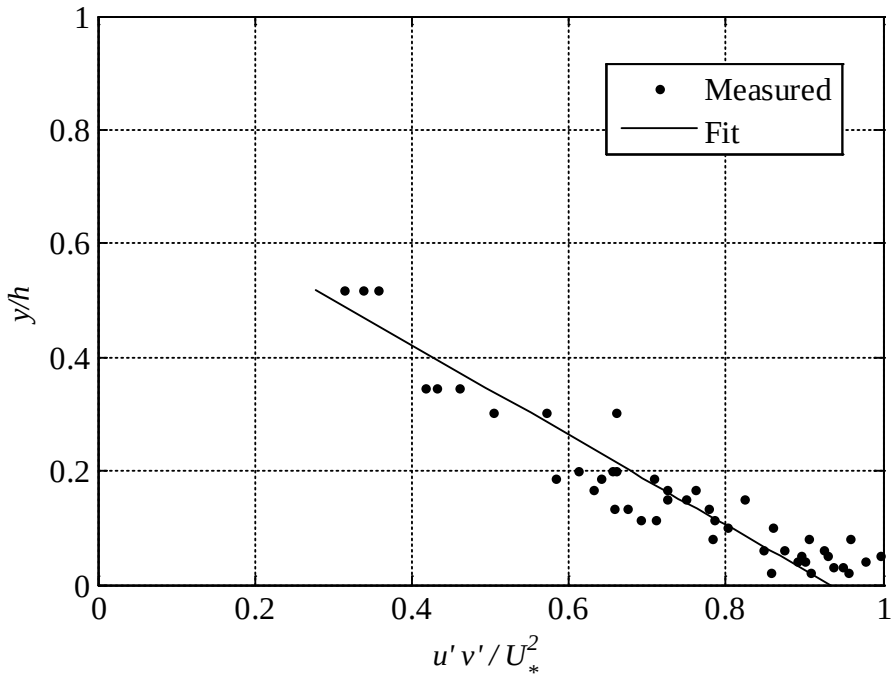

Figure 4.7: Distribution of $u'v'$ as a function of depth in the channel for run 1.

With U_* determined, it is then possible to compute the analytical model response for the turbulent fluctuations as a function of depth. The velocity fluctuations are computed using Equation (4.5) and compared with the measured results, as shown in Figure 4.8. The coefficient of determination between the measured values and the model is 0.73 for run 1, 0.87 for run 2, and 0.82 for run 3, indicating an acceptable representation of the measured data by the turbulence model.

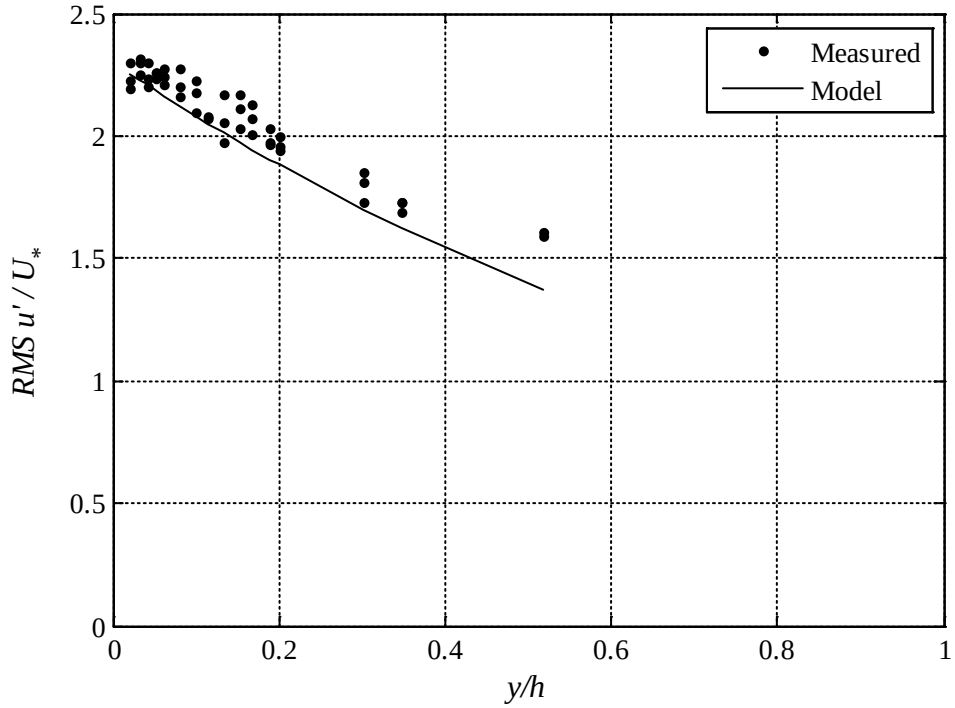

Figure 4.8: Measured and model root mean square of u' normalized by friction velocity as a function of relative depth in the channel (run 1).

In addition to the turbulent velocity fluctuations, the semi-empirical model must accurately represent the velocity spectrum. Several spectra are available in the published literature, two of which are shown in Figures 4.9 and 4.10. Figure 4.9 shows the comparison of the model predictions against the data published by Kironoto and Graf (1994). As shown in the Figure 4.9, the model fit falls within the published data set. The coefficient of determination is 0.89. Similarly, the comparison of the model results with the data published by Nakagawa and Nezu (1993) is shown in Figure 4.10, where the coefficient of determination is 0.97. The results shown in Figure 4.10 indicate that the model captures the same trend as the measured data.

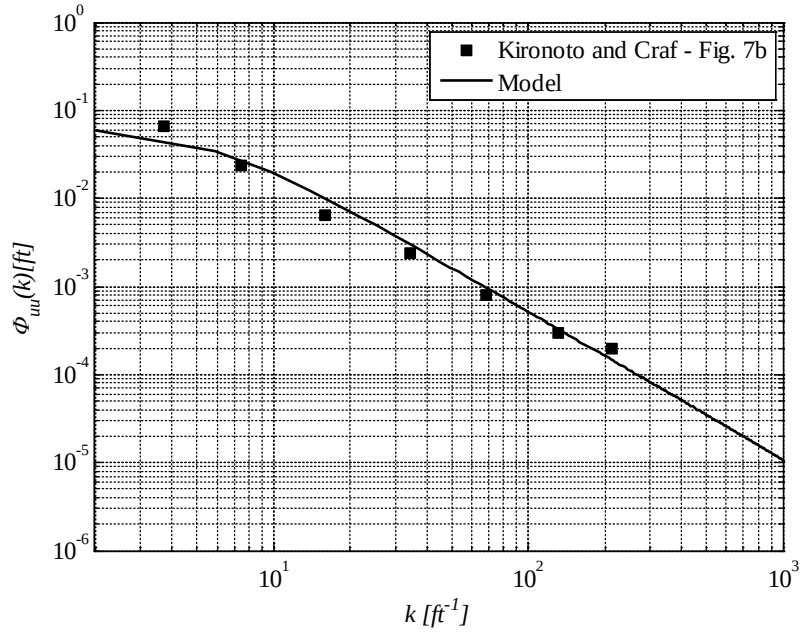

Figure 4.9: Comparison of model turbulent velocity fluctuation spectrum with published results from Figure 7b of Kironoto and Craf (1994).

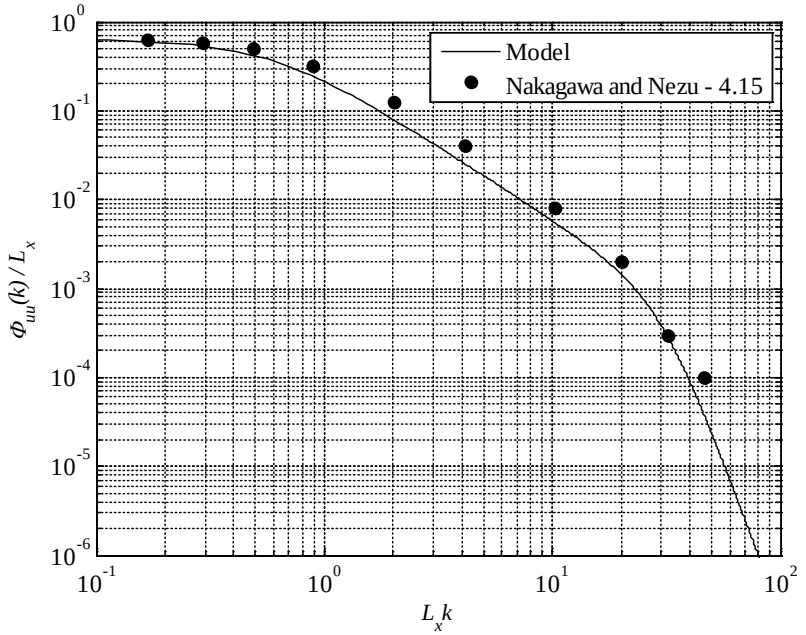

Figure 4.10: Comparison of model turbulent velocity fluctuation spectrum with published results from Figure 4.15 of Nakagawa and Nezu (1993).

Turbulent spectrum can also be constructed from the measured ADV data for runs 1-3. The power spectral density of the turbulent velocity fluctuations for run 1, for y/h of 0.1, 0.2, and 0.3 are shown in Figures 4.11 through 4.13, respectively. The figures indicate that the model captures the shape and magnitude of the measured turbulent spectra, with coefficient of determination of 0.87, 0.79, and 0.92, respectively. For the higher frequencies, the model results under-predict the measured spectra. This deviation is expected due to the nature of the ADV measurements. It is possible to correct the measured data as discussed in Hurther and Lemmin (2001). However, this requires a sonar device with a fourth probe to correct for the noise in the measured signal. The Sontek ADV device used in this study is not equipped with this additional probe, so this correction is not possible.

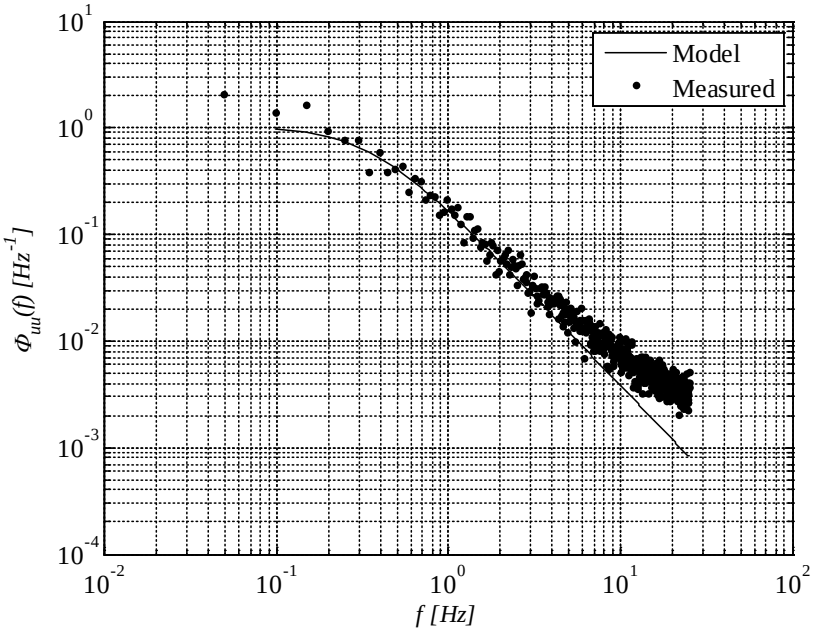

Figure 4.11: Power spectral density of u' at y/h of 0.1 from run 1.

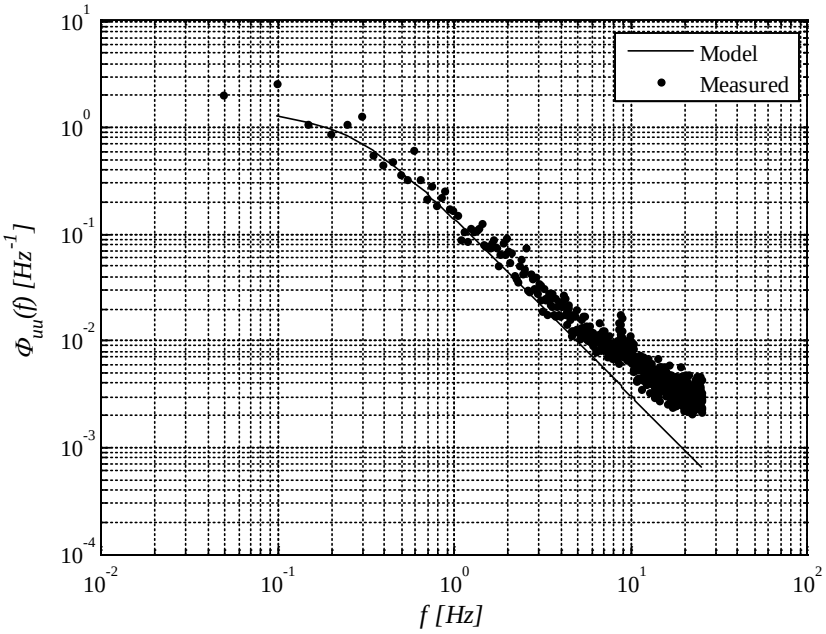

Figure 4.12: Power spectral density of u' at y/h of 0.2 from run 1.

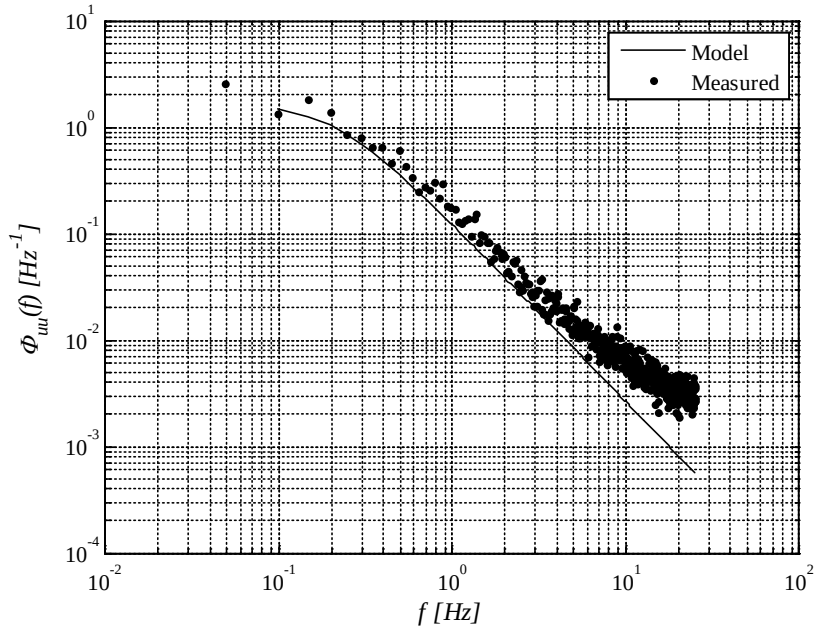

Figure 4.13: Power spectral density of u' at y/h of 0.3 from run 1.

Figures 4.9 through 4.13 reveal that the power spectral density of the u' velocity fluctuations as presented in the turbulence model is in agreement with both published spectra and those measured in the CHL flume. In addition, the magnitudes of the velocity fluctuations, shown in Figure 4.8, correspond to the measured values obtained with the ADV measurements. Thus, it can be concluded that the semi-empirical model component for the turbulent open channel flow does not require calibration in order to predict the magnitude and spectra of u'.

The objective of the semi-empirical model is to predict the mean squared acceleration response of the VTP. These results will also have to be calibrated in order to use the model for prediction and optimization of the VTP for field deployment. Data sets corresponding to the conditions for Run 1 are recorded experimentally, as discussed in Chapter 3, and are used to calibrate the model result. The measured VTP energy content response is recorded at y/h of 0.16 and 0.51. The mean energy content from this data set for the lower VTP is 0.24 ft^2/s^4 with a standard deviation of 0.016 ft^2/s^4. The model predictions for this VTP's mean energy content is 1.51 ft^2/s^4. For the upper VTP, the mean energy content is 0.16 ft^2/s^4 with a standard deviation of 0.011 ft^2/s^4. The model predictions for this VTP's mean energy content is 0.06 ft^2/s^4. Based upon these results, it is necessary to calibrate the model. The objective of the calibration is to configure the results such that the model predictions are within 10 times the standard deviation of the measured energy contents for the various positions within the channel. This will result in a calibrated model that can predict the VTP energy response within the appropriate order of magnitude but does not overly constrain the response. Since the model is being used to

determine the geometry of the prototype, this will ensure that the predicted results are sufficiently accurate to capture the difference between VTPs located in the sediment and in the flow.

The remaining parameters under consideration for calibration include the combined structural and fluid damping, the friction velocity, the mean flow velocity, and a factor introduced in Equation (4.22) that accounts for variations in the proportionality of the turbulent velocity fluctuations to the dynamic pressure. These parameters are varied by up to 20%. The largest variation in the model response occurs for the friction velocity, resulting in a variation in the mean energy content of up to 80%. Given this variability in the model results, U_* is chosen for calibration. Based upon the measured variation in the model response as a function of position within the channel flow, the friction velocity is calibrated by a linear function of position, with a slope of 0.833 and an intercept of 0.668. The resulting model predictions are 0.39 and 0.16 ft^2/s^4 for y/h of 0.16 and 0.51, respectively, a significant improvement in the model results. The model is conditioned based on the measured data during calibration and thus, it is necessary to validate the model by comparing the predictions against an independent data set.

4.3.3 Model Validation

The data set used for validating the analytical model consists of the measurements taken during Run 3, an independent data set not used for calibration. The measured VTP responses are recorded at positions in the channel at y/h of 0.35 and 0.66. The measured energy content response for each VTP is 0.14 and 0.085 ft^2/s^4 for the lower and upper

VTPs respectively. Using the calibrated model, the predictions are 0.17 and 0.081 ft^2/s^4 for these two positions, which are within the desired model tolerance.

In addition to computing the mean squared energy content response for the VTPs, it is also possible to compare the measured acceleration power spectral density with the model predictions. For the two VTP positions, the measured and model acceleration power spectra are shown in Figures 4.14 and 4.15, respectively. In addition to the synthesized modal response of the VTP, the first three modes of the VTP are also shown in order to highlight their contribution to the overall response. As shown in Figures 4.14 and 4.15, the results indicate that the first mode is responsible for the majority of the low frequency response. The model response for the first mode also indicates that the model mode is underdamped relative to the measured response. This suggests that further refinements in the model are possible. However, given that the objective of the model development is to optimize a field deployable scour monitoring device, the current model precision is acceptable.

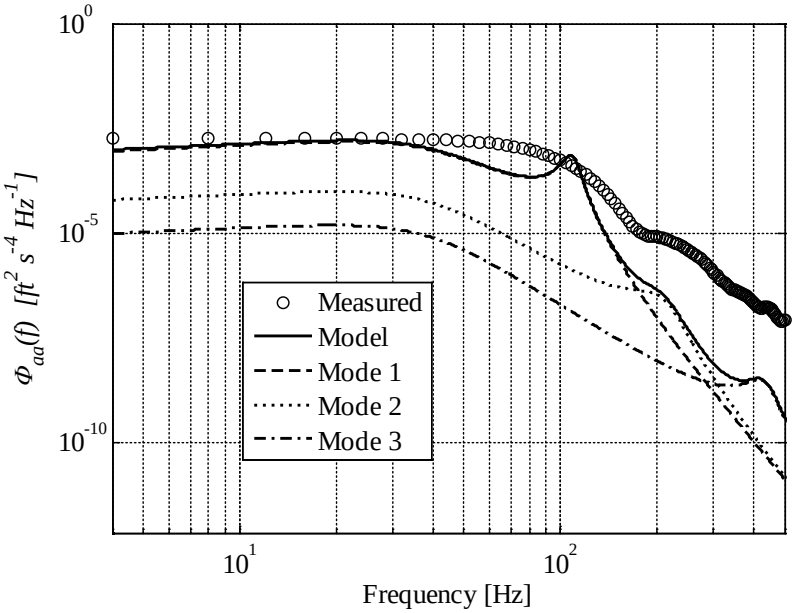

Figure 4.14: Measured and model acceleration response spectra for run 3 at y/h of 0.35. VTP plate is neoprene (0.063 inch thick, 0.787 inch radius).

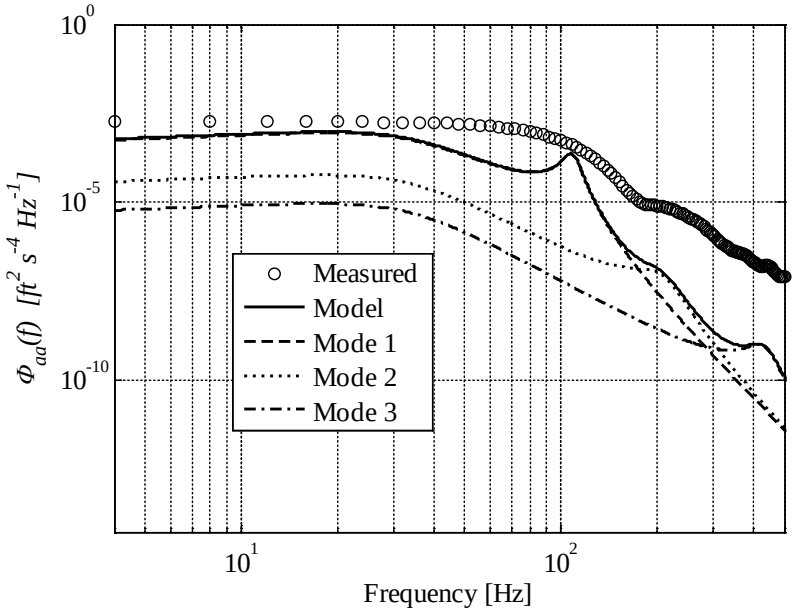

Figure 4.15: Measured and model acceleration response spectra for run 3 for y/h of 0.66. VTP plate is neoprene (0.063 inch thick, 0.787 inch radius).

4.4 VTP Optimization for Field Deployment

Having verified, calibrated, and validated the model, it is appropriate to use the model to predict the VTP energy content as the geometry of the device changes. In Chapter 3, it has already been shown that nonmetallic disks for the VTP are preferred over metallic disks, due to the lower stiffness, and higher acceleration response for a given turbulent dynamic pressure. Additionally, the circular VTPs are preferred over square geometries. Therefore, the optimization for field deployment considers only the radius and thickness of the disk as design parameters.

From the measured results of the VTP energy content presented in Chapter 3, it was determined that the maximum response from the VTPs located in the sediment was 0.1 ft^2/s^4. In order to ensure the response of the VTP located in the flow is at least one order of magnitude greater than the VTPs in the sediment, threshold energy content value is set to 0.11 ft^2/s^4. This ensures that the VTP device can be used for scour monitoring. Additional constraints imposed on the optimization process include that the resolution of the device is at least equal to that of a magnetic sliding collar, which can resolve the bed depth to 6 inch (Lagasse et al., 1997). Also, the material selected should be able to withstand the conditions that are likely to occur in the field. Given the performance of the neoprene in the experimental results conducted in Chapter 3, the decision is made to select this material for the field deployment. To overcome any risk to the probe due to the selection of neoprene for the VTP plate, each VTP is isolated to prevent failure in one sensor from affecting the remaining sensors installed on the probe.

Based upon the conditions discussed previously, several predictions are made with the analytical model for VTP thicknesses of 0.063 to 0.126 inch and radii from 0.6 to 1.38 inches. The results are shown in Figure 4.16.

The results reveal that the optimal VTP for a thickness of 0.063 inch has a radius of 0.787 inch. For the 0.126 inch thick neoprene, the minimum radius is determined to 1.38 inches. From these results, it is determined that the 0.063 inch thick neoprene of 0.787 inch radius is preferred over the thicker and larger VTP due to the improved resolution achievable with the smaller device. As expected, the model indicates that the energy content is higher for the thinner VTPs for the same dimension. Therefore, the minimum flow rate that can be achieved with the smaller, thinner VTP will exceed that for the larger, thicker VTP. To mount the sensor and the necessary hardware a clear spacing of 2.4 inches is required between the adjacent VTPs. This amounts to center to center distance between the adjacent VTPs and bed detection resolution of 4 inches, which is better than that provided by the MSC.

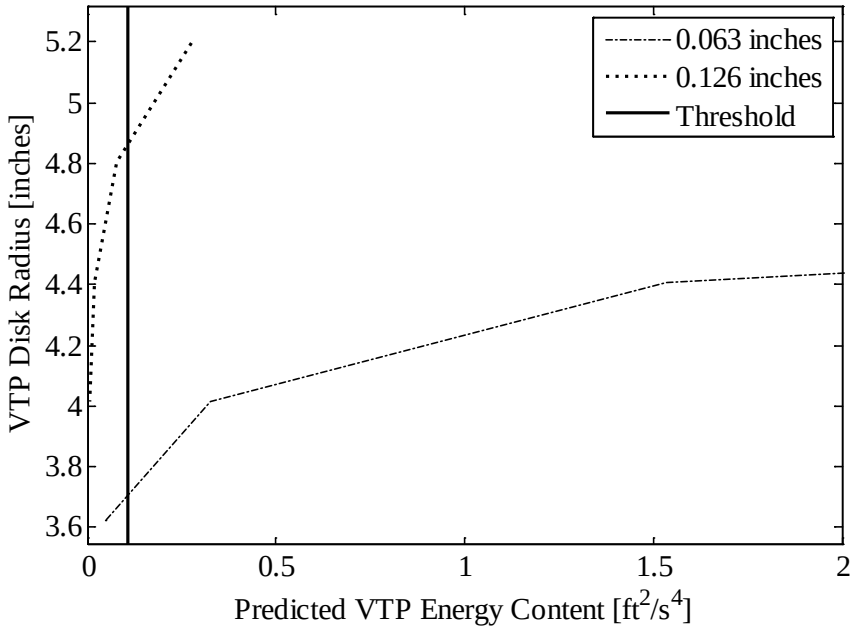

Figure 4.16: Optimization of VTPs' size and thickness for field deployment.

4.5 Field Prototype Performance

Based upon the results presented in Section 4 of this work, the optimal VTP configuration is determined to have a disk radius of 0.787 inch and a thickness of 0.063 inch. A field prototype is constructed with 8 VTPs distributed along a 3.28 ft length of an aluminum support pipe with 4-inch diameter. The VTPs are spaced 4 inches apart and housed within removable units which are designed to aid maintenance in the field and to ensure that damage to one device does not allow water to penetrate into the undamaged VTPs. A schematic of the device is shown in Figure 4.17. The fully assembled prototype is shown in Figure 4.18. The accelerometers installed in the field prototype are PCB model 352A24, with a sensitivity of 3.05 mV/ft/s^2. The accelerometers are connected to the bulkhead, as shown in Figure 4.17, in order to provide a water tight seal through

which the accelerometer signal is routed. On the interior of the pipe, the signal is carried by a wiring harness to the top flange of the pipe, where it passes through a water tight bulkhead and into a wet-mateable fitting for connection to the data lines and the data collection units.

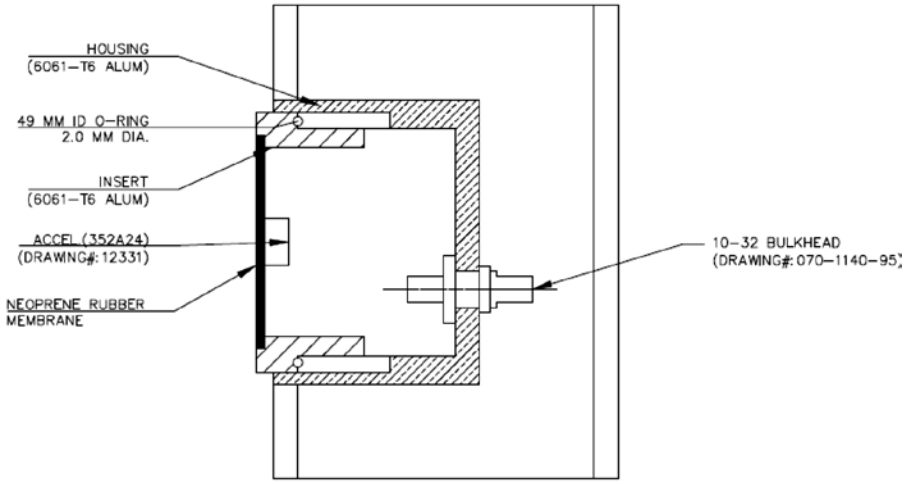

Figure 4.17: Schematic of field VTP configuration.

Figure 4.18: Field prototype.

4.5.1 Measured Energy Content Profile

The fully assembled field prototype is tested in the CHL flume to ensure the performance of the device. Tests are conducted in the channel flow with velocities ranging from 0.47 to 0.97 ft/s. The results from these tests are shown in Figure 4.19.

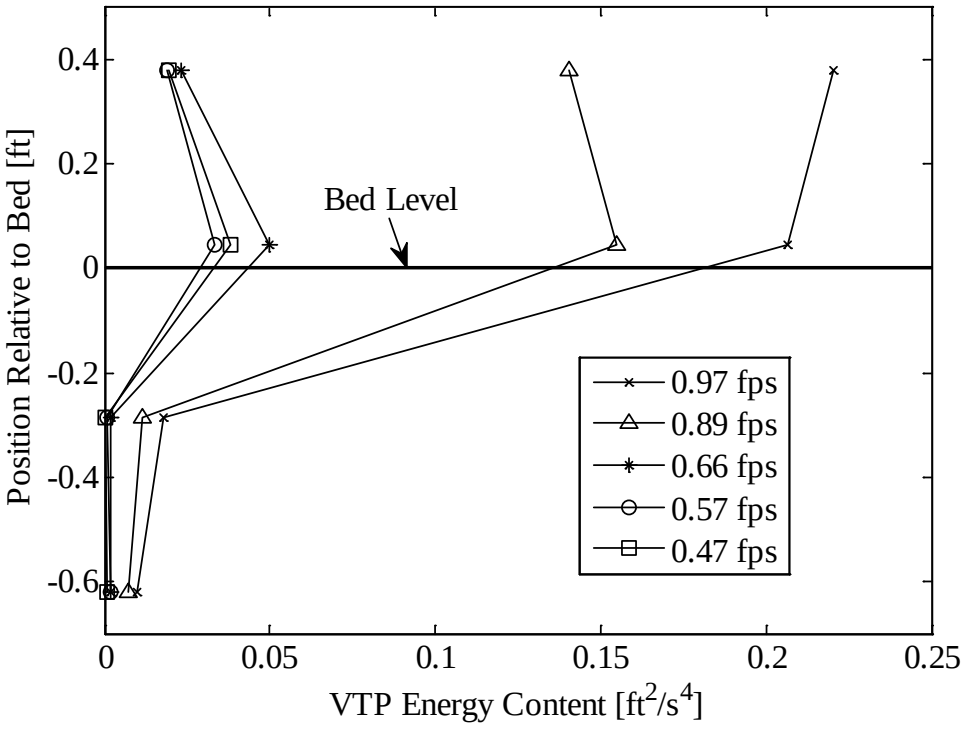

Figure 4.19: Performance of the field prototype in CHL flume at different velocity.

The results indicate that the VTP located in the channel flow and closest to the bed surface responds with energy content that is at least one order of magnitude greater than the VTPs in the sediment. Therefore, it is possible to conclude that the objective of the model development and optimization process has produced a device that will meet the required field performance metrics. Additionally, the results in Figure 4.19 indicate that

for the velocity in the range of 0.47 to 0.66 ft/s, the energy content of the VTP in the flow closest to the bed varied from 0.033 to 0.05 ft^2/s^4. These values are lower than the design threshold in the optimization; however, the ratio of the energy content between the VTP located in the flow and that in the sediment for these three cases ranges from 20 to 31. Thus, even for the low velocity cases, the field prototype will still indicate the water/sediment interface and therefore can monitor any scour hole development.

4.5.2 Measured and Predicted Sensitivity to Flow Misalignment

The field prototype is also tested against varying flow misalignment between the main flow and the VTP axis. The results from these tests are compared against the semi-empirical model, which is shown in Figure 4.20. The model and measured results reveal that as the misalignment increases, the response from the VTP decreases. The model response approaches the measured results for smaller angles of misalignment. As the misalignment increases, the model results begin to deviate from the measured results. This is expected, as the flow around the probe will begin to separate at the upstream edge of the VTP with increasing misalignment. This effect is not accounted for in the analytical model. Despite this, the model is able to capture the measured decay in energy content with increasing misalignment. This serves to confirm that the semi-empirical model is capturing the governing physics that dictate the VTP energy content response.

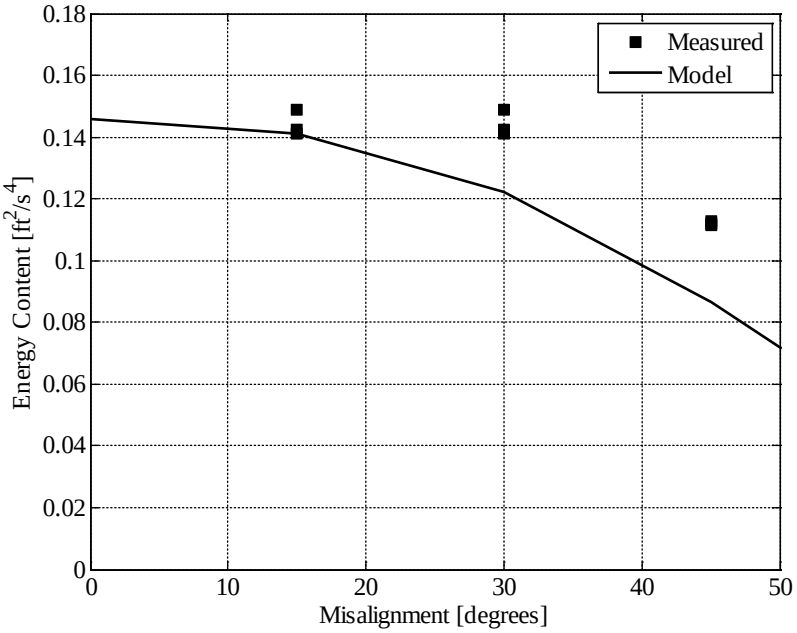

Figure 4.20: Measured and analytical model response as a function of flow misalignment.

4.6 Summary

A semi-empirical model that can predict the energy content response of a flexible plate to turbulent open channel flow is developed. This model includes an empirical relationship between channel conditions and turbulent velocity fluctuations. The turbulent flow model is coupled to a dynamic structural response model which translates variations in the dynamic turbulent pressure impinging on the VTP into a prediction of the mean acceleration response.

A mesh refinement study is conducted to determine the number of elements across the VTP surface required during integration of surface pressure. The study shows that result converge to within 1% of its final value for an element number greater than 10. Furthermore, the first three natural frequencies are calibrated with a 10% increase in the

modulus for the neoprene disk. The turbulent model calibration is investigated and reveals that the measured and predicted values are within the expected measurement error and is not adjusted. The final calibration showed that the model is sensitive to the friction velocity, which is then calibrated against a measured data set.

The calibrated model is then validated against an independently measured data set and reveals that the predicted values are within the desired tolerance of 0.16 ft^2/s^4. The predicted responses from the calibrated model range from 3 to 22% of the measured energy content responses for the independent data set. This represents a significant improvement in the model over the uncalibrated model.

After calibrating the model, a VTP is optimized for field deployment by considering variations in the VTP size and thickness. Optimal thickness is determined to be 0.063 inch while the ideal radius is determined to be 0.787 inch. The resulting device is sensitive to the turbulent velocity fluctuations while also being sufficiently robust for field deployment.

Based upon the optimized results, a field prototype is developed and tested in the laboratory. These tests indicate that the energy content variation across the channel depth is sufficient to allow for a determination of the water/sediment level. The model also captures the decay in energy with increasing flow misalignment.

CHAPTER 5

ROBUSTNESS OF THE SELECTED SCOUR MEASURING DEVICES

5.1 Introduction

Sonar and time domain reflectometer (TDR) are the most commonly used instruments for measuring scour depth as has been demonstrated in Chapter 2. This chapter focuses on these two devices to determine how the channel conditions such as temperature, salinity, and turbidity may affect the measurement accuracy of scour depth. In addition, the sensitivity of the VTP for different bed sediment types, flow alignment, turbidity, and flow velocity is also evaluated. Understanding the impact of these conditions on the performance of the scour monitoring methods is essential for a successful selection of an instrument for field deployment.

To study the variability in the measured scour depth due to channel conditions, an experimental campaign was undertaken to evaluate the performance of sonar fathometer, TDR, and VTP under various field conditions. These conditions include, where appropriate:

- Saline conditions, from 0 to 35.5 ppt;
- Water temperatures, from 41 to 104°F;
- Water with suspended sediments, for turbidities up to 900 NTU, including stratification effects;

This chapter is adapted from the article published by Fisher et al. (2013b) based on the work done for this project.

- Scour hole size;
- Flow alignment;
- Flow velocity;
- Bed sediment type.

5.2 Previous Studies of Factors Affecting Sonar

The speed of the acoustic pulse, given in Equation (2.1), is assumed to be constant. However, it has been shown to vary with temperature, salinity, and depth (Kuwahara, 1939; Leroy, 1969; Urick, 1975; Mackenzie, 1981). For a typical temperature variation from summer to winter of 86 to 50 °F, corresponding errors in a sonar measurement due to changes in the speed of sound are shown in Figure 5.1. The three curves correspond to the equations for the speed of sound, as presented by Mackenzie (1981), Kuwahara (1939), and Leroy (1969) which are given by Equations (5.1), (5.2), and (5.3), respectively. In these equations, c is the speed of sound in ft/s, T is the temperature in degrees Fahrenheit, S is the salinity in ppt, and D is the depth in ft. For a temperature change of 68 °F, a sonar transducer can have an error up to 4% in the distance to the riverbed. In turn, that 4% would correspond to nearly 0.5 ft for an initial depth of 12.3 ft. This is several times larger than the typical resolution of the device (about 0.1 ft) and thus, cannot be ignored.

$$\begin{aligned} c = {} & 4753.806 + 8.368\left(T-32\right) - 5.371\times10^{-2}\left(T-32\right)^2 + \\ & 1.336\times10^{-4}\left(T-32\right)^3 + 4.396\left(S-35\right) + 1.630\times10^{-2}D + \\ & 5.105\times10^{-8}D^2 - 1.868\times10^{-2}\left(T-32\right)\left(S-35\right) - \\ & 3.685\times10^{-14}\left(T-32\right)D^3 \end{aligned} \tag{5.1}$$

$$c = 4740.814 + 8.501(T-32) - 0.056(T-32)^2 + 4.288\times(S-35) + 0.01815D \tag{5.2}$$

$$c = 4897.966 + 9.843(0.556T - 27.778) - 1.969\times10^{-2}(0.556T - 27.778)^2 - 1.312\times10^{-1}(0.556T - 35.778)^2 + 3.937(1000S - 35) - 3.281\times10^{-2}(0.556T - 35.778)(1000S - 35) + D/61 \tag{5.3}$$

Similarly, the changes in the speed of sound due to salinity must also be considered. Variations occur in coastal waterways subject to tides or for inland waters during rainfall events, where the runoff could contain chemicals and other pollutants that would change the apparent salinity. The impact of changes in the salinity of the channel flow on sonar can also be evaluated by Equations (5.1), (5.2), and (5.3). Figure 5.2 reveals an increase in the uncertainty of approximately 2% in the scour measurements due to salinity effect relative to the speed of sound at 68°F.

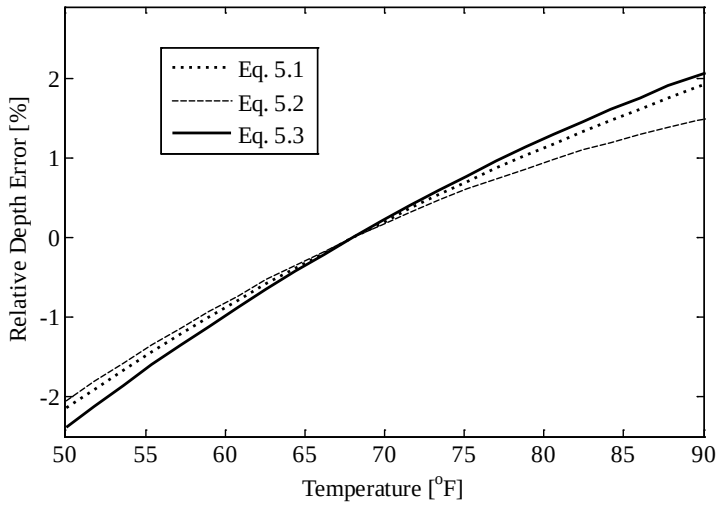

Figure 5.1: Relative error in distance measurements due to temperature changes, relative to the value at 68°F ($c = 4920$ ft/s).

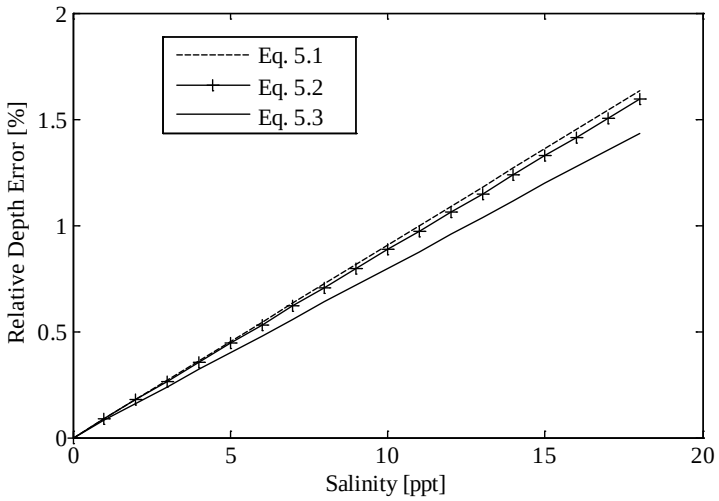

Figure 5.2: Relative error in distance measurements due to salinity, relative to the speed of sound at 68°F.

In addition to being affected by the temperature and salinity of the water, the accuracy of measurements can depend upon the nature of the bed itself. Natural riverbeds typically have a defined transition between the water density, ρ_0, and bed density, ρ_2, with an intermediary density between that of the sediment and the water, ρ_1. This transition is typically defined by an initial step change from the water density to the near surface sediment density followed by a gradual transition to the final deep bed density (Hamilton, 1980), as shown in Figure 5.3. Robins (1990) presented a model for the propagation of sound waves in a fluid of varying density and developed a generalized model for the response of the sound wave as it encounters a density gradient. The reflection coefficient, defined as the ratio of the reflected signal to incident signal at an interface, can be affected by the stratification of sediments along the sonar pulse. For the general case described above, the result is a complex function of vertical wave number,

k_z, which is the ratio of signal frequency to speed of sound. In general, the reflection coefficient is a function of the lower-bed density, the water density, the intermediate zone density, the density gradient thickness, h, and k_z. Robins (1990) showed that as the product $k_z h$ approaches zero and infinity, the reflection coefficient approaches values as shown in Equation (5.4).

$$\begin{aligned} \underset{k_z h \to 0}{R} &\to \frac{\rho_2 - \rho_0}{\rho_2 + \rho_0} \\ \underset{k_z h \to \infty}{R} &\to \frac{\rho_1 - \rho_0}{\rho_1 + \rho_0} \end{aligned} \tag{5.4}$$

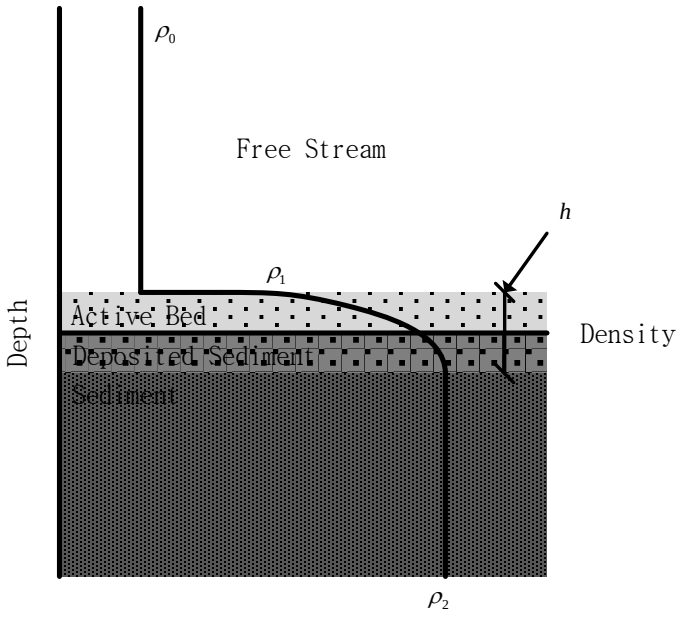

Figure 5.3: Density variation in the channel flow, adapted from Robins (1990).

The implication of the results shown in Equation (5.4) is that at lower $k_z h$, and in turn at lower frequencies, the reflected signal is only a function of the density difference

between the final bed density and the water density and is independent of the intermediate value. Conversely, as the frequency increases the model predicts that the reflection is from the initial step change between the channel and the riverbed. Stoll and Kan (1981) developed a more complex model that accounts for the effects of a porous, viscoelastic, saturated sediment and included the losses associated with the propagation of sound waves in the sediment structure and the saturated pores. The model, which includes the effects of porosity, grain size, permeability of the sediment, and internal stresses, predicts the reflection coefficient as a function of the incidence angle and acoustic signal frequency. Stoll and Kan's (1981) results for incidence angles less than 50° are relatively insensitive to frequency and collapse to Robins'(1990) results for low vertical wave number. Above 50°, the model predicts a reflection coefficient that is a function of frequency and rapidly approaches a value of 1.0. The Stoll and Kan (1981) model for varying incidence is useful for scenarios where the sonar waves are not perpendicularly incident on the riverbed. However, for the typical configurations seen in river scour monitoring, the model developed by Robins (1990) will suffice.

To explore Robins' (1990) model, the reflection coefficient is plotted in Figure 5.4 (a, b) as a function of the riverbed density (saturated sediment density) and the intermediary material concentration, respectively. Figure 5.4 reveals that for various bed densities, the reflection coefficient varies in the range of approximately 0.2 to 0.32. Typical value of near bed suspended sediment concentration is about 0.62 lb/ft^3 (Gray et al., 2003) for which the reflection coefficient is 0.003. Thus the wave will pass through

the intermediary layer with only a minor reflection occurring at the interface level. This is beneficial if an active bed is present in the channel.

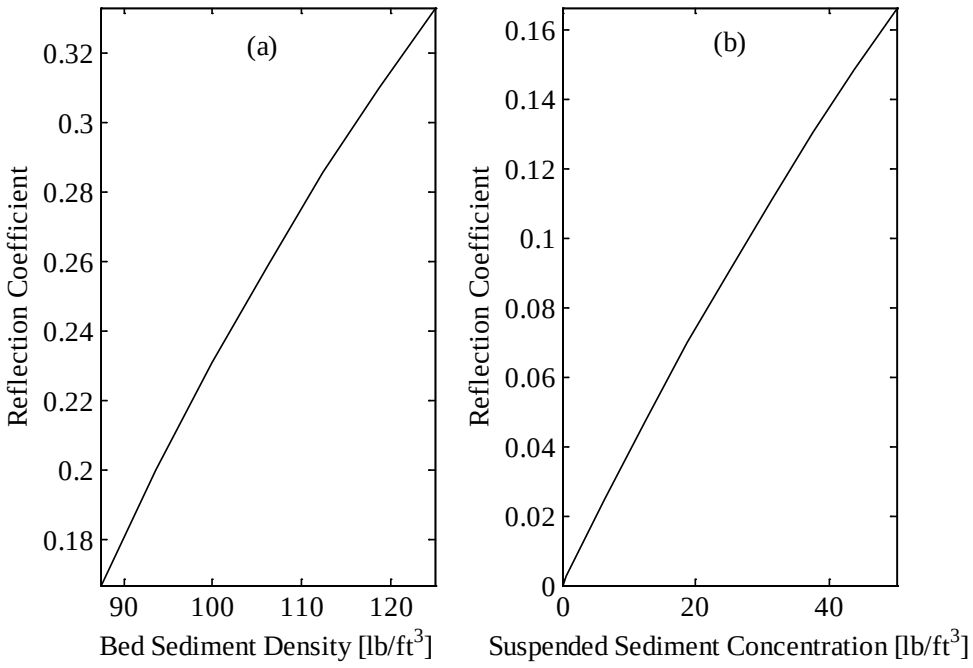

Figure 5.4: Reflection coefficient versus (a) sediment unit weight, (b) suspended sediment concentration. The reflection coefficient is calculated for density ratios according to the Robins (1990) model with a water density of 62.4 lb/ft^3.

5.3 Previous Studies of Factors Affecting TDR

In the field, the salinity, the temperature, and the amount of suspended sediment in the channel flow will vary. Each of these parameters has an impact upon the speed of propagation of an EM wave through water. Stogryn (1971) developed several empirical equations that describe the impact of salinity and temperature on the apparent dielectric constant, K_a, which is defined as the square of the ratio of the speed of light in a

vacuum to the speed of the EM wave in a particular medium. As the TDR device uses a single EM wave, it is possible to use Stogryn's low frequency results for the static dielectric constant, leading to the Equations (5.5) through (5.8). These equations reveal that the apparent dielectric constant is a function of temperature, T and salt concentration, measured in normality units, N. The factors included in Equation (5.5) are the relationship of the static dielectric constant with temperature only and an empirical equation to account for the concentration of sodium chloride, $a(N)$. The salinity of the salt water, S can be related to the normality, as shown in Equation (5.8).

$$K_a(T,N) = K_a(T,0) \cdot a(N) \tag{5.5}$$

$$K_a(T,0) = 87.74 - 2.23(T-32) + 2.90\times10^{-4}(T-32)^2 + 2.42\times10^{-7}(T-32)^3 \tag{5.6}$$

$$a(N) = 1.000 + 0.2551N + 5.151\times10^{-2}N^2 - 6.889\times10^{-3}N^3 \tag{5.7}$$

$$N = S\left(1.07\times10^{-2} + 1.205\times10^{-5}S + 4.058\times10^{-9}S^2\right) \tag{5.8}$$

This set of equations can be used to assess the impact of the salinity and temperature upon the TDR measurement. To evaluate these effects, a scenario is constructed in which the salinity varied from 0 ppt to 17.5 ppt, a typical range found in channels near coastal waters (USGS, 2006a; USGS, 2006b). In this analysis, the temperature is also varied from 32 to 86°F. The relative error is computed from an apparent dielectric constant of 80.11, which corresponds to the value at 68°F and 0 ppt salinity. The results of this analysis are shown in Figure 5.5. In an environment where dielectric constant is greater than 80.11, the use of dielectric constant of 80.11 will result in longer distance that actually present. Thus, the calculated scour depth (using 80.11 as

dielectric constant) will be higher and relative error will be negative. As indicated, the impact of salinity and temperature on the dielectric constant is significant (up to 6% relative error).

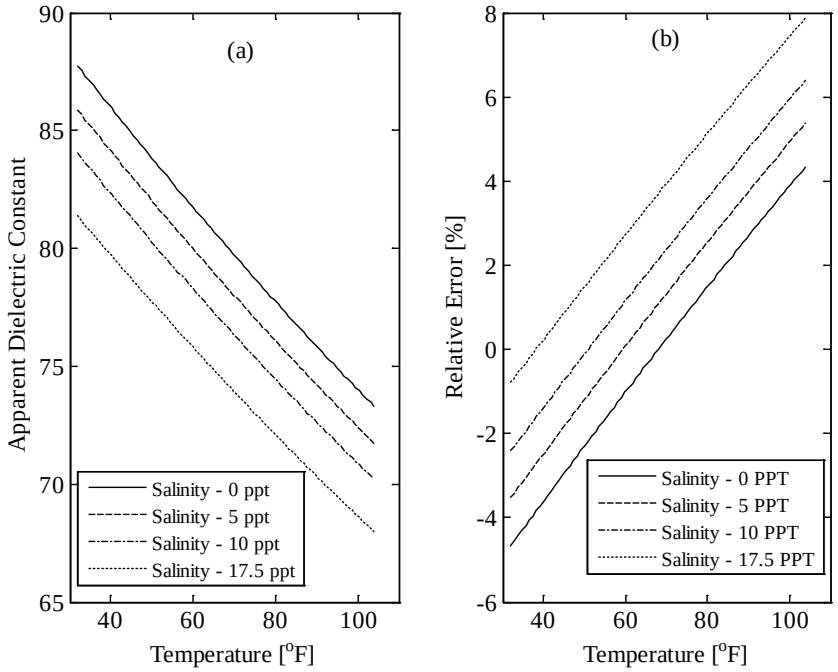

Figure 5.5: Effect of varying channel salinity levels and temperature on the dielectric constant and TDR measurements. (a) Dielectric constant, per Stogryn (1971). (b) Relative percentage error in TDR measurements.

It is also necessary to assess the impact of turbid water with various sediment concentrations upon the performance of a TDR system. Using the method developed by Yu and Yu (2011), it is possible to quantify the changes in the apparent dielectric constant for turbid water. Equations (5.9) and (5.10) are used to calculate the variations in the dielectric constant and relative errors in the resulting TDR measurements. Here, $K_{a,w}$

is the dielectric constant of water, $K_{a,s}$ is the dielectric constant of soil solid, $K_{a,bs}$ is the dielectric constant of saturated sediment, n is the porosity, ρ_{bulk} is the bulk density of the sediment, S is the specific gravity of the sediment and ρ_w is the density of water. Results are shown in Figure 5.6 (a, b) with respect to the dielectric constant of 80.11 as before. For typical channel sediment concentrations, 0.62 lb/ft^3 (Gray et al., 2003), the relative error is within 1%.

$$n\sqrt{K_{a,w}} + (1-n)\sqrt{K_{a,s}} = \sqrt{K_{a,bs}} \tag{5.9}$$

$$n = 1 - \frac{\rho_{\text{bulk}}}{S \times \rho_{\text{w}}} \tag{5.10}$$

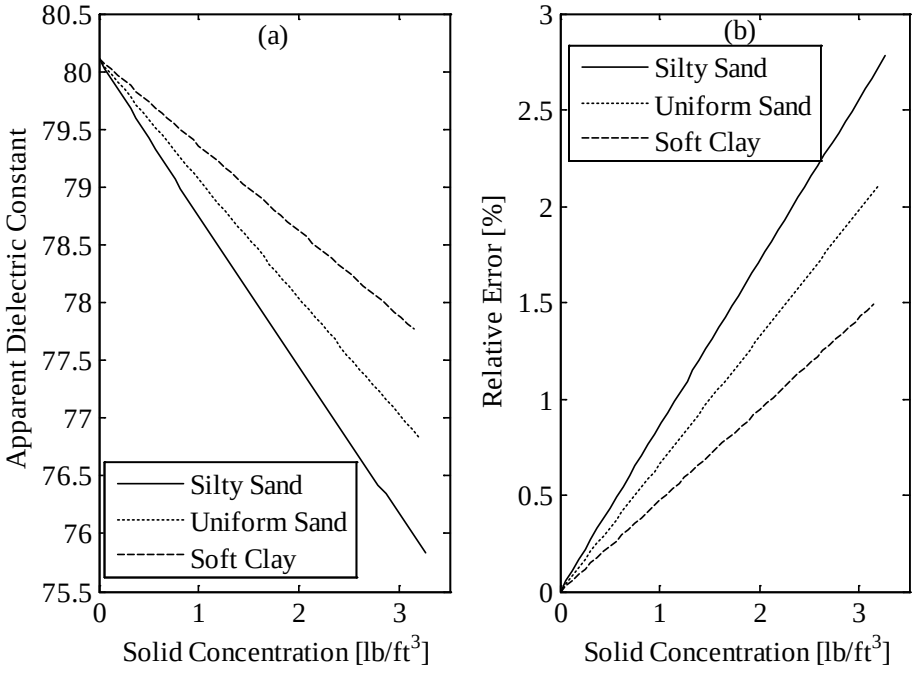

Figure 5.6: Effect of varying suspended sediment concentration on the dielectric constant and TDR measurements. (a) Impact on dielectric constant per Yu and Yu (2011). (b) Relative error in TDR measurements. Sediment types as shown in Das (1998).

5.4 Test Setup

To investigate the effects of channel conditions on sonar, TDR, and VTP instruments, several experiments were conducted in the Clemson Hydraulics Laboratory (CHL). The following section reviews the experimental setup for each of the devices.

5.4.1 Sonar Experimental Setup

The sonar system consisted of an Airmar SS510 transducer, with a sampling frequency of 234 KHz, an 8° beam width, and a tolerance of 0.1 ft. It was connected to a Campbell Scientific CR-800 data logger. Data were recorded on a work station via the Campbell Scientific PC200 software package. The temperature and salinity tests for sonar were conducted in a 12 inch diameter, 6 ft high test chamber. The sonar was mounted at the most 5 ft above the bed of the test chamber and was always submerged. This ensured that the beam did not intersect the side walls. During the test, the temperature was varied from 41 to 104°F and was measured with a Type K thermocouple. A uniform temperature distribution was maintained by complete mixing of the water. Salinity was varied from 0 to 35.5 PPT, measured with a Vee Gee SX-1 analog refractometer.

To investigate the effects of turbidity on the sonar device, experiments were conducted in stationary and dynamic configuration, including the effect of stratified turbidity. The static water turbidity tests were conducted in a 6 ft diameter plastic tank with water depths up to 4.1 ft and turbidity values from 39 to 520 NTU. The dynamic turbidity tests were conducted in the CHL flume with a depth of 1.84 ft, for flow velocity ranging from 0.13 to 0.4 ft/s. The stratified turbidity flow tests were also conducted in the same flume for channel flow depths ranging from 1.80 to 2.0 ft, and velocity from 0.18 to

0.4 ft/s. The stratified turbidity layer consisted of two distinct regions. The bottom layer (up to 2 inches) had a concentration of 300 to 900 NTU and the flow above had a concentration of 7 to 17 NTU, as shown in Figure 5.7. For each of these tests, the turbidity was measured with a Global Water WQ 730 turbidity sensor connected to the GL 500U data logger.

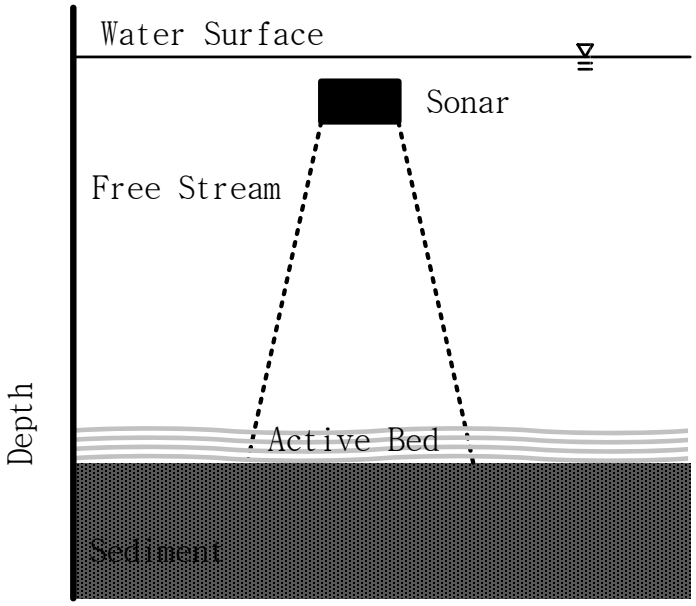

Figure 5.7: Schematic of the turbidity stratification test.

In addition to temperature, salinity, and turbidity effects on sonar, the effect of the bed contour was also investigated. Two series of tests were conducted with cones of 6 inches and 9 inches in diameter, which were placed underneath the sonar. To create a planar reflecting surface, the cone was partially filled with sand as shown in Figure 5.8.

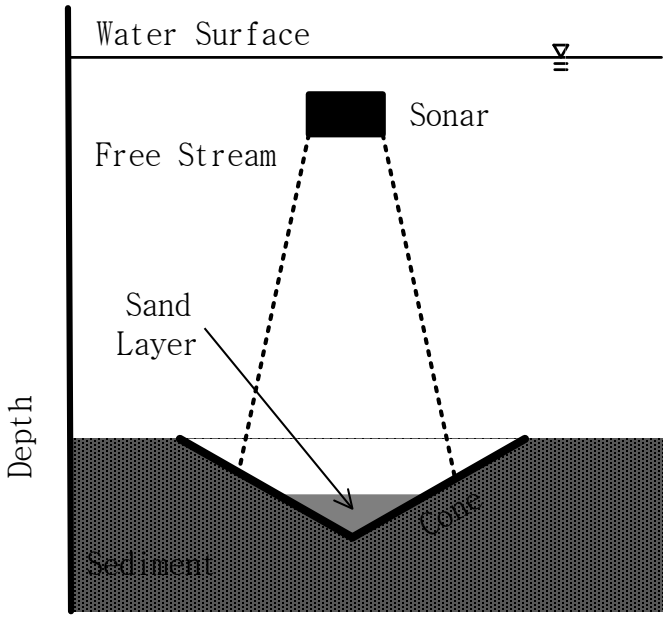

Figure 5.8: Schematic of the scour hole/beam ratio tests.

5.4.2 TDR Experimental Setup

The TDR system used to investigate the effects of temperature, salinity, and turbidity on measurements consisted of a probe similar to that used by Yankielun and Zabilansky (1999), as shown in Figure 5.9. The waveform was generated by the TDR 100, from Campbell Scientific, and was recorded on a work station running the Campbell Scientific PC TDR software. The tests were conducted in a 1.97 ft diameter barrel, with the lower portion of the TDR probe located in sand, with an AFS (American Foundry Society) grain fineness number of 16, and the upper portion completely submerged in the water, as shown in Figure 5.9. The temperature tests were conducted at two water depths, 2.41 and 1.82 ft, with temperatures ranging from 44.6 to 104°F. During the salinity tests, the concentration was varied from 0 to 0.75 ppt, in 0.25 ppt increments, for a water depth

of 2.26 ft. The effect of turbidity on the TDR readings was evaluated in 1.72 ft deep water with sediment concentration ranging from 100 NTU to 500 NTU.

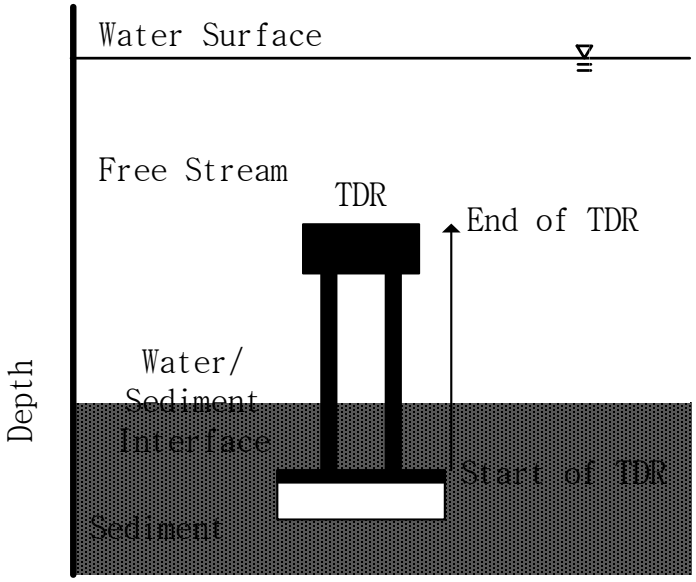

Figure 5.9: Schematic of the test using TDR.

5.4.3 VTP Experimental Setup

To evaluate the VTP performance, experiments were conducted to investigate the effect of suspended sediment and misalignment between the main flow direction and the VTP axis. Additionally, the effect of bed material on the sensors located below the channel bed level was evaluated. Lastly, the flow rate was varied in order to determine the minimum flow rate required for a distinct difference between the VTPs located in the bed and in the channel flow.

The VTP configuration consisted of sensors with a 0.787 inch radius neoprene disk, instrumented with a PCB 325A24 accelerometer of 5.5×10^{-4} slugs, with a

sensitivity of 3.05 mV per ft/s^2. The VTPs were installed along the length of an aluminum support pipe of 4 inches in diameter, spaced at intervals of 4 inches (center to center), as shown in Figure 5.10. The measured results were recorded with a Bruel and Kjaer Lan XI 3050A-060 data acquisition system, operating at a sampling frequency of 25.6 KHz. A convergence study revealed that a 4 minute measurement period was sufficient and yielded results that were within 1% of the measurements taken over longer periods of time. For each condition, the measurements were repeated three times.

Figure 5.10: VTP setup as installed in CHL flume for channel effects study.

For the turbidity tests, the VTP was evaluated in the CHL flume with 2 ft flow depth and velocities from 0.23 to 0.40 ft/s. The turbidity was varied from 0 to 900 NTU in 300 NTU increments. For the flow misalignment tests, the flow velocity was held constant at 0.90 ft/s while the flow angle was varied from 0 to 90° in increments of 15°. To evaluate the impact of the velocity and to find the minimum velocity required to

distinguish between the VTPs in the sediment and in the flow, tests were conducted with velocity ranging from 0.5 to 0.98 ft/s.

5.5 Sonar: Temperature Effects

The temperature tests on the sonar device were conducted at depths of 3, 4.1, and 5.1 ft. The results show that the percent relative error increases as the temperature increases from a reference temperature of 68°F. As shown in Figure 5.11, Figure 5.12, and Figure 5.13, the percent relative errors in the sonar readings range from -3.30% to 3.30%,

-4.97% to 1.77% and -5.98% to 2.00%, for 3, 4.1, and 5.1 ft deep water, respectively. The dash lines in the figures show the resolution of the instrument (±0.1 ft). The relative errors increase with increase in water depth.

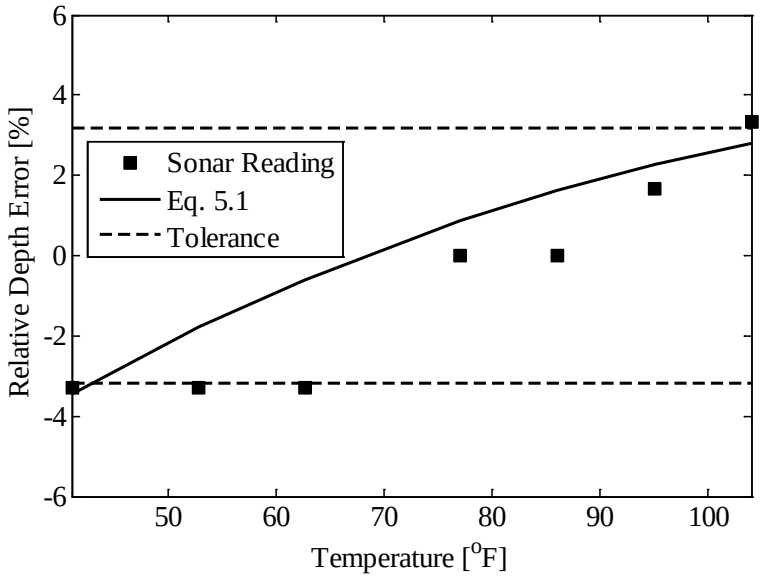

Figure 5.11: Variation in relative error of sonar measurements with temperature for water depth of 3 ft.

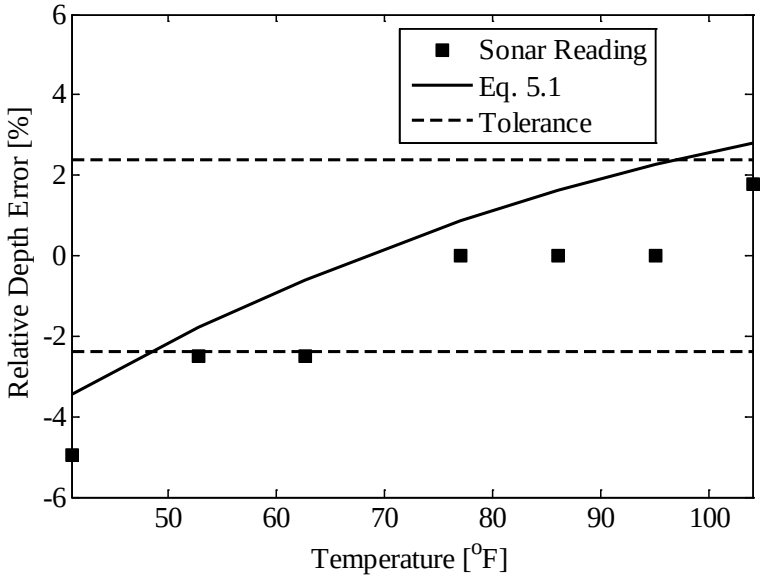

Figure 5.12: Variation in relative error of sonar measurements with temperature for a water depth of 4.1 ft.

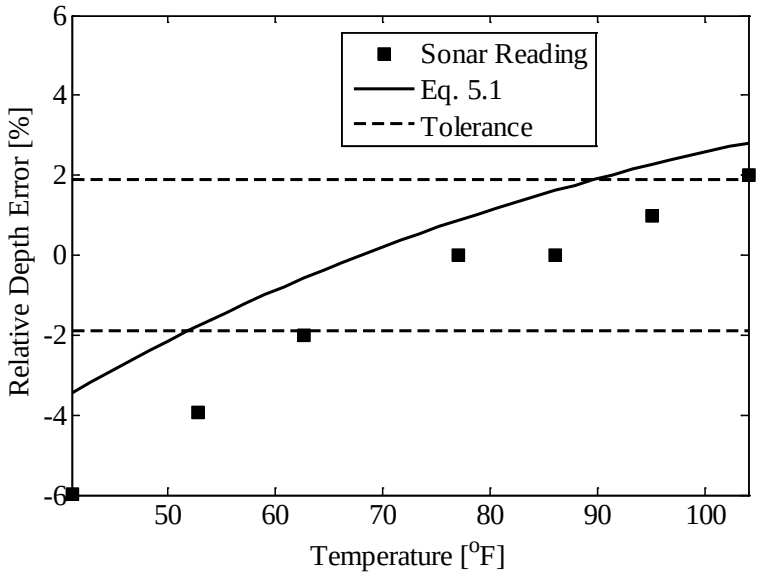

Figure 5.13: Variation in relative error of sonar measurements with temperature for a water depth of 5.1 ft.

The results suggest that as the channel temperature changes seasonally, the distance to the bed, and any scour depth will artificially vary, simply due to changes in the flow temperature. The lower temperatures (less than 68°F) have greater impact on the relative error compared to the higher temperatures. As shown in Figure 5.13, the experimental results follow the same trend as the Mackenzie's model predictions (Figure 5.1). The deviation between the two results may be accounted for by the resolution of the sonar transducer ($\pm$ 0.1ft).

Thus, to account for temperature changes, the water temperature should be measured along with the sonar signal. It must be noted that as the depth of the channel increases, the sonar readings are affected to a greater degree by the temperature since the error is proportional to the distance traveled by the acoustic pulse.

5.6 Sonar: Salinity Effects

The salinity tests on sonar were conducted for two water depths (3.8 and 4.3 ft). The relative errors, as shown in Table 5-1, range from 3.51 to 3.81% (relative to zero salinity). These values are in line with the errors predicted in section 5.2 with the Mackenzie's model. The model reveals that for the same range of salinity, the error could reach up to 3.18 %.

Table 5-1: Range of percent relative error in water depth, and comparison with theoretical model.

Water depth, [ft]	Range of salinity, [ppt]	Measured relative error [%]	Relative error [%] (Mackenzie,s model)
3.8	0 to 35.5	0 to 3.51	0 to 3.18
4.3	0 to 35.5	0 to 3.81	0 to 3.18

The results in Table 5-1 suggest that if the sonar transducer is located within 4.3 ft of the bed, the influence of salinity on the measurements is likely to be minor. However, as the distance of the sonar from the bed increases, the error will increase. This presents a tradeoff, however, between the ease of maintenance in the field, which is complicated by installations close to the bed, and measurement error.

5.7 Sonar: Turbidity Effects

Turbid waters are commonly encountered in natural rivers. To evaluate the impact of suspended particles on the sonar readings, three cases were considered. In the first case, the sonar was tested in still turbid water in a tank; in the second case, the sonar was tested in flowing turbid water in a flume; lastly, the effect of turbidity stratification on sonar accuracy was evaluated. For the still turbidity test, the water depth was varied from 3.1 to 4.2 ft and the concentration was varied from 39 to 525 NTU. Table 5-2 shows that still turbidity has a negligible effect on the accuracy of the sonar in locating the bed.

Table 5-2: Range of percent relative error in water depth for various turbidities.

Water depth, [ft]	Relative error [%]	Tolerance limit [%]	Range of turbidity [NTU]
3.1	0 to 3.3	-3.2 to 3.2	39 to 525
3.70	0 to 2.8	-2.73 to 2.73	39 to 525
4.2	0	-2.4 to 2.4	39 to 525

The combined effects of suspended particles and channel flow were evaluated in a flume for a water depth of 1.84 ft, and the results are shown in Figure 5.14 and Figure 5.15. In Figure 5.14, the relative percent errors for a 30 second sample mean are plotted for various average velocities and turbidity levels in the channel. Figure 5.14 shows that as the velocity increases, the absolute relative error increases for all turbidities. Additionally, it appears that for a given velocity the level of turbidity has little effect on the measured error. In addition, the range of error for different turbidities is about the same for the velocity range considered in this test. For example, for a turbidity of 402 NTU, the relative error varies from -6.12 to 0.41%, while for 220 NTU the relative error varies from -6.82 to -2.1%.

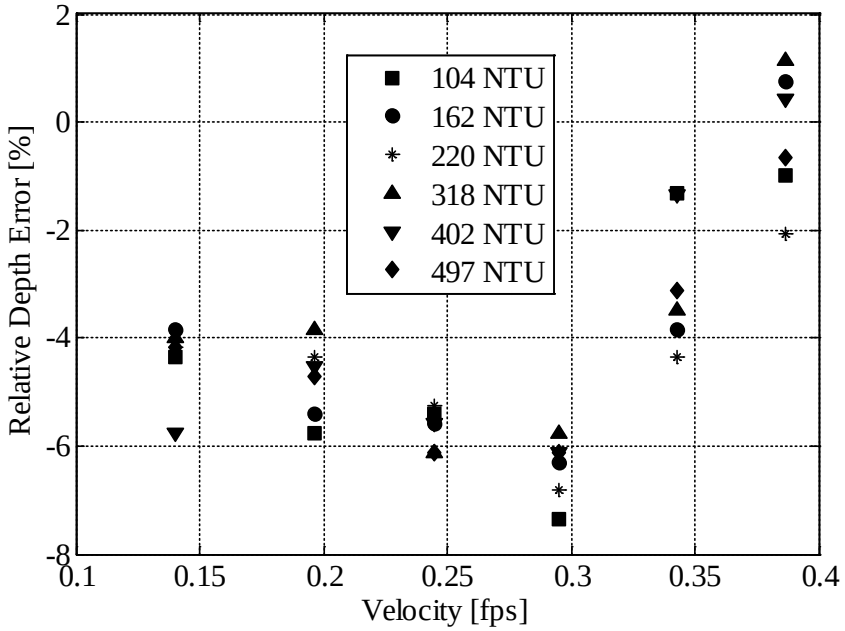

Figure 5.14: Relative error in the sonar reading for various turbidity concentrations and velocities.

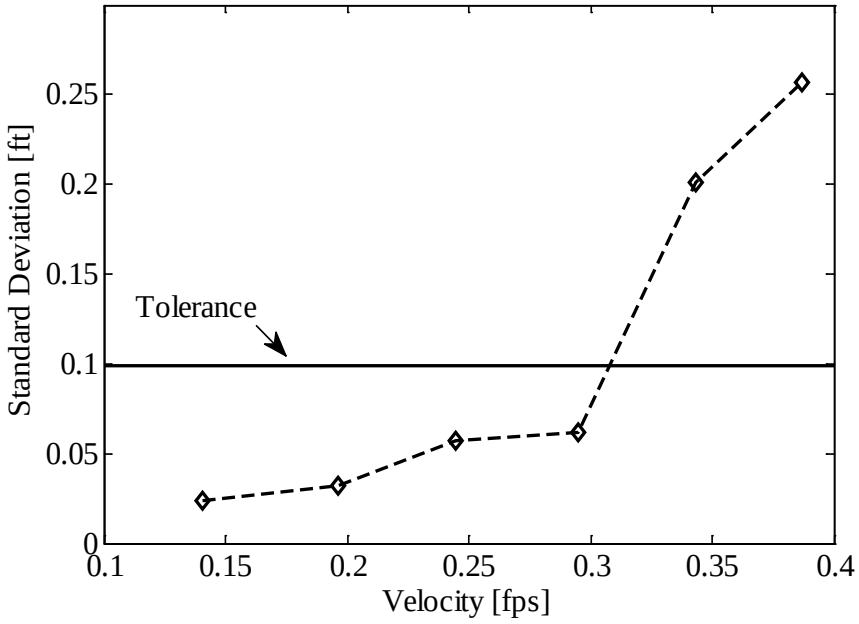

Figure 5.15: Average standard deviation of sonar readings based on Figure 5.14.

In Figure 5.14, it should be noted that for velocities greater than 0.3 ft/s, there is a step change in the relative percent error. The source of this divergence is revealed in Figure 5.15, where the standard deviation in the 30 seconds time histories increases sharply to a level above the sonar device tolerance. This indicates that for the two highest velocities, the sonar device is not able to locate the bed. Thus, the combined results in Figure 5.14 and Figure 5.15 reveal that as the velocity of a turbid flow increases beyond 0.3 ft/s, the sonar can no longer obtain a stable recording. The inability to locate the bed is attributed to the higher velocity with which the suspended sediment particles are moving and may be attributed to Doppler shift.

The results in Figure 5.14 and Figure 5.15 indicate that when the standard deviation of the sonar time history exceeds the device tolerance, the average value is inaccurate and scour readings should be independently verified with another device. Also, the results suggest that for sites with higher sediment loads during peak flow conditions (which is normally the condition), sonar reading may be questionable.

In the final turbidity test configuration, the effects of stratified concentrations and flow velocities were considered. The velocity ranged from 0.13 to 0.4 ft/s, the stratified layer thickness varied from 0.80 to 1.98 inch, and the concentration in the stratified layer was between 300 and 900 NTU. The flow depths during the tests ranged from 1.80 ft to 2.0 ft. The results of these experiments reveal that for low velocities and increasing layer thickness, the relative error can be as high as 17.5%. For stratified layers of smaller thickness, this error drops down to 2%, which is of the order of the thickness of the layer.

As has been demonstrated earlier in the report, it is important to investigate the standard deviation of the measured signal in the stratified turbidity test. As shown in Figure 5.16, the standard deviation of the 30 second time histories is above the sonar device tolerance limit for all concentrations. This indicates that the sonar device is unable to determine the bed level. These results suggest that the stratification effects are not well described by considering density alone. Therefore, other effects, such as increased scattering or attenuation by the sediment particles, must also be considered.

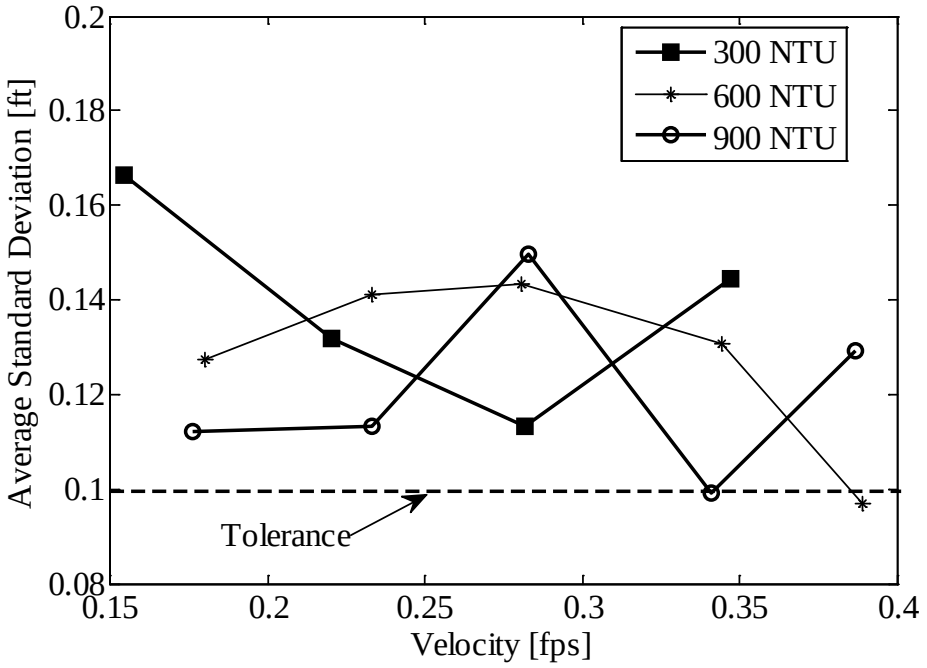

Figure 5.16: Standard deviation of sonar for various stratification concentration and velocities.

In summary, sonar is affected by moving turbid water. For a uniform turbidity and for velocities higher than 0.3 ft/s, the sonar device cannot locate the bed level. For

stratified flow, this effect occurs even for low velocities. As such, the findings suggest that sonar devices should not be used independently in highly turbid zones. It is important to monitor the standard deviation of the recorded signal to confirm that the sonar readings are reliable.

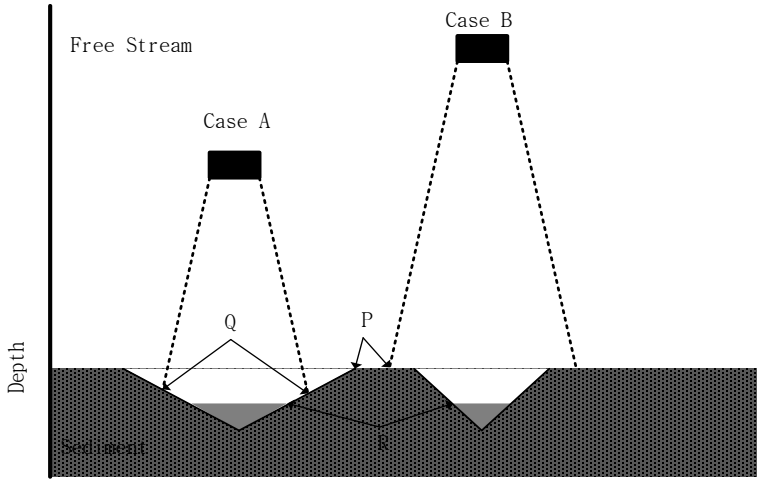

Figure 5.17: Sonar beam to scour hole size experimental setup.

5.8 Sonar: Topography and Beam Width Effect

Naturally developed scour holes have uneven surfaces. Therefore, it is important to determine the location in the bed topography that is registered by a sonar pulse. Two cases were considered, one where the sonar beam fell entirely within the scour hole, Case A, and the other where the sonar beam completely surrounded the scour hole, Case B, as shown in Figure 5.17. In Case A, the sonar beam reflected along the surfaces from point Q (the minimum water depth) to point R (the maximum water depth). In Case B, however, the minimum depth corresponded to the unscoured bed level, located by point

P. These two conditions were tested in the lab. The results are shown in Table 5-3 and Table 5-4.

Table 5-3: Experimental results for case A.

Maximum Water Depth, R [ft]	Minimum Water Depth, Q [ft]	Average of R and Q [ft]	Actual Sonar Reading [ft]
2.80	2.51	2.66	2.5 ± 0.1
2.49	2.24	2.36	2.2 ± 0.1
2.10	1.88	1.98	1.80 ± 0.1

Table 5-4: Experimental results for case B.

Maximum Water Depth , R [ft]	Minimum Water Depth, P [ft]	Actual Sonar Reading [ft]
3.66	3.40	3.3 ± 0.1
2.77	2.50	2.60 ± 0.1
2.45	2.20	2.10 ± 0.1
1.78	1.50	1.60 ± 0.1
1.50	1.26	1.30 ± 0.1

The results show that the measured sonar readings are within the device tolerance limit of point Q for Case A, as shown in Table 5-3. Similarly, for Case B the measured sonar results correspond to point P, as shown in Table 5-4. From these two results, it can be concluded that the sonar measurements correspond to the minimum depth encountered by the beam, which does not correspond to the point of maximum scour. Therefore, in the field if the beam is contained within the hole, sonar is expected to underestimate the scour depth. Alternatively, if the sonar transducer is located far from the bed, due to

installation or maintenance concerns, and if the beam diameter is larger than the scour hole, the presence of scour may be completely ignored.

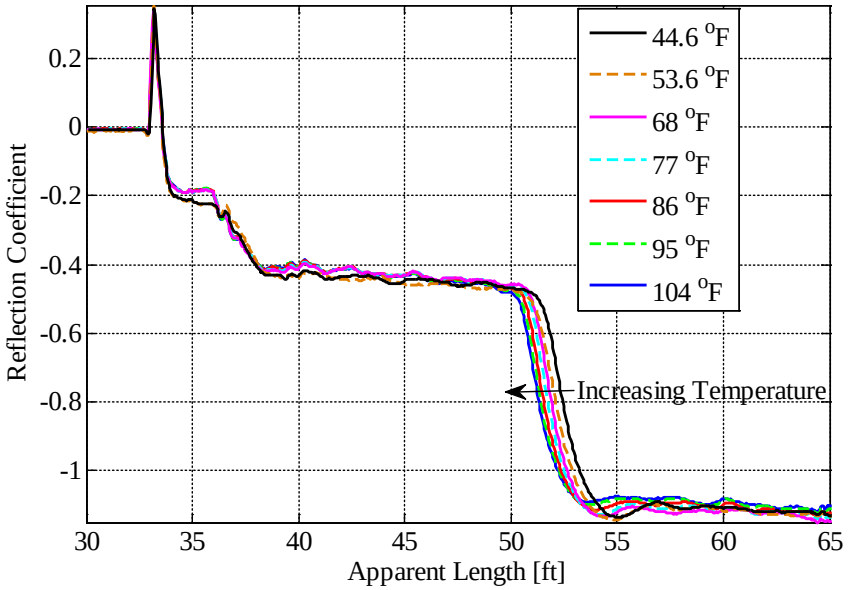

Figure 5.18: TDR waveform in various water temperatures for water depth 1.92 ft.

5.9 TDR: Temperature Effects

As discussed previously, the dielectric constant is a function of temperature and decreases with increasing water temperature (Stogryn, 1971). Results for the TDR probe under various water temperatures are shown in Figure 5.18. The curves shown are the reflected waveforms generated by the TDR and are analyzed using the method outlined by Yankeilun and Zabilansky (1999). At the start of the waveform, a sharp reflection occurs indicating the start of the probe. This is then followed by a 'plateau A' at a reflection coefficient of -0.2, corresponding to the depth of sediment. This plateau is

followed by another step that leads to 'plateau B' with a reflection coefficient of approximately -0.4, indicating the presence of water column. Finally, there is a terminal step change indicating the end of the probe. Figure 5.18 indicates that as the temperature increases, the waveform shifts such that it gives a decreasing trend of apparent length.

Temperature tests on TDR system were performed for two water depths (2.41 ft and 1.92 ft). Water depths extracted from TDR waveform were then converted to percent relative error, relative to the dielectric constant at 68°F. Figure 5.19 and Figure 5.20 show the percent relative errors in the measured results, for the water depth of 2.41 and 1.92 ft, respectively, along with the predictions from Stogryn's (1971) model.

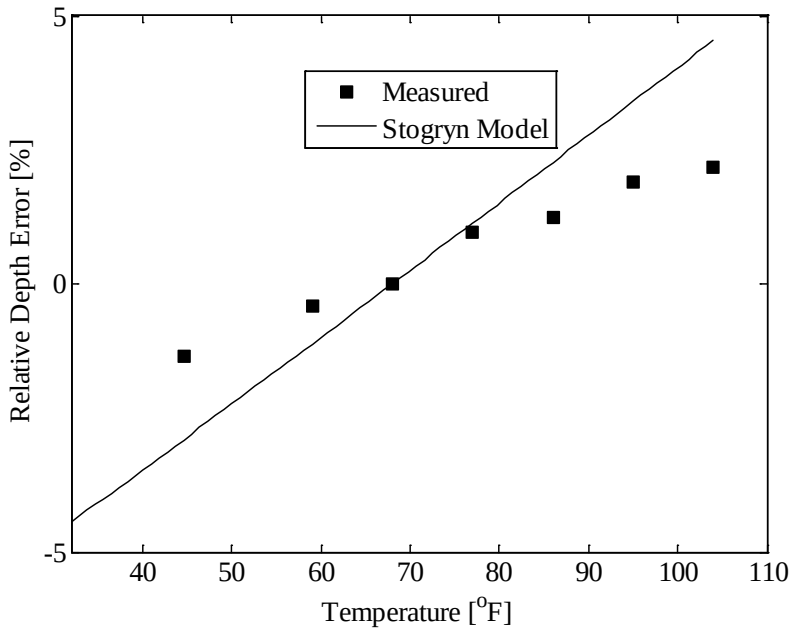

Figure 5.19: Relative error in the TDR readings for various temperatures and water depth of 2.41 ft.

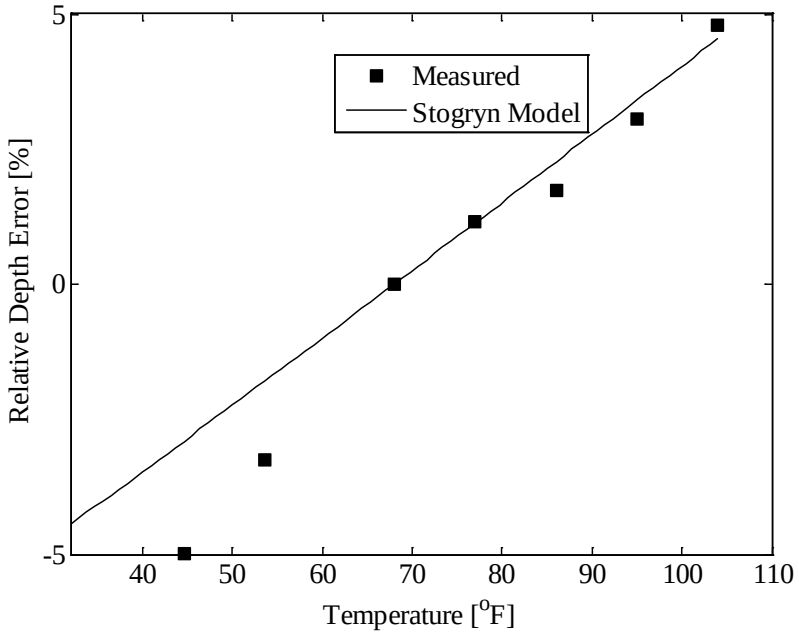

Figure 5.20: Relative error in the TDR readings for various temperatures and water depth of 1.92 ft.

In general, the figures indicate that lower water depths are measured by the TDR as temperature increases above 68 °F and that higher depths are measured as the temperature decreases below 68 °F. The percent relative error in water depth ranges from -1.36% to 2.18% and -4.98% to 4.78% for 2.41 ft and 1.92 ft of water depths, respectively. The measured values determined by the TDR method are affected by the change in the water temperature. Practically, this suggests that in the winter season, the TDR might overestimate the scour depth while in summer TDR might underestimate the scour depth. The temperature dependency of the measurements can be accounted for by measuring temperature as part of the scour monitoring system.

5.10 TDR: Salinity Effects

The salinity of the flow can also affect the accuracy of a TDR system as indicated by Stogryn (1971). Thus, TDR was tested under various salinity conditions and the resulting waveforms are shown in Figure 5.21. The TDR waveform, particularly the reflection at the end of the probe, becomes increasingly hard to distinguish as the salinity increases. Above 0.5 ppt, the reflection at the end of the probe is indistinguishable. This degradation in performance can be attributed to the decay of the EM wave into the surrounding medium, which becomes more conductive as the salinity increases. Therefore, deploying a TDR device in a saline environment or at sites that could become brackish (greater than 0.5 PPT) can lead to inconclusive results, due to the loss in the distinct features of the waveform necessary to determine the scour depth.

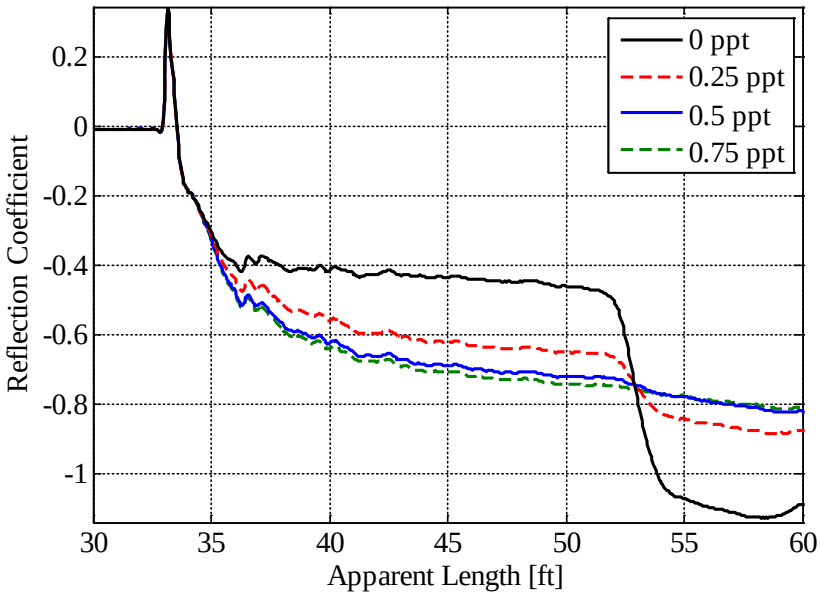

Figure 5.21: Sensitivity of TDR waveform to salinity.

5.11 TDR: Turbidity Effects

The results obtained for the turbidity tests conducted on the TDR system for a water depth of 1.7 ft are shown in Figure 5.22. The effect of turbidity on TDR measurements is determined by calculating the percent relative error in water depth predictions. For turbidities up to 500 NTU, the TDR system is insensitive to the presence of suspended sediments. The results shown in Figure 5.22 imply that the TDR system can be efficiently operated in highly turbid zones (maximum error up to 5%).

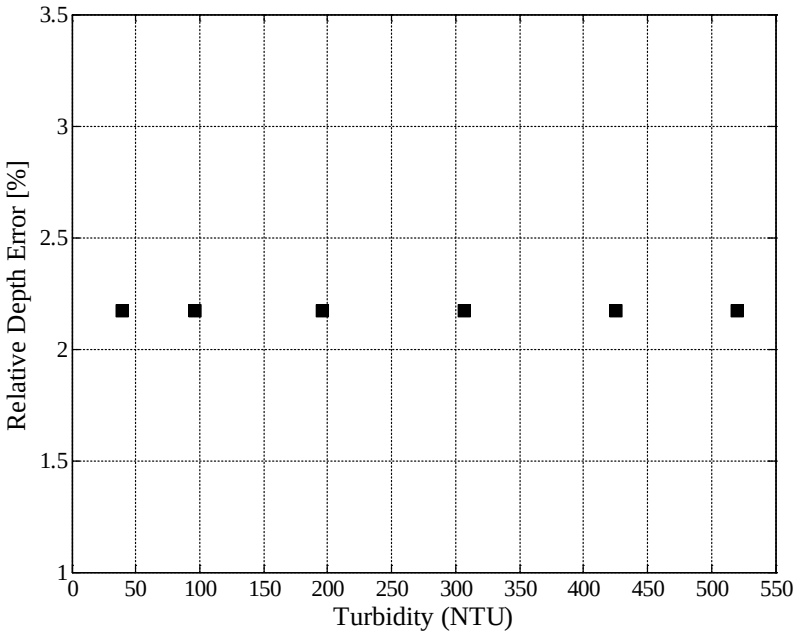

Figure 5.22: Effect of turbidity on TDR.

5.12 VTP: Turbidity

VTP based method has the potential to be affected by turbidity in the flow, as well as any misalignment between the flow direction and the VTP axis. Also, in order to

fully evaluate the VTP method, it is necessary to consider the effect of different sediment types on the measured energy content in the bed. Lastly, the minimum channel velocity needed to achieve a measurable difference between those VTPs located in the flow and those in the sediment should be determined. The results from the tests conducted to evaluate the performance of the VTP device under these conditions are discussed below.

The impact of dynamic turbidity on the VTP's turbulent energy content is shown in Figure 5.23 for turbidities ranging from 0 to 900 NTU and flow velocities from 0.23 to 0.40 ft/s. The results indicate that the registered energy content increases slightly with turbidity. The increase in the VTP energy content with flow velocity is expected since $\sqrt{\overline{u'^2}}$ increases with the mean flow velocity.

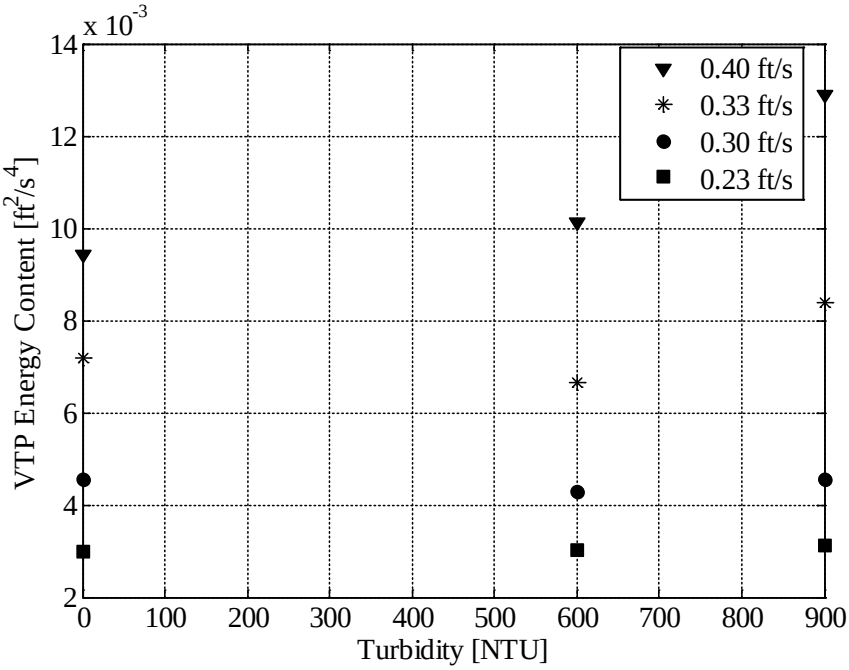

Figure 5.23: VTP energy content for various turbidity levels and channel flow velocities.

The results shown in Figure 5.23 indicate that the VTP's energy content response increases in the presence of turbidity in the flow, and thus the device can be deployed without the need to monitor the turbidity level in the channel. The energy content of the VTP buried in the bed was not affected by turbidity and flow velocity.

5.13 VTP: Flow Misalignment

During high flow events, it is possible that the main flow direction can shift from the normal flow direction. Therefore, it is necessary to understand how a VTP performs as the flow direction relative to the probe changes. Figure 5.24 reveals the VTP energy content for three sensors located at different depths within the channel. VTP #6 is located in the sediment and therefore the response should not be a function of the flow angle. This is revealed in the results shown in Figure 5.24. VTP #5 is located within a scour hole, and the results reveal that the response for VTP #5 is insensitive to flow angle. This is attributed to the fact that in the scour hole, the flow is separated. Thus the sensor in a scour hole is subject to velocity fluctuations from the separated flow instead of the turbulent free stream velocity fluctuations. The recorded energy content for VTP #5 is an order of magnitude higher than the VTP in the bed (VTP #6), indicating that the method can be used to determine the water/sediment interface. The energy content recorded by VTP #4 is sensitive to the flow angle, dropping from 0.17 ft^2/s^4 at 15° to 0.08 ft^2/s^4 at 90°. This is expected as the magnitude of the turbulent fluctuations normal to the VTP surface diminishes with increasing misalignment. It is also important to note that the results are still an order of magnitude higher than the VTP located below the bed. The ratio between VTP #4 and VTP #6 at 90° is approximately 75. This suggests that the

method can still be used in highly misaligned flows. For the higher flow angles, the separated flow around the probe itself maintains the energy content at a level much higher than the energy content in the sediment.

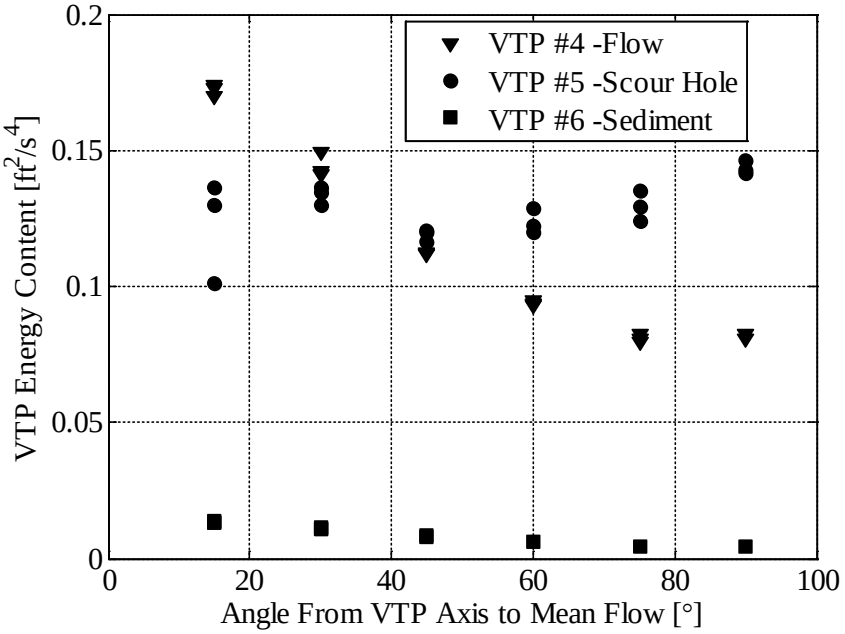

Figure 5.24: VTP energy content as a function of the flow misalignment.

5.14 VTP: Flow Velocity

Chapter 3 revealed that the minimum energy content in the flow should be at least one order of magnitude greater than in the sediment. To investigate the impact of velocity, the energy content of two VTPs was recorded for depth averaged channel velocities ranging from 0.48 to 1.0 ft/s. The results are shown in Figure 5.25. The results reveal that the energy content of the VTP in the sediment decreases with decreasing velocity, to a minimum of 4.3×10^{-4} ft^2/s^4. For the VTP in the flow, the energy content

decreases to 0.022 ft^2/s^4. This value is low compared to the energy content at higher velocities; however, it is still greater than the energy content of the VTP below the bed by a factor of 50. Thus, the VTP method is still able to determine the water/sediment interface even at low velocities. Based upon these results, it can be concluded that the VTP method will function for a depth averaged channel velocity of at least 0.48 ft/s.

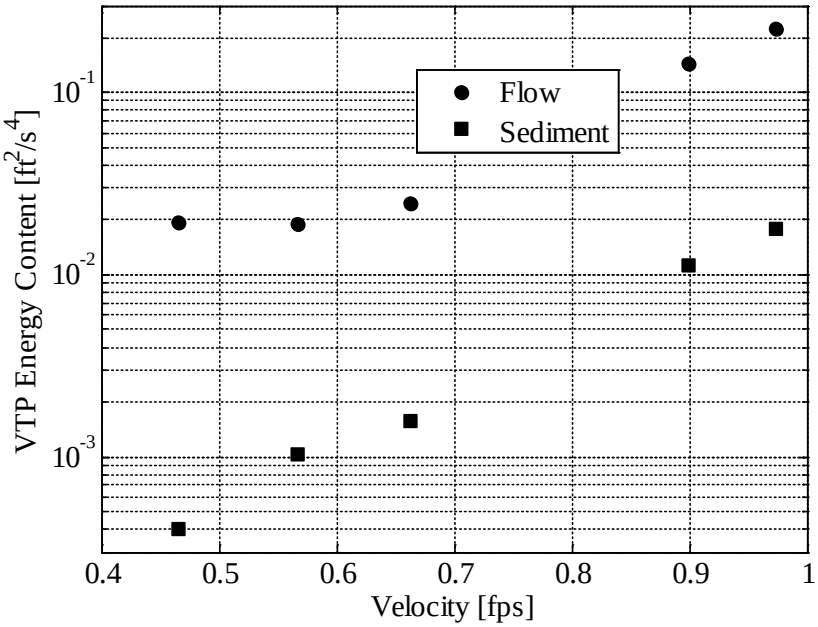

Figure 5.25: Variation of VTP energy content with channel velocity.

5.15 VTP: Bed Sediment Type

Lastly, when considering the response of the VTP method, it is also important to investigate the impact of varying sediment types on the energy content of the VTP below the bed. The potential effect of varying sediment types was investigated by conducting three experiments in two different quartz sands and in clay sediment. The results of these

experiments are shown in Figure 5.26. The results indicate that the sediment has no measureable impact upon the measured energy content for the VTPs located in the channel bed. Therefore, the device can reliably be deployed without being significantly affected by the nature of the sediment type in the channel.

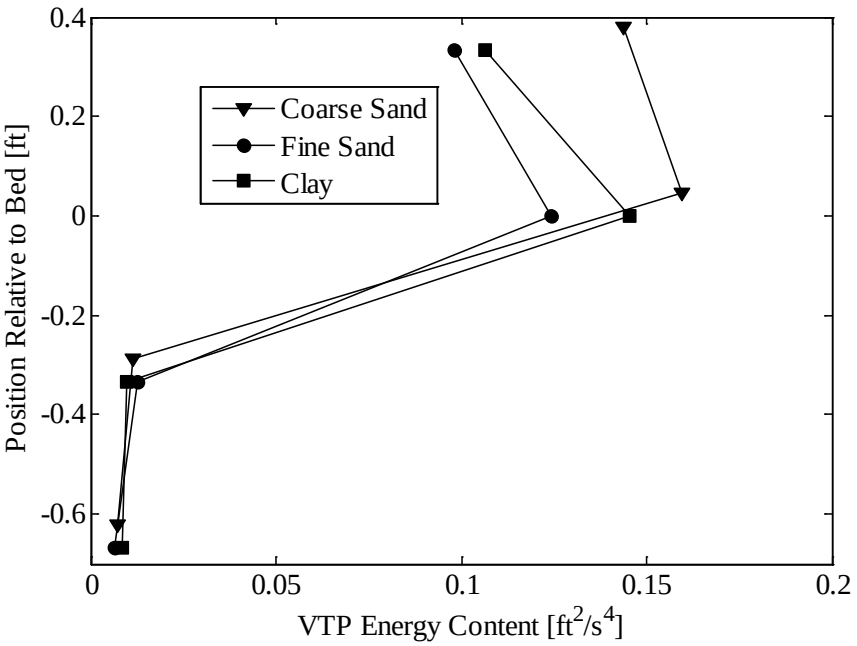

Figure 5.26: Variation of VTP energy content for various bed sediment types.

5.16 Summary

Given the fact that the changing environmental conditions in natural channels are inevitable, it is necessary to understand how these parameters can affect scour monitoring systems. A series of experiments were conducted on two common scour measurement devices, namely a sonar transducer and a time-domain reflectometer probe. In addition,

the performance of the VTP device which exploits the flow turbulence in the channel was also evaluated.

From the series of experiments conducted it can be concluded that for the sonar device, changes in temperature can result in relative errors up to 6% in channel depth. The relative error is a function of the height of sonar above the bed, and as this height increases the relative error will increase. This can be accounted for in the field by measuring the temperature and accounting for the change in the speed of sound. Salinity can lead to relative errors of up to 3% for depths up to 4.2 ft, which is within the tolerance of the device tested.

The concentration of suspended particles does not affect the sonar results in still water. For dynamic turbidity, uniform as well as stratified, the relative error in bed level measurements can be significant. The results indicate that measuring the standard deviation of the recorded signal may be important to ascertain the viability of the measurements. Lastly, the beam width with respect to scour size and the height at which the sonar is located above the bed may significantly affect the accuracy of the scour depth measurements. It is determined that for variable bed topography, the sonar records the shallowest depth.

For TDR, the channel temperature in the range of 44.6 to 104°F results in relative error of the order of 5%. The effect is small; however, it can be mitigated by monitoring the channel temperature. For salinities greater than 0.5 ppt, the distinct features needed in the TDR waveform to determine the length of the water and sediment depth around the probe are lost. Thus, it is necessary to avoid the installation of TDR in brackish

conditions. Turbidity in the channel flow had no effect on the TDR measurements and can be used for monitoring scour in highly turbid zones.

The performance of a VTP was evaluated under turbid flow conditions and varying flow angles. The results indicate that there is no significant change in the energy content recorded by the VTP based method for varying turbidities. Thus, it is possible to use the method in turbid zones. The energy content recorded by the VTP located in the flow decreases with increasing misalignment between the probe and the main flow direction. However, even at 90° misalignment, the energy content of the VTP in the flow is an order of magnitude greater than the VTP in the sediment. Thus, it can record the location of the water/sediment interface accurately even in highly misaligned flows. In addition, the VTP method is not affected by the bed sediment type and performs in coarse and fine sand beds as well as in clay beds. For depth-averaged channel velocities as low as 0.48 ft/s, the device can be used to determine bed location.

Based upon the results presented for the various methods it is possible to select a scour monitoring instrument for a given site. The selected instrument should be insensitive to the anticipated channel conditions, thus resulting in more robust field measurements.

CHAPTER 6

FIELD INSTALLATION AND DATA COLLECTION

6.1 Introduction

Following the performance evaluation of each instrument through laboratory experimental investigations, the adaptability and performance of sonar, TDR, and VTP devices are evaluated under field conditions in the final phase of this project. Field performance evaluation of the instruments is necessary to make a conclusive evaluation prior to large scale deployment of the instruments. To this end, the instruments have been installed on the two SCDOT recommended field sites for monitoring scour depth. This chapter presents the data collected from the field performance evaluation, discusses the relative comparison of performances, and provides recommendations for the field deployment of the instruments.

6.2 Selection Criteria of Field Sites

Occurrence and frequency of scour was one of the primary considerations in the selection of the field sites. Presence of real time stream flow measurement stations (installed by the USGS) at the sites was another consideration in the selection process. The flow measurement stations would provide real time data of the water surface elevation/discharge at the site, which is an indicator for flood and scour/refill events. The water surface elevation data are essential for the mapping of scour events recorded by the instruments to the flood events. Proximity of the field sites to the Clemson University campus was also a key factor as periodic maintenance prior to sustainable deployment

was envisioned. Other factors included, for example, ease of installation, vulnerability to damage, and water depth at the pier under normal flow conditions. Based on the preceding considerations, the bridge site on Highway 76 over Eighteen Mile Creek, Pendleton, SC, the bridge site on the Enoree River near Woodruff, SC, and the bridge site over Black Creek in Florence, SC on S-26 were selected as primary sites for installation. The installation at the third site had to be abandoned due to closure of the bridge for repairs. In addition, the loss of equipment at the first site during the flood events in July 2013 resulted in budget constraints. Accordingly, the deployment of instruments at the third site was eliminated.

6.3 Field Site 1

The first field site is located on Highway 76 over Eighteen Mile Creek, Pendleton, SC (USGS Station No. 02186702 and Latitude 34°38'42" N, Longitude 82°48'02" W). This location was chosen for its close proximity to Clemson University (about 2.6 miles) and its vulnerability to scour. The TDR and VTP devices were installed at this site. A high pressure pump was used to create two jets. These jets were used to lower the instrument into the bed.

TDR and VTP were first installed in November 2012 at this field site to measure the scour depth at the pier. For the next several months, data collection software, raw data processing programs, and data transfer system were developed and optimized. This experience proved helpful for efficient installation of equipment and management of data at other sites. After installation, several unusual flood events occurred at this site, causing damage and delays. During a flood event on January 18, 2013, large debris dislodged the

instruments from their location. Instruments were reinstalled in March 2013. However, again during a major flood event on July 13, 2013, debris dislodged and damaged both instruments. In addition, water elevation during the flood reached and damaged the data acquisition units that were installed just below the bridge deck. This particular flood event resulted in damage and loss of equipment worth several thousands of dollars. A new VTP device was manufactured, and new instruments were purchased. Scour monitoring systems were reinstalled at the site in February 2014 and since then both TDR and VTP have been measuring scour depths. Although the two flood events posed setbacks for the field evaluation study, sufficient amounts of data were collected to support a comparative performance evaluation of the instruments. The installed instruments, field site, and equipment are shown in Figures 6.1-6.5.

Figure 6.1: Satellite view of Field Site 1 (Source: Google Earth).

Figure 6.2: Solar panel and data acquisition system at Field Site 1.

Figure 6.3: SCDOT crew assisting in running the cable at Field Site 1.

Figure 6.4: Instruments mounted on the face of the footing pad at the pier.

Figure 6.5: TDR (on the right) and VTP (on the left) at Field Site 1.

6.4 Field Site 2

The second field site is located on Harris Bridge Road, Spartanburg County, SC (USGS Station No. 02160390; Latitude 34°41'00" N, Longitude 82°02'24" W). TDR and sonar were installed at this site to measure scour depths in January 2014. The TDR was installed as described for the Field Site 1. At this site, the sonar was attached to a rod that was clamped to the pier. Devices started to record scour depths in February 2014. Instruments were installed at the pier located in the middle of the river and immediately behind the upstream pier in order to avoid damage due to debris (Figure 6.9). The field site and installed equipment are shown in Figures 6.6-6.9.

Figure 6.6: TDR and sonar at Field Site 2 (Source: Google Earth).

Figure 6.7: SCDOT crew assisting in running the cable at Field Site 2.

Figure 6.8: Installed TDR (on the right) and sonar (on the left) at Field Site 2.

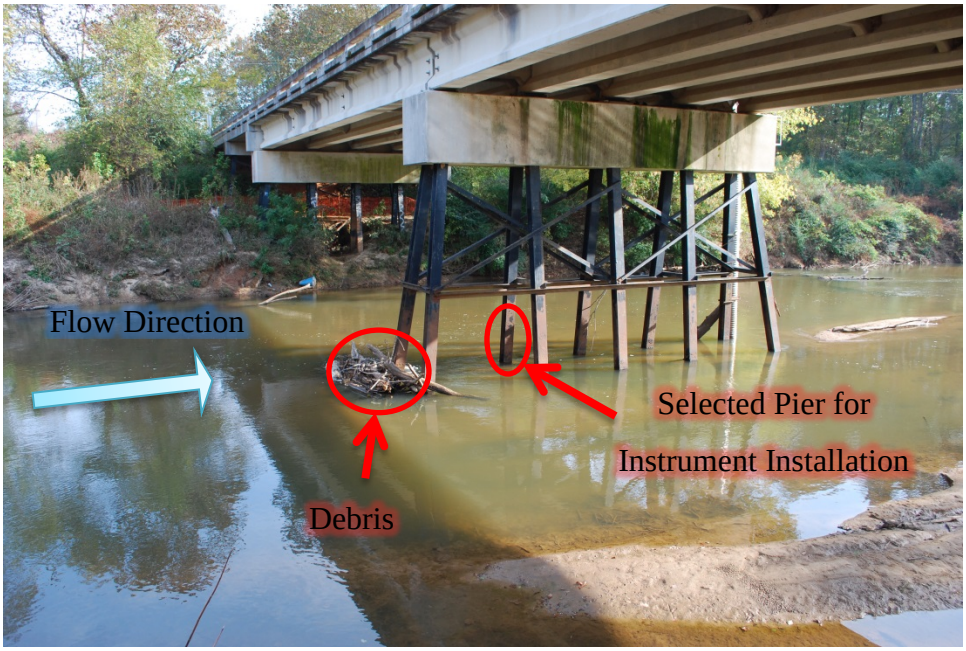

Figure 6.9: Bank view showing the pier located in the middle of the river.

This field site is prone to debris accumulation at the upstream pier. Large piles of debris have altered the natural flow of the river near the bridge, creating stagnation zones and turbulence zones (Figure 6.9). SCDOT cleared the debris twice in 2013. Although most of the debris was cleared, one log that was wedged in the bed at the upstream pier could not be removed. For this reason, instruments were installed on the pier behind the upstream pier as shown in Figure 6.9.

6.5 Installation and Data Collection Procedure

The systems at both field sites are powered by solar energy. Solar panels transmit energy to the batteries during daylight hours. The energy stored in the batteries is utilized for powering up the data loggers and instruments at prescribed times for recording,

processing, and storing data. The batteries also provide power to cellular modems for data transmission.

At Field Site 1, TDR and VTP are installed to monitor scour and compare the performances of the instruments. The TDR probe is connected to an Electromagnetic pulse emitter TDR 100 (from Campbell Scientific), and a CR 800 data logger (from Campbell Scientific). Raw data from the TDR is collected every 30 minutes via Loggernet Software (from Campbell Scientific). This raw data is then processed to obtain the bed elevation. The bed elevation data are transmitted via the internet to Clemson University.

With the VTP device, Bruel & Kaer Pulse Lan-XI unit (B&K module) is used to power up accelerometers attached to the VTPs. The accelerometers measure the vibrations of the VTPs, which are recorded by the B&K module. The B&K module transmits raw data to the laptop at the site via Netgear Ethernet hub. Raw data is processed by software developed during this project to obtain the energy content of the accelerometers and subsequently to obtain bed elevation. All the processed data is transferred from the field to Clemson University via the internet.

At Field Site 2, sonar and TDR are installed to compare the relative performance of these devices. The setup for the TDR is the same as described for the Field Site 1. The only difference is that the data logger used at this site is CR 1000 (an updated version), instead of CR 800. The sonar is also connected to the CR 1000 data logger, which makes the system power efficient. The CR 1000 records the data from both devices every 30 minutes and transfers the data to Clemson University every hour.

6.6 Bed Elevation Results from Field Site 1

In this section, bed elevations data obtained from TDR and VTP devices are presented in chronological sequence. Bed elevations from each instrument correspond to the distance from a common datum, which in this case is the top of the concrete pad at the pier and is denoted by zero elevation in the plots. In addition, water surface elevations based on the USGS gauge station record have also been plotted to check the consistency and the sensitivity of the instruments in recording the scour resulting from flood events. The bed elevation data at this site have been collected since March 2014. Except during maintenance and troubleshooting periods, the data collection is continuous.

6.6.1 Bed Elevation History Using TDR

The bed elevations measured using the TDR measurements are shown in Figures 6.10–6.16. Each figure shows the record for one month. The water surface records at the site are also shown in these figures. The scour events follow the flood episodes at the site.

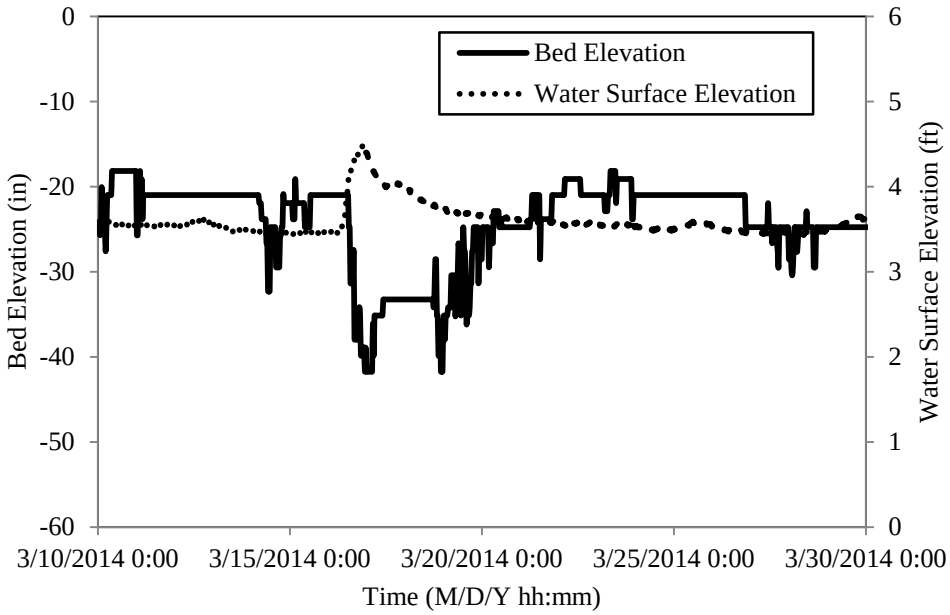

Figure 6.10: Bed elevation from TDR in March 2014.

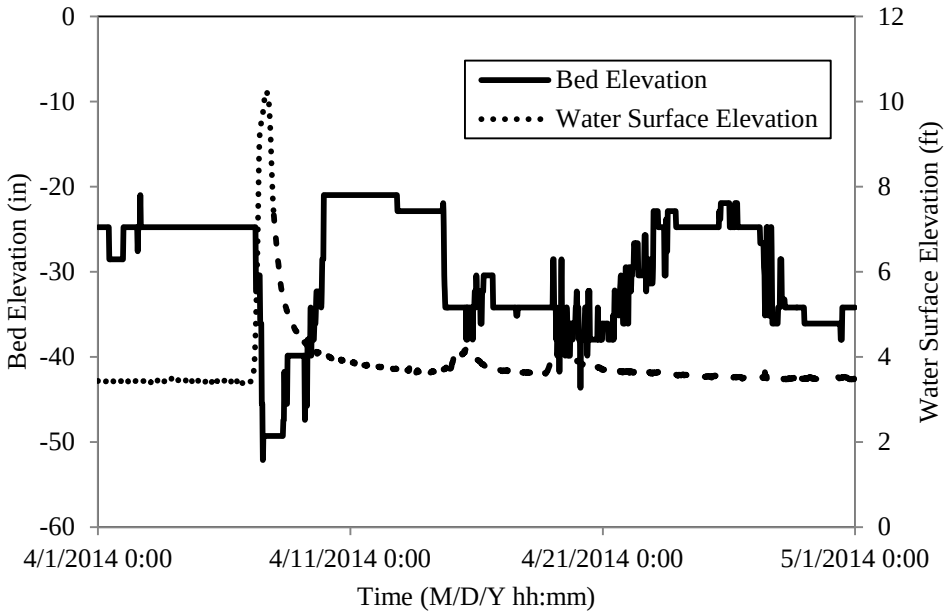

Figure 6.11: Bed elevation from TDR in April 2014.

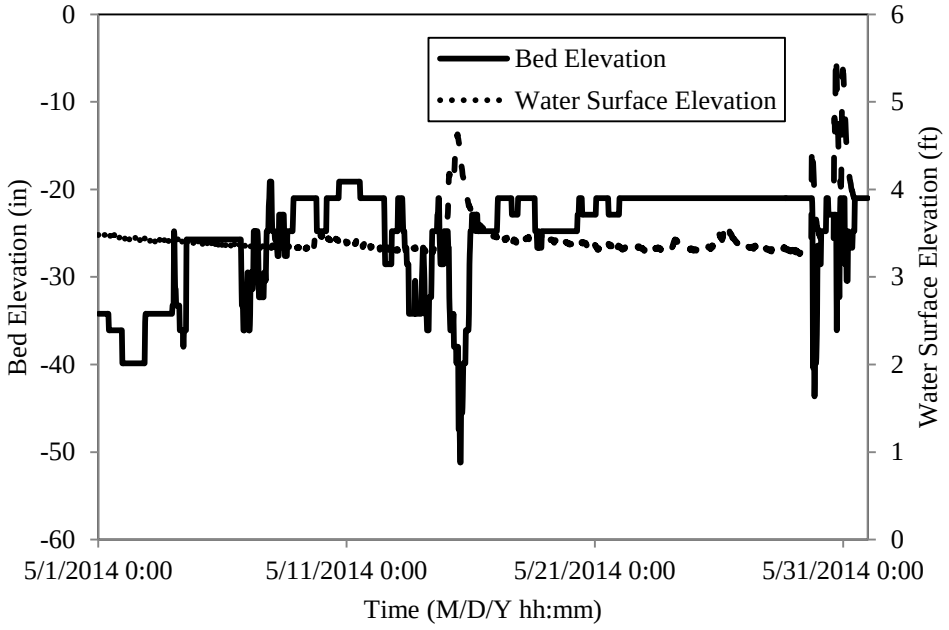

Figure 6.12: Bed elevation from TDR in May 2014.

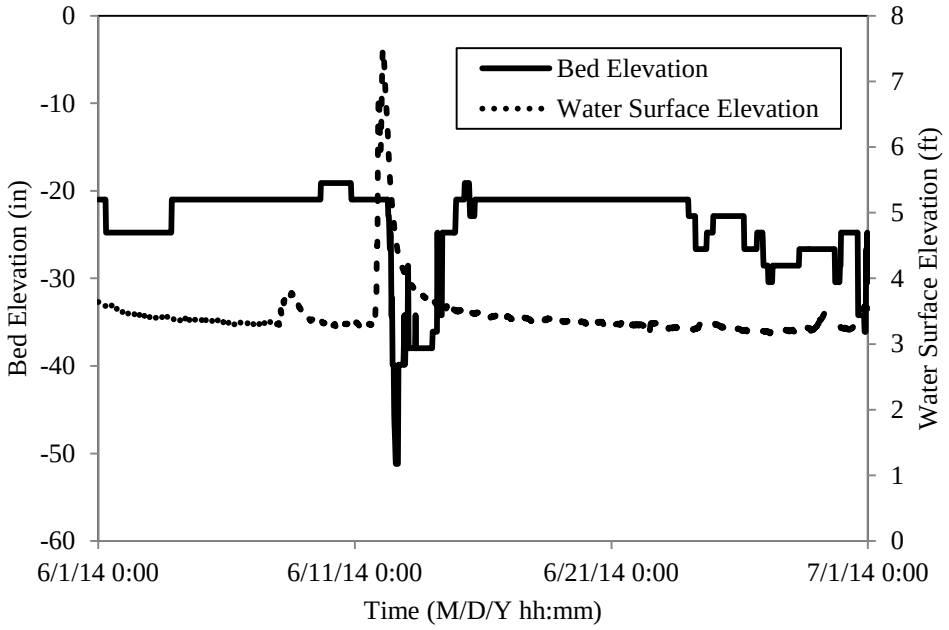

Figure 6.13: Bed elevation from TDR in June 2014.

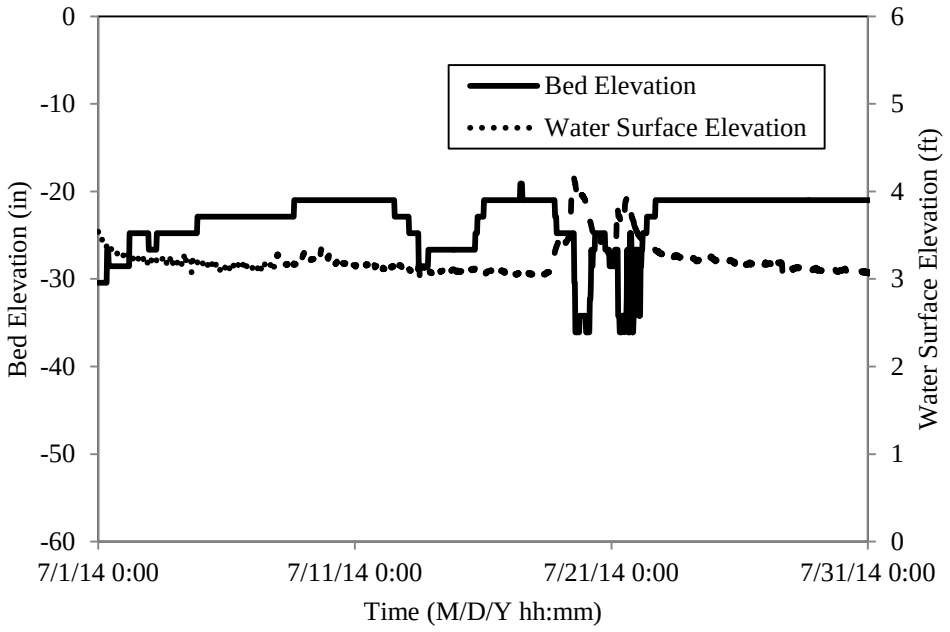

Figure 6.14: Bed elevation from TDR in July 2014.

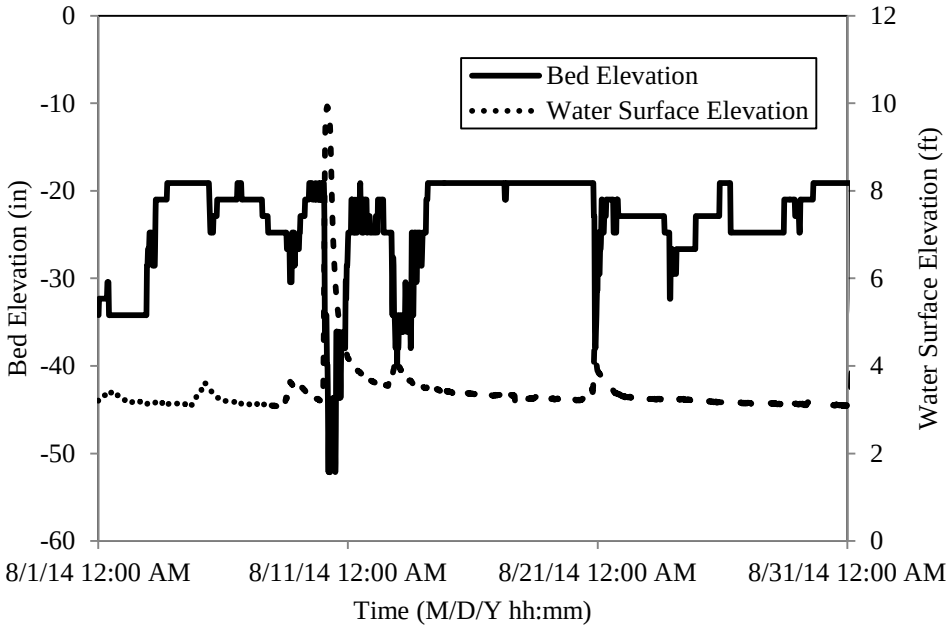

Figure 6.15: Bed elevation from TDR in August 2014.

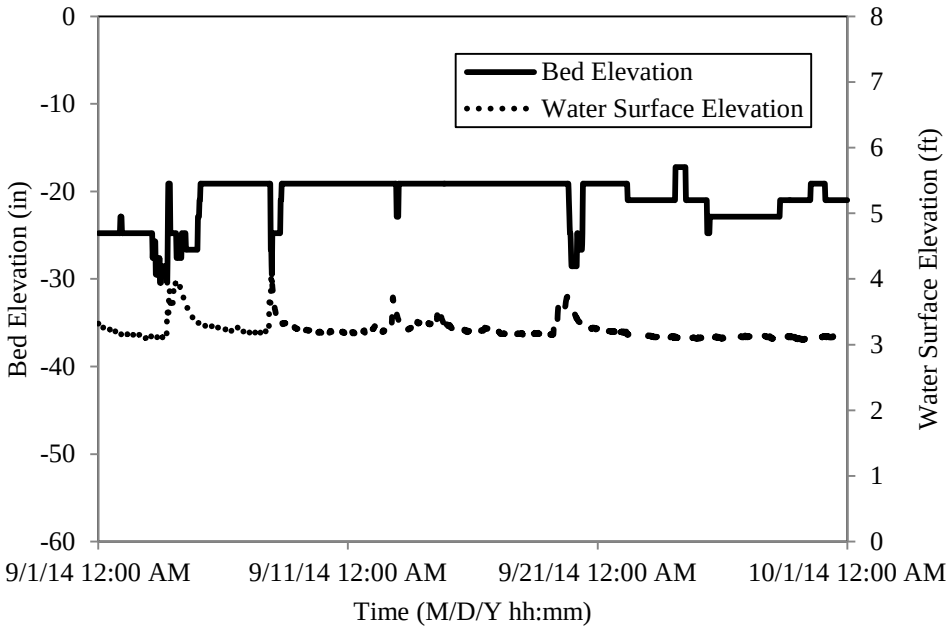

Figure 6.16: Bed elevation from TDR in September 2014.

6.6.2 Bed Elevation History Using VTP

The bed elevations recorded using the VTP device at this site are shown in Figures 6.17–6.23 for the seven month period beginning with March. The minimum bed elevation that can be measured with the VTP device is -45 inches, which corresponds to the length of the device.

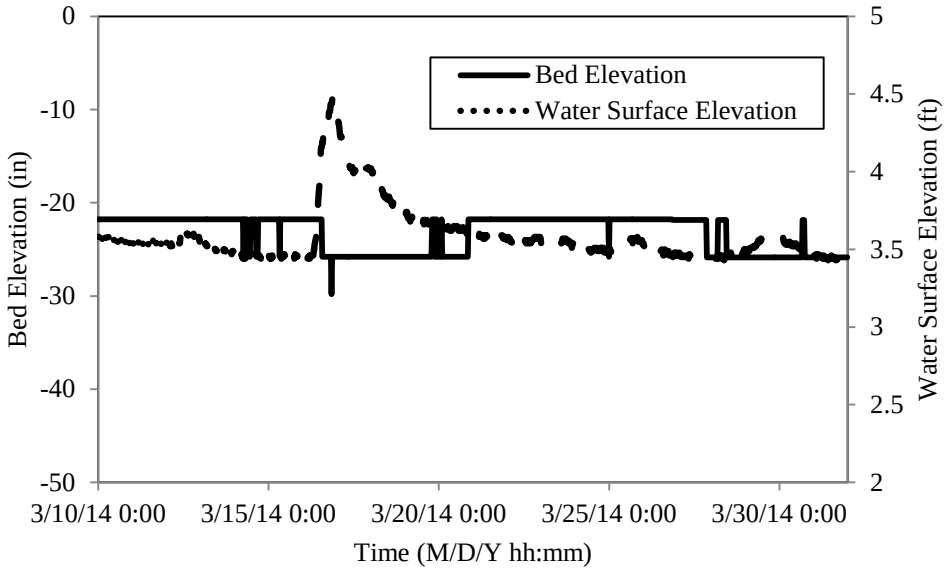

Figure 6.17: Bed elevation from VTP in March 2014.

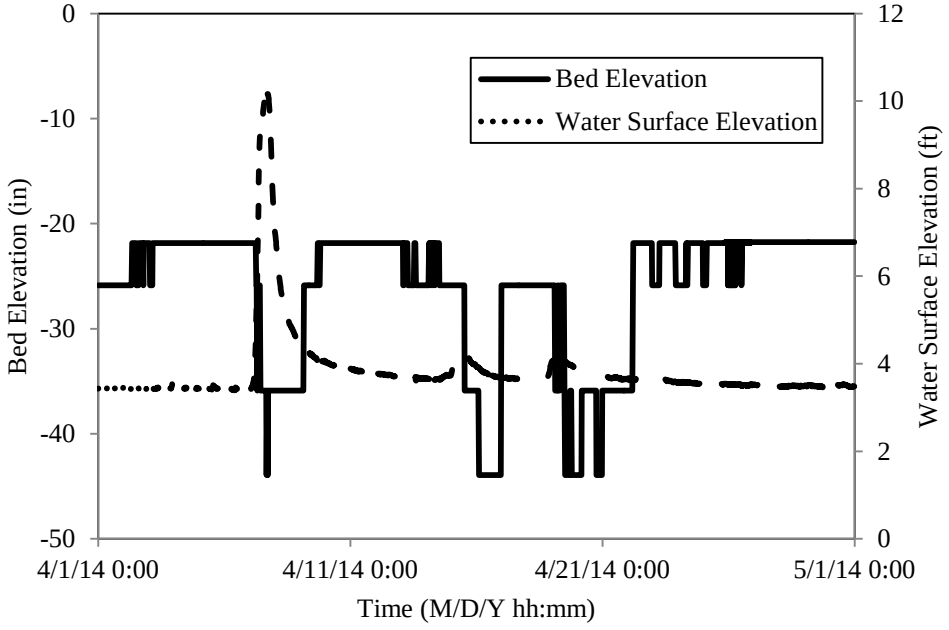

Figure 6.18: Bed elevation from VTP in April 2014.

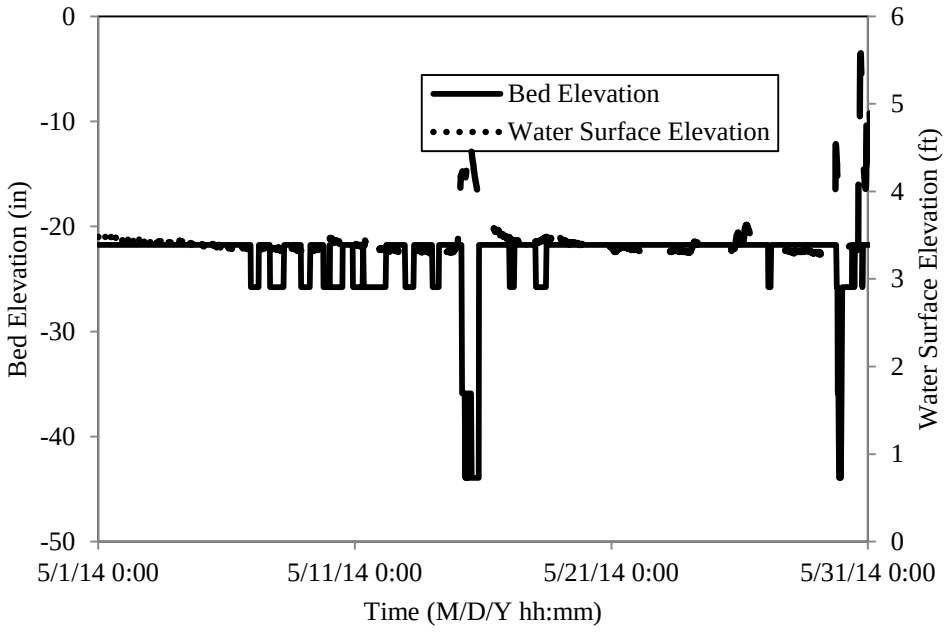

Figure 6.19: Bed elevation from VTP in May 2014.

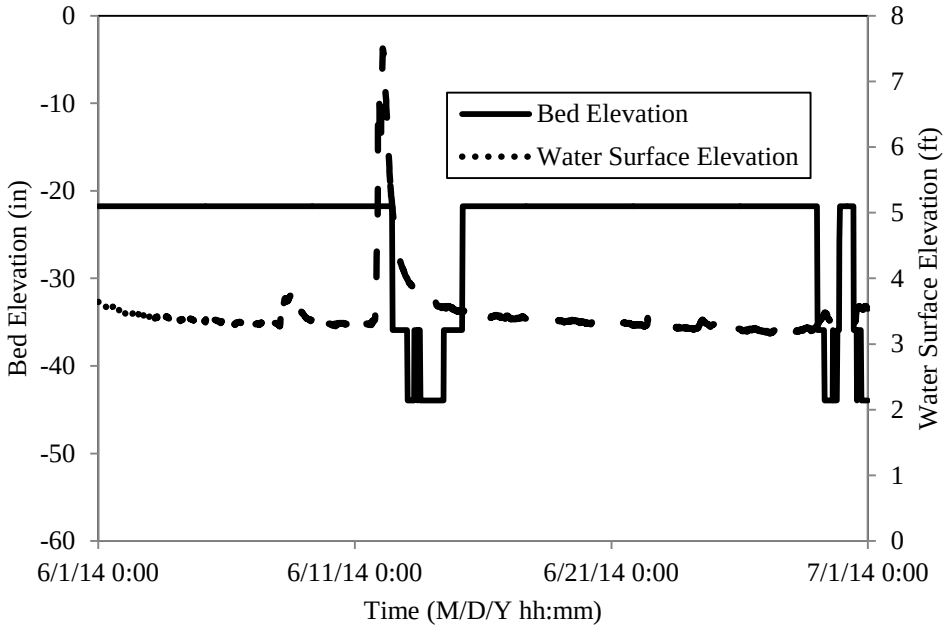

Figure 6.20: Bed elevation from VTP in June 2014.

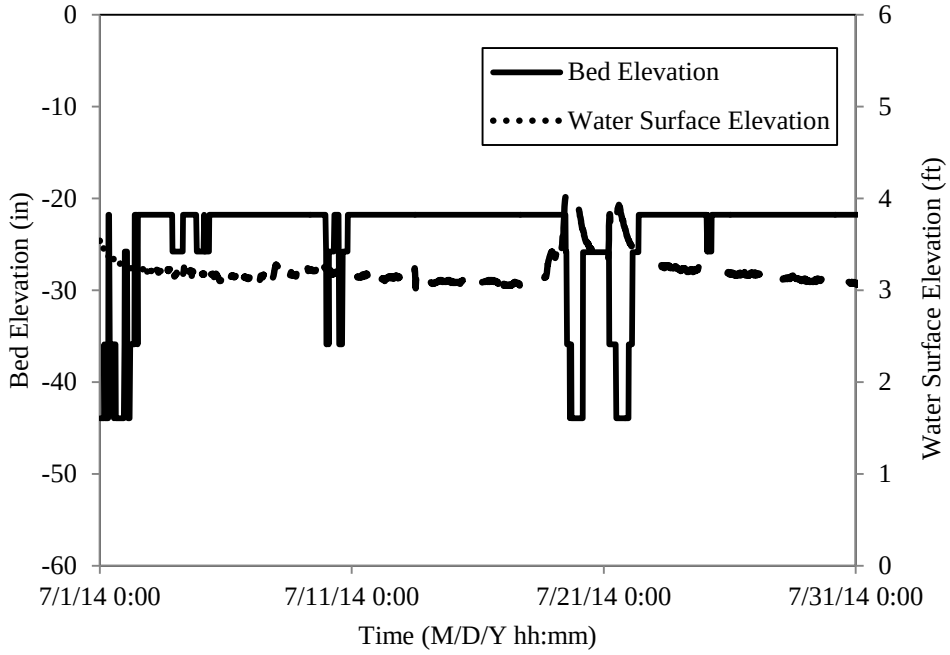

Figure 6.21: Bed elevation from VTP in July 2014.

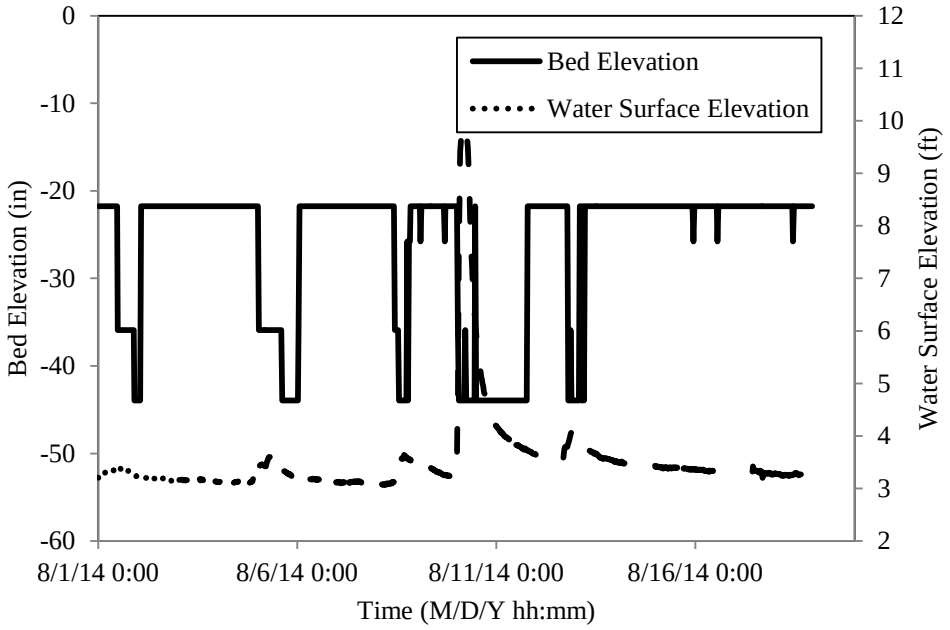

Figure 6.22: Bed elevation from VTP in August 2014.

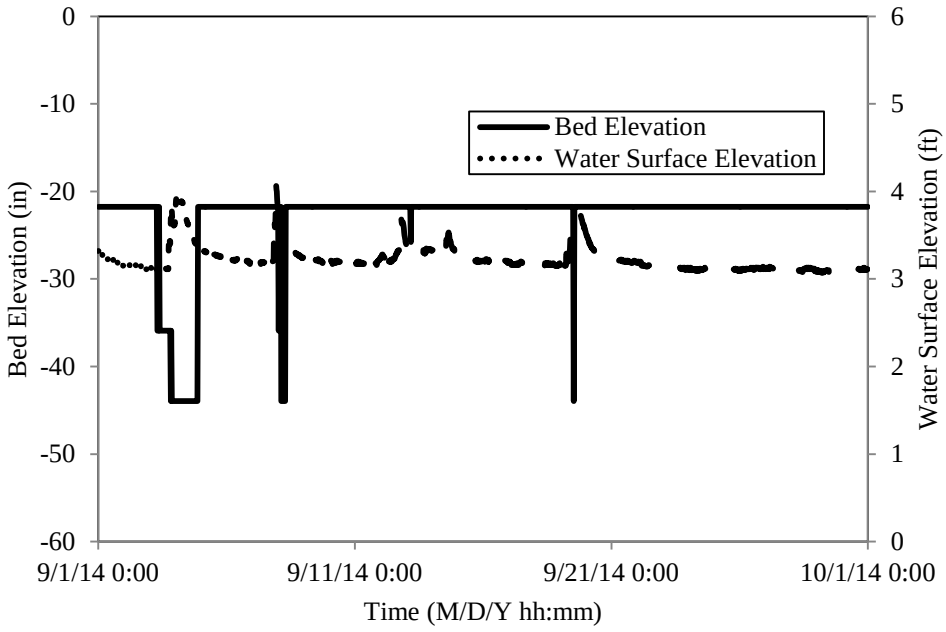

Figure 6.23: Bed elevation from VTP in September 2014.

6.6.3 Performance Comparison between TDR and VTP

Comparison of the bed elevations recorded by the TDR and VTP during the flood events is discussed in this section. A flood event occurred at this station during April 7-9, 2014. Water level increased up to 10 ft above the datum. Figure 6.24 shows the flood event along with the scour recorded by both TDR and VTP. The TDR and VTP are responding to the change in bed level due to the flood event. However, there are some differences in recorded bed elevation. The instruments are placed about 1.5 ft apart, and this would lead to different bed elevation records from TDR and VTP. The TDR and VTP can only record bed elevation up to their probe length. As the length of TDR probe is longer than that of the VTP, the TDR can register scour beyond the limit of the VTP

probe. For this reason, the TDR gives greater maximum scour depth than the VTP for this flood event.

Figure 6.25 shows the response of the instruments to consecutive flood events during April 13–23, 2014. Again, both TDR and VTP are recording bed levels consistently. The maximum scour depth recorded by the instruments is the same as the scour depth is within the probe length of each instrument.

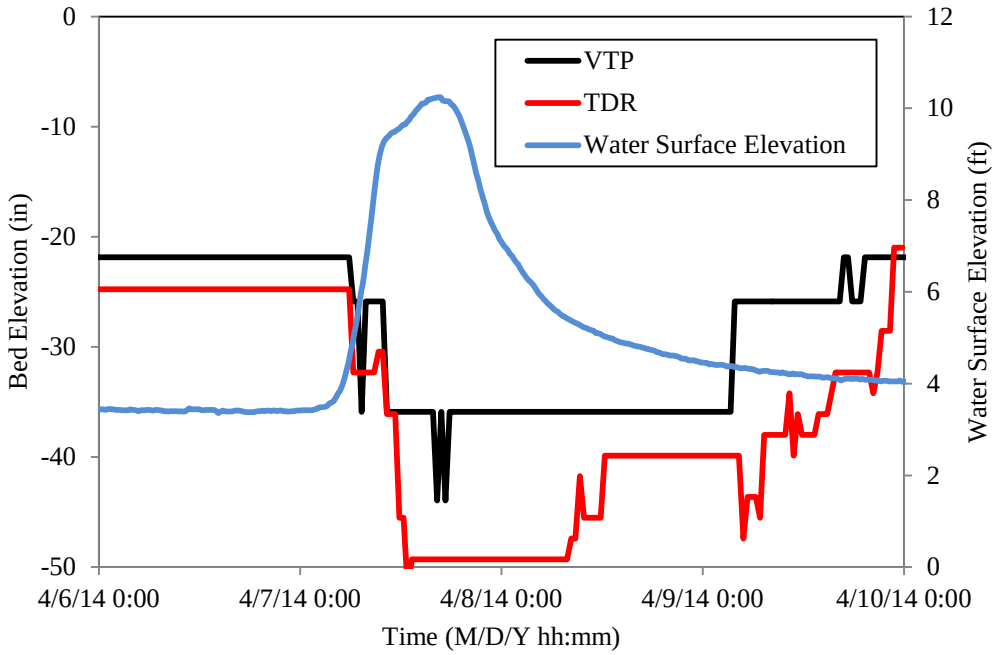

Figure 6.24: Comparison of bed elevation obtained from TDR and VTP for scour event 1.

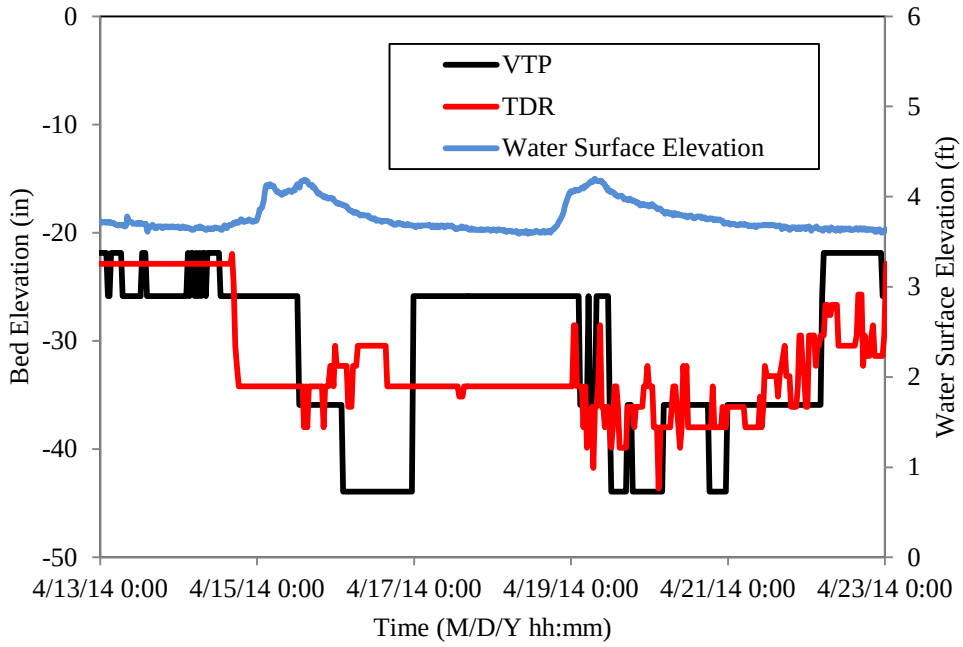

Figure 6.25: Comparison of bed elevation obtained from TDR and VTP for scour event 2.

6.7 Bed Elevation Results from Field Site 2

In this section, bed elevations measured using sonar and TDR at Field Site 2 are presented in chronological sequence. Bed elevations from each instrument correspond to the distance from a common datum (the top of the mounting device, which for the two instruments is the same). The recorded scour depth and water surface elevation based on the USGS gauging station are examined. Data at this site have been collected continuously since March 2014.

6.7.1 Bed Elevation History Using Sonar

The bed elevations recorded by the sonar from March to September 2014 are shown in Figures 6.26–6.32, respectively. Due to the presence of debris at the front pier,

the scour development at the site is restricted. The sonar did not record any scour event at the site. Variation in the bed elevation may be attributed to debris passing under the sonar and instrument resolution.

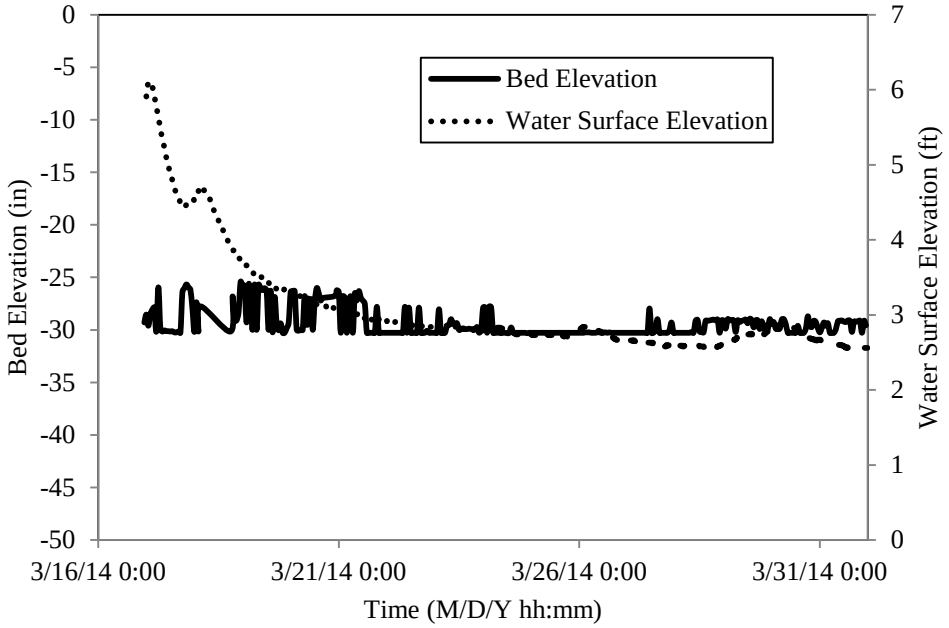

Figure 6.26: Bed elevation from sonar in March 2014.

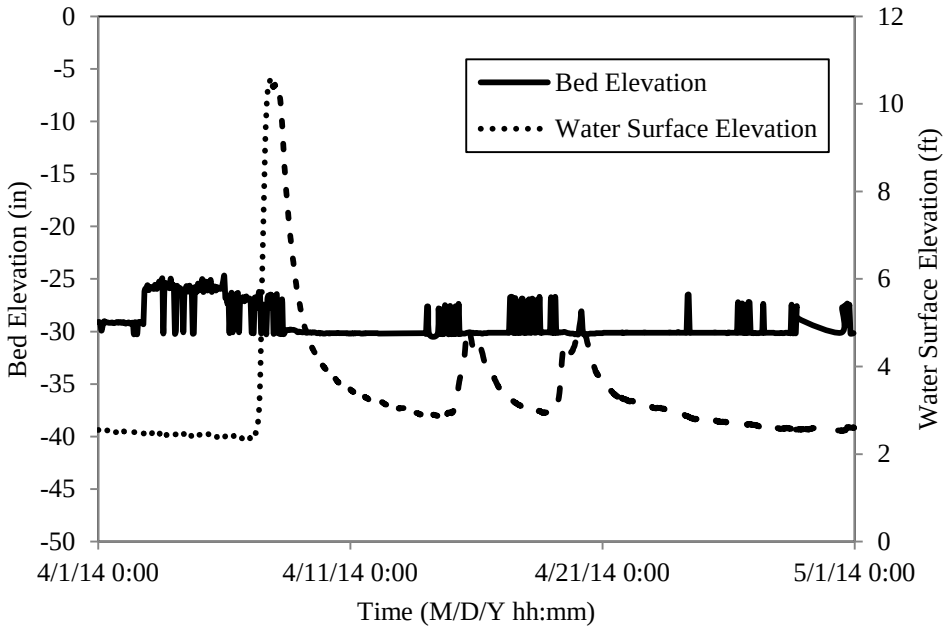

Figure 6.27: Bed elevation from sonar in April 2014.

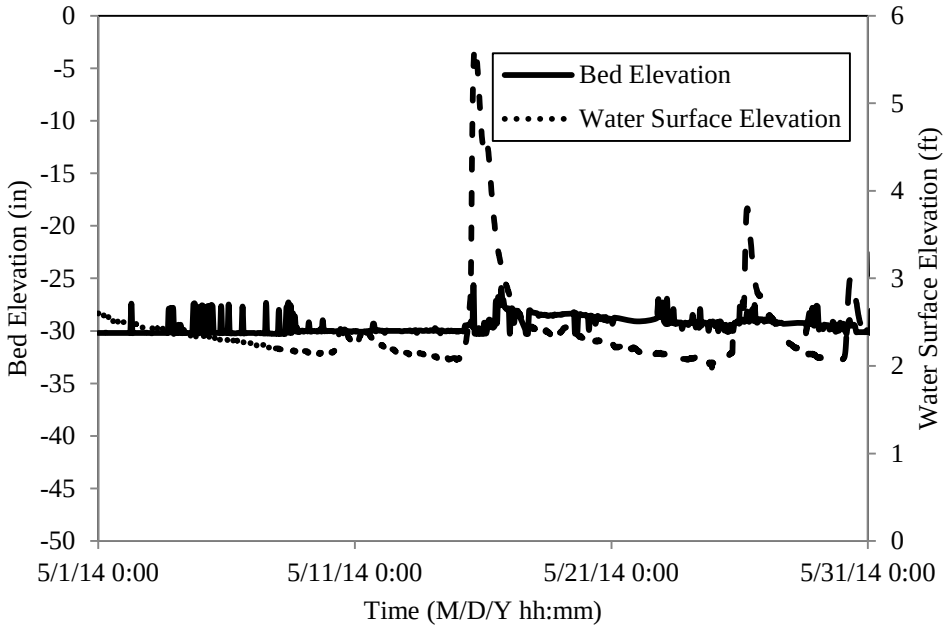

Figure 6.28: Bed elevation from sonar in May 2014.

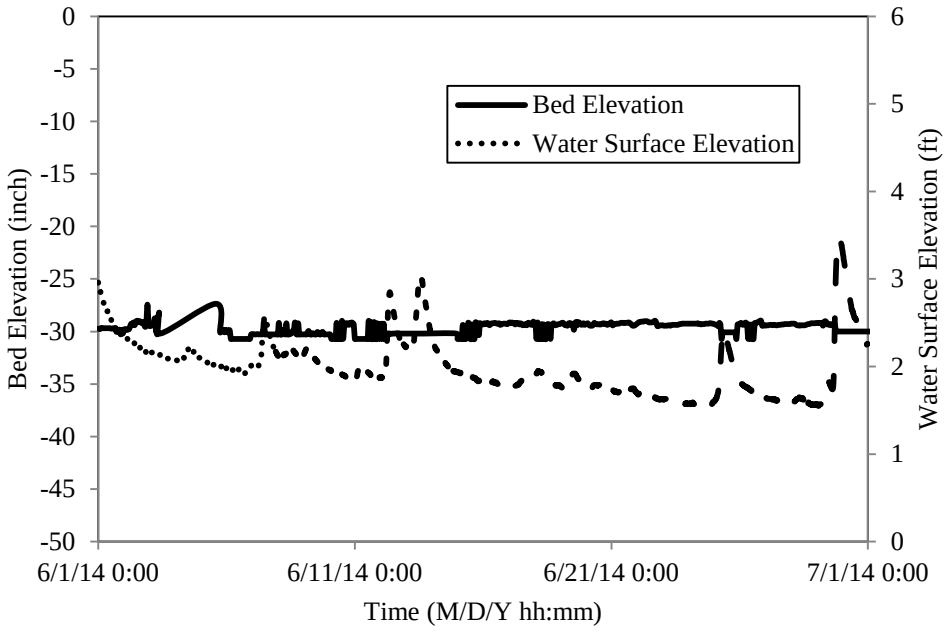

Figure 6.29: Bed elevation from sonar in June 2014.

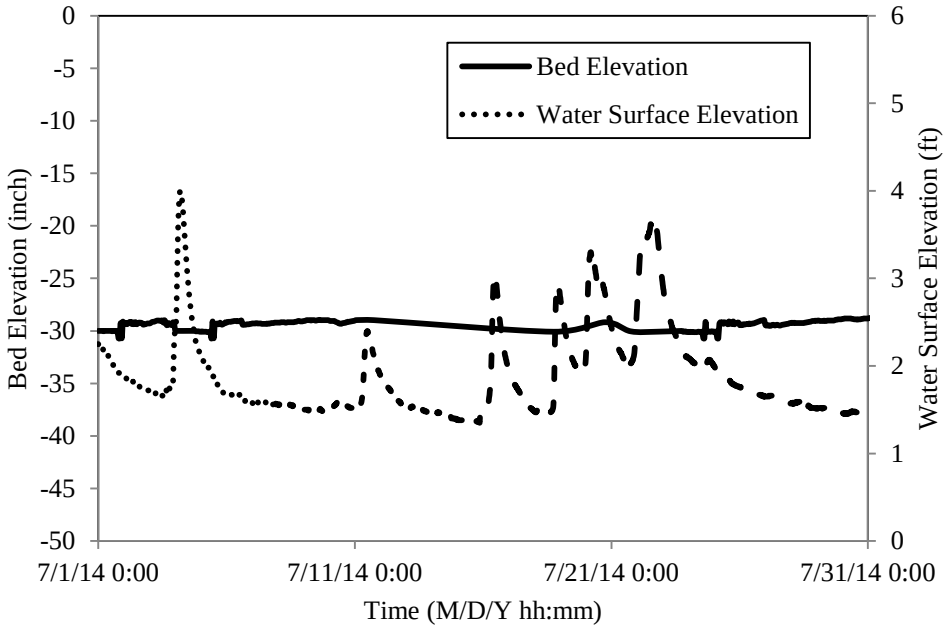

Figure 6.30: Bed elevation from sonar in July 2014.

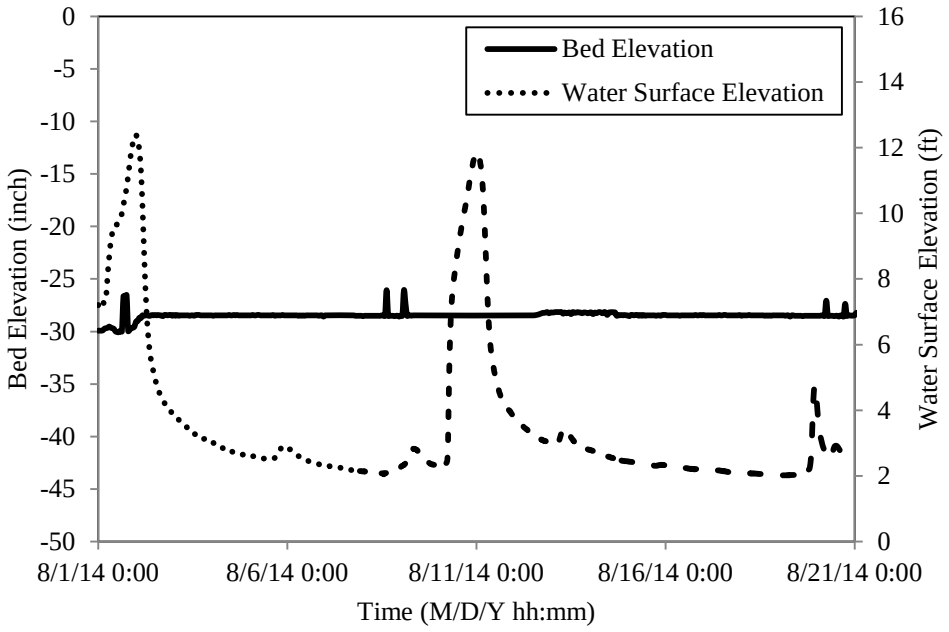

Figure 6.31: Bed elevation from sonar in August 2014.

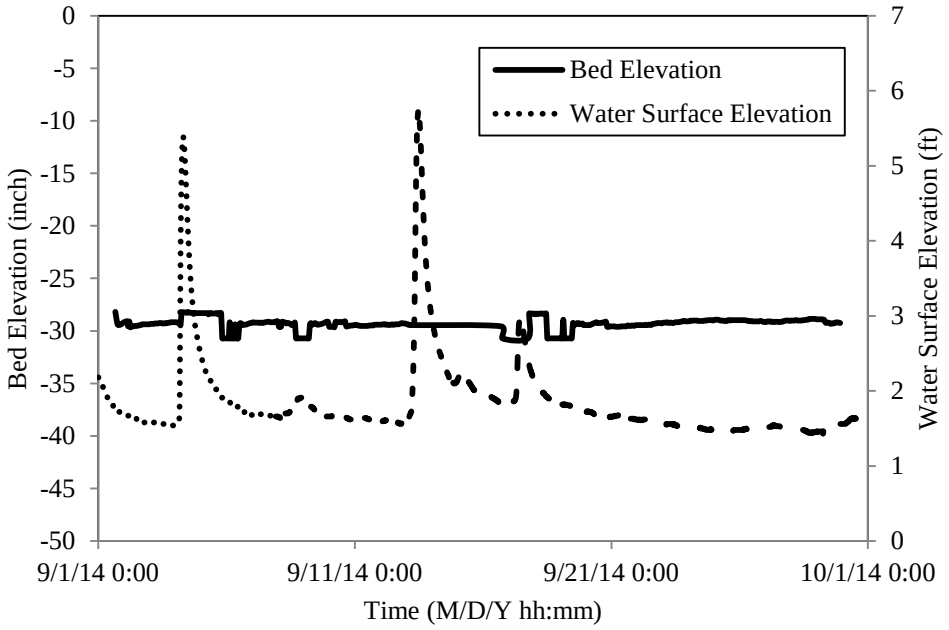

Figure 6.32: Bed elevation from sonar in September 2014.

6.7.2 Bed Elevation History Using TDR

The bed elevations recorded by the TDR from March to September 2014 are shown in Figures 6.33–6.39, respectively. The bed elevation in March (at the start of the record) is about 9 inches lower than that at the sonar site. In addition, the bed elevation at the TDR site shows a cycle of aggradation and degradation during the measurement period, which is not present at the sonar site. The general trend of aggradation and degradation can be fully ascertained once a longer record of bed elevation data becomes available. The TDR record shows a scour event corresponding to the flood event in April 2014 (Figure 6.34). This event was not recorded by the sonar. The TDR records indicate that flooding during the measurement period did not produce any scour at this site.

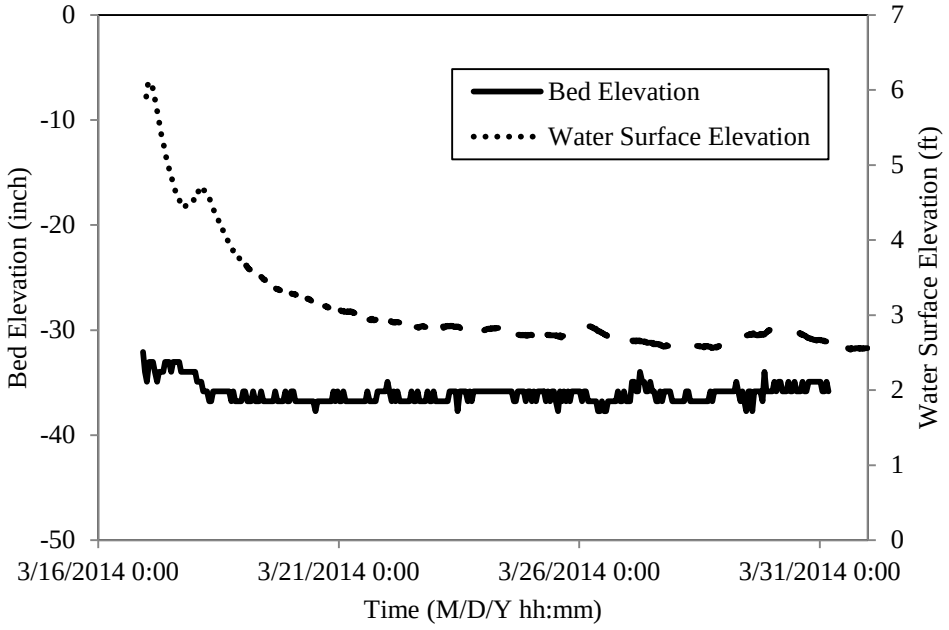

Figure 6.33: Bed elevation from TDR in March 2014.

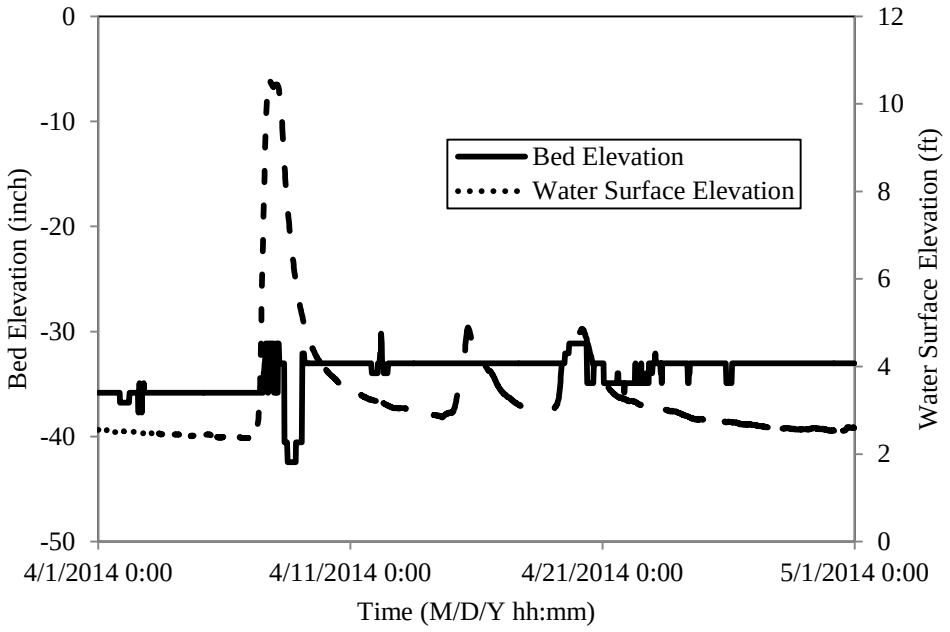

Figure 6.34: Bed elevation from TDR in April 2014.

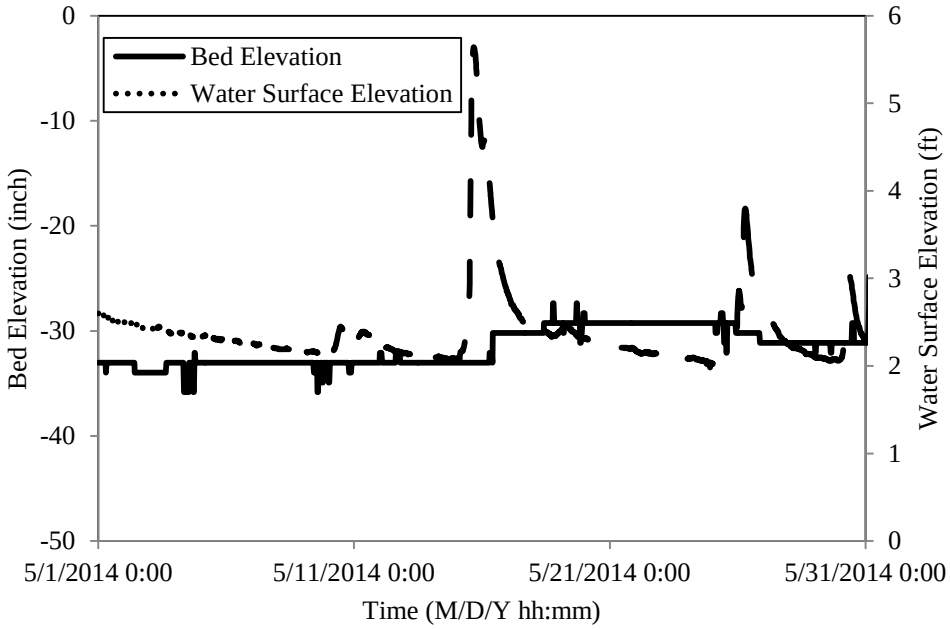

Figure 6.35: Bed elevation from TDR in May 2014.

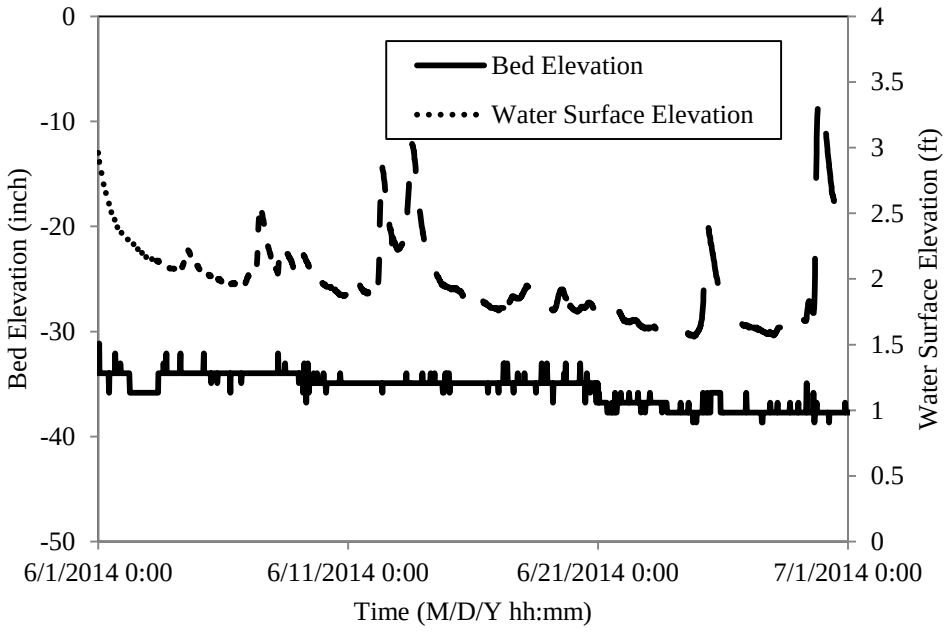

Figure 6.36: Bed elevation from TDR in June 2014.

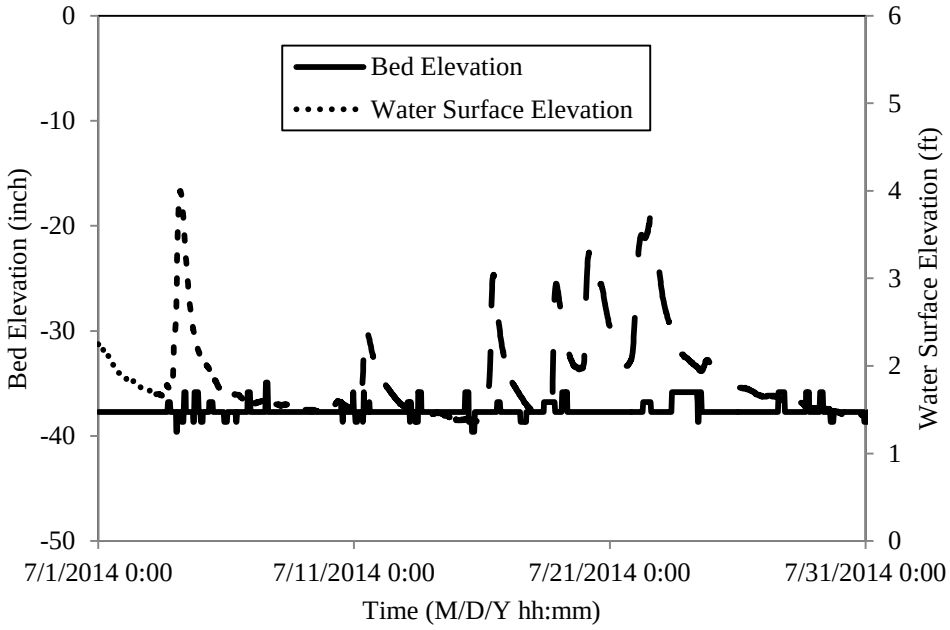

Figure 6.37: Bed elevation from TDR in July 2014.

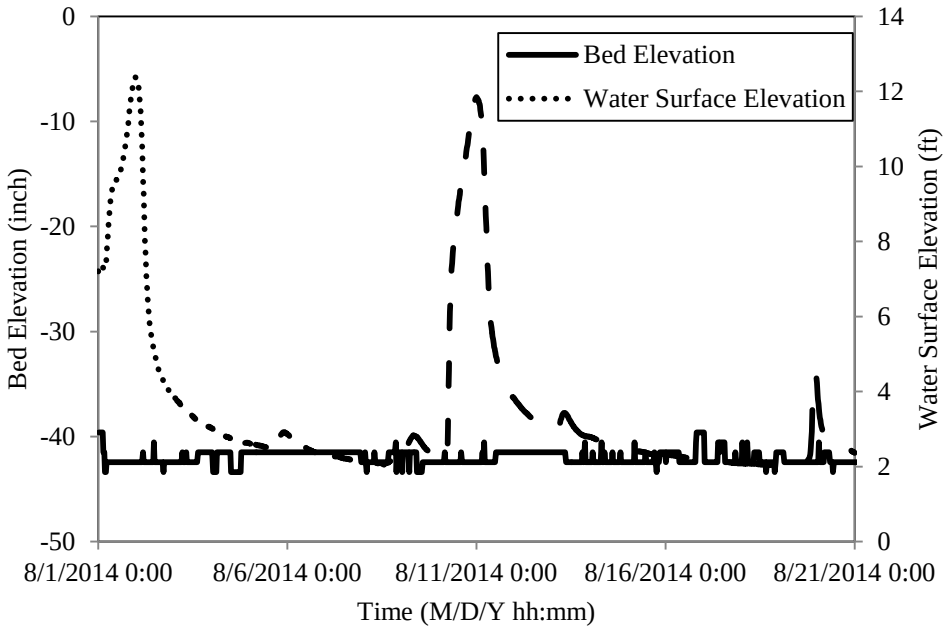

Figure 6.38: Bed elevation from TDR in August 2014.

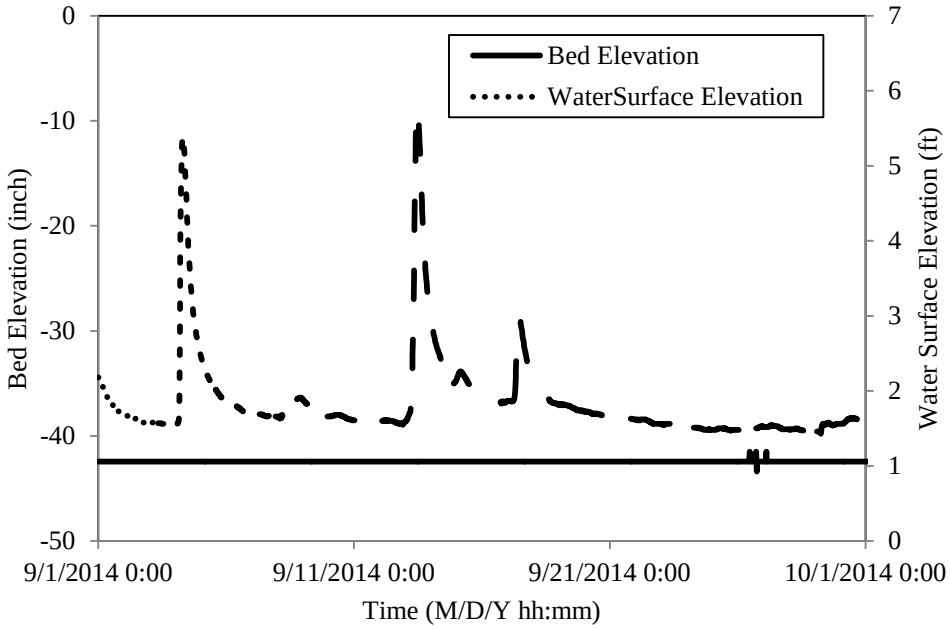

Figure 6.39: Bed elevation from TDR in September 2014.

6.7.3 Performance Comparison between TDR and Sonar

The relative performance of sonar and TDR is evaluated by comparing the bed elevations recorded by the two instruments, together with the water surface elevation at the station during the flood event in April 2014 (Figure 6.40). The scour resulting from the flood event is recorded by the TDR; however, there is no evidence of scour at the sonar site. Although flood events took place during the measurement period based on the water surface elevation data collected from the USGS gauge at this site, records show no scour due to other flood events. The level of debris accumulation may vary during different flow periods and the bed elevation at the instrument site may respond to it. However, for a definitive assessment, a longer duration of recording and a history of debris accumulation levels will be required.

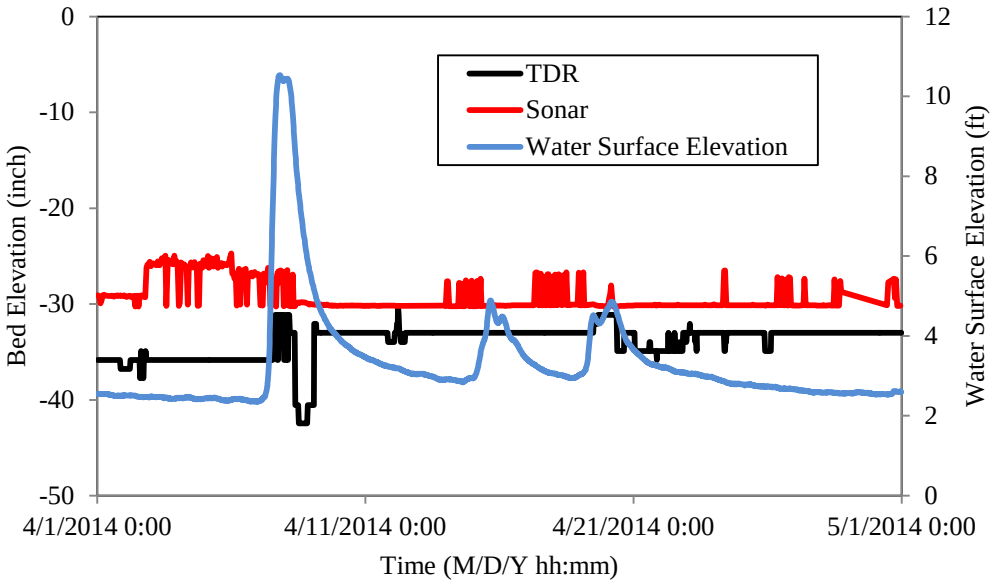

Figure 6.40: Comparison of bed elevation obtained from sonar and TDR.

6.8 Summary

The three devices, VTP, sonar, and TDR were installed in the field to record the bed elevation history. The TDR device installed at Field Site 1 reveals consistent results of bed elevation history with respect to the water surface elevation data obtained from the USGS gauging station. The VTP bed elevation record is limited by the length of the device; however, the bed elevation is recorded accurately considering the resolution of the device (0.25 ft) and corresponds well with the water surface elevation data and the TDR record.

At Field Site 2, there is no evidence of scour based on the bed elevation record obtained using TDR (except for one flood event) and sonar. The scour and refill episodes that are evident at Field Site 1 are absent at this site. Given these results, the accuracy and response of the sonar cannot be evaluated with respect to the TDR.

CHAPTER 7

CONCLUSIONS

7.1 Summary of the Research

Scour remains the leading cause of bridge failure in the United States and is responsible for hundreds of millions of dollars in damage to the nation's transportation infrastructure. It has also been directly linked to the loss of lives resulting from the collapse of bridges during peak flow events. Given the threat to critical components of the transportation system, the current study evaluated the state of the art of the scour monitoring technology, developed a new instrument to overcome some of the deficiencies in the existing methods, and deployed the selected instruments at two different field sites to evaluate performance.

In order to deploy any system for monitoring scour hole formation around a bridge pier or abutment, it is necessary to evaluate the underlying physics that govern the operation of the proposed device. It is also necessary to consider the potential impact of various channel conditions on the proposed scour measurement methods. The existing techniques are reviewed, including both point scour measurement devices and distributed scour monitoring methods. The available techniques reviewed include devices such as magnetic sliding collars, which rely upon the movement of key parts to indicate the presence of scour, and advanced 3D sonar systems that are capable of recording the bed topography around a bridge pier. However, each device has certain strengths and weaknesses, which should be considered when deploying any system in the field. To

facilitate the development of robust scour monitoring systems, the failure modes and effects analysis (FMEA) is proposed to aid in the selection of scour monitoring systems that are resilient to changes in flow properties that exist in natural channels, such as temperature, salinity, suspended sediment, debris, and bed topography.

The review reveals that the two most suitable instruments for scour monitoring are sonar and TDR. A novel method is developed in response to several of the common weaknesses in existing scour monitoring methods. The new method employs sensors that are selected to be sensitive to the natural turbulence in open channel flows. These sensors, classified as vibration-based turbulent pressure sensors (VTP), will vibrate at significantly higher amplitudes when placed in a turbulent flow compared to the sensors buried in the bed. The mean squared acceleration response of these sensors, which is denoted as the energy content in this work, across the depth of a bridge pier or abutment, can be used to determine the bed location. This method is tested experimentally to validate the concept using different materials, shapes, thickness, and size. The experimental results show that the device can be used effectively to determine the bed location.

The VTP sensor type, shape, and material are selected for developing field prototype. Neoprene rubber with circular shape is found to be ideally suited for use as vibration detecting membranes. The size and thickness of the Neoprene are optimized to improve the response and resolution of the device for field deployment. The final radius and thickness are found to be 0.787 inch and 0.063 inch, respectively. The center to center spacing between the sensors is 4 inches, which means that the device will have a

resolution of 4 inches in measuring scour depth. The optimized VTP device is then tested to ensure that the required performance criteria are met for monitoring the formation and refill of scour holes around bridge piers and abutments.

The performance of sonar, TDR, and VTP devices is evaluated for various channel conditions including salinity, temperature, turbidity, bed topography, flow alignment, flow velocity, and bed sediment type, where applicable. For the sonar device, changes in temperature (41 to 104°F) can result in relative errors of up to 6% in channel depth. Salinity (up to 35.5 ppt) can lead to relative errors of up to 3%. The temperature and salinity can be measured in the field to apply appropriate corrections to the sonar readings. The concentration of suspended particles minimally affects the sonar results in still water. For dynamic turbidity, uniform as well as stratified, the relative error in bed level measurements can be significant. The results indicate that measuring the standard deviation of the recorded signal is important to verify the quality of the recorded signal. Lastly, for variable bed topography, the sonar measures the shallowest depth. Therefore, the location of the sonar above the bed and the beam angle are critical for measuring scour depth accurately.

For the TDR device, the channel temperature can affect the measured depth of a scour hole. The relative errors can be of the order of 5% for temperature variation ranging from 44.6 to 104°F. This effect, however, can be mitigated by monitoring the channel temperature in addition to the TDR waveform. For salinities greater than 0.5 ppt, the distinct features in the TDR waveform necessary to determine scour depth are lost. It is

therefore recommended to install the TDR only in freshwater conditions. Turbidity in the channel flow had no measurable effect on the TDR measurements.

The VTP device is not affected by temperature, salinity, or turbidity of the channel flow. In addition, for flow angles up to 90 degrees relative to the VTP, the sensor in the flow and that in the bed can be clearly distinguished based on their energy content. Thus, the bed can be located accurately even in highly misaligned flows. The bed sediment type (clay, sand, etc.) does not influence the energy content of the sensors in the bed and therefore does not impact the VTP device ability to locate the bed. The VTP device was tested for velocity as low as 0.48 ft/s. The response from the VTP in the flow was an order of magnitude greater than the VTP in the sediment, indicating adequate performance even at low flow velocity conditions.

7.2 Recommendations

Table 7-1 shows the FMEA analysis for the TDR, sonar, and VTP devices. The results show the applicability of these three devices under different channel conditions. It is clear that TDR is not the instrument of choice in saline water. The sonar applicability is limited due to turbidity in the channel, especially in case of stratified turbidity that may occur where there is an active bed movement (normally under high flows). The sonar readings are easily affected by the debris accumulation around the instrument. The VTP is affected the most by the debris accumulation around the sensor, especially the sensors that are in the flow closest to the bed. All three instruments are prone to debris damage. However, SEV ratings for sonar and VTP are higher compared to TDR. The TDR is mostly made of metallic pipes and base that are more resistant to debris impact.

The temperature effect is not considered to be a major hindrance for the TDR and sonar as it can be easily measured independently and necessary corrections can be applied to the recorded data. Salinity, on the other hand, is given a high SEV rating as it may vary across the depth and will require multiple sensors in the flow.

Table 7-1: FMEA analysis for the selected instruments.

Instrument	Failure Mode	Effect of Failure	SEV	OCC	DET	RPN
TDR	Water Turbidity	Dielectric constant changes a small amount	1	7	8	56
	Water Temperature	Dielectric constant changes a significant amount	1	9	5	45
	Salinity	Unidentifiable interfaces	10	5	8	400
	Debris	Damage	4	9	1	36
		Obstruction	1	9	1	9
Sonar	Water Turbidity	Multiple reflection and scattering of acoustic pulse	9	10	8	720
	Water Temperature	Change in speed of acoustic pulse	1	9	5	45
	Salinity	Change in speed of acoustic pulse	4	5	6	120
	Debris	Damage	7	9	2	126
		Obstruction	8	9	7	504
VTP	Water Turbidity	Enhances vibration	1	7	5	35
	Water Temperature	Minimal effect on VTP	1	7	5	35
	Salinity	Minimal effect on VTP	1	5	5	25
	Debris	Damage	8	9	4	288
		Obstruction	8	9	6	432

Table 7-2 summarizes the recommendations of this project. For a shallow stream without salinity effects, the TDR may be the best choice. However, if temperature variations are large, it may be necessary to independently record the temperature in the river to apply necessary correction to the TDR raw data. The VTP device is ideally suited for shallow streams in coastal areas as it is not affected by salinity. The sonar needs to be submerged in the water and must be installed at least 2 ft above the river bed. For deep rivers, where TDR and VTP installation may be difficult, sonar can easily be installed by attaching it to a rod. The rod can then be lowered so that sonar is situated close to the bed.

Table 7-2: Recommendations for the selection of an instrument for field deployment.

Device	Temperature	Salinity	Turbidity	Debris		Water Depth	Installation
				Damage	Obstruction		
TDR	Effect: Influences measurements. Remedy: Simultaneous temperature measurement.	Effect: Unidentifiable signal. Remedy: Do not use TDR.	Effect: Minor Influence. Remedy: Not required.	Susceptibility low	No Influence	Shallow /Deep	Complicated for deep water
Sonar	Effect: Influences measurement. Remedy: Simultaneous temperature measurement.	Effect: Influences measurement. Remedy: Simultaneous salinity measurement.	Effect: Unstable sonar reading beyond a 0.3 ft/s flow velocity. Remedy: Use another instrument.	Susceptibility high	Susceptibility high	At least 2 ft above the bed. Reliability decreases as distance from sonar to the bed increases.	Easy for both shallow and deep channels
VTP	Effect: Minor Influence. Remedy: Not required	Effect: Minor Influence. Remedy: Not required	Effect: Minor Influence. Remedy: Not required	Susceptibility high	Susceptibility high	Shallow/ Deep	Complicated for deep water

BIBLIOGRAPHY

Ansari, F., (2010). "Simple cost-effective scour sensor." Research Report ICT-10-070, Illinois Center for Transportation.

Arneson, L.A., Zevenbergen, L.W., Lagasse, P.F., and Clopper, P.E., (2012). "Hydraulic Engineering Circular No.18: Evaluating Scour at Bridges." 5th Edition, U.S. Department of Transportation, Federal Highway Administration, Publication No. FHWA-HIF-12-003.

Atamturktur, S. Hemez, F.M., and Laman, J.A., (2012). "Uncertainty Quantification in model Verification and Validation as Applied to Large Scale Historic Masonry Monuments." Engineering Structures, Vol. 43, 221–234.

Berger, E.H., Royster, L.H., Royster, J.D., Driscoll, D.P., and Layne, M., (2003). "The Noise Manual." 5th Edition, American Industrial Hygiene Association, Fairfax, VA.

Birchak, J.R., Cardner, C.G., Hipp, J.E., and Victor, J.M., (1974). "High dielectric constant microwave probes for sensing soil moisture." Proceedings of the IEEE, 62(1), 93–98.

Blevins, R.D., (1979). *Formulas for Natural Frequency and Mode Shape*. Van Nostrand Reinhold Co., New York.

Blevins, R.D., (1990). *Flow Induced Vibration*. Van Nostrand Reinhold Co., New York.

Brice, J.C., and Blodgett, J.C., (1978). "Countermeasures for hydraulic problems at bridges." Vol. 1 & 2, FHWA/RD-78-162 & 163, Federal Highway Administration, U.S. Department of Transportation, Washington, D.C.

Browne, T.M., (2011). "Underwater acoustic imaging devices for portable scour monitoring." In Scour and Erosion: Proceedings of 5th International Conference on Scour and Erosion. Ed: Burns, S.E., Bhatia, S.K., Avila, C.M.C., Hunt, B.E., ASCE, November 7-10, 2010, San Francisco, CA.

Bruer, M., and Münch, M., (2008). "Fluid–structure interaction using LES – A partitioned coupled predictor–corrector scheme." Proceedings in Applied Mathematics and Mechanics, 8(1), 10515–10516.

Burczynski, J., (1982). "Introduction to the use of sonar systems for estimating fish biomass." FAO Fisheries Technical Paper, No. 191, Revision 1. FIRU/T191, Rev 1.

Butch, G.K., (1996). “Evaluation of selected instruments for monitoring scour at bridges in New York.” North American Water and Environment Congress, ASCE.

Camp, C.V., Pezeshk, S., and Leatherwood, T.D., (1998). “Detecting bridge scour by measuring the thermal variation across the stream bed.” International Water Resources Engineering Conference, Memphis, TN, August 3-6.

Campbell Scientific, (2010). “TDR 100 instruction manual.” Revision: 2/10.

Coles, D., (1956). "The Law of the wake in the turbulent boundary layer," Journal of Fluid Mechanics, Vol. 1, 191–226.

Cooper, T., Chen, H.L., Lyn, D., Rao, A.R., and Altschaeffel, A.G., (2000). “A field study of scour-monitoring devices for Indiana streams.” Final Report, FHWA/IN/JTRP-2000/13, October 2000.

Craig, R.R., (1981). *Structural Dynamics: An Introduction to Computer Methods*. John Wiley and Sons, Inc.

Das, B.M., (1998). *Principles of Geotechnical Engineering*. 4th Edition, PWS Publishing Company, Boston, MA.

Davidson, P.A., (2004). *Turbulence, an Introduction for Scientists and Engineers*. Oxford University Press Inc., New York.

DeFalco, F., and Mele, R., (2002). “The monitoring of bridges for scour and sedimentri.” NDT&E International, Vol. 35, 117–123.

Deng, L., and Cai, C.S., (2010). “Bridge scour: Prediction, modeling, monitoring, and countermeasures—Review.” Practice Periodical on Structural Design and Construction, 15(2), 125–134.

Dey, S., and Barbhuiya, A.K., (2006). “Velocity and turbulence in a scour hole a vertical-wall abutment.” Flow Measurement and Instrumentation, Vol. 17, 13–21.

Drnevich, V.P., Siddiqui, S.I., Lovell, J., and Yi, Q., (2001). “Water content and density of soil insitu by the Purdue TDR method.” TDR 2001: Innovative Applications of TDR Technology, Infrastructure Technology Institute, Northwestern University, Evanston, IL.

Eilertsen, R.S., and Hansen, L., (2008). “Morphology of river bed scour on a delta plain revealed by interferometric sonar.” Geomorphology, Vol. 94, 58–68.

Ettema, R., and Zabilansky, L.J., (2004). “Ice influences on channel stability: Insights from Missouri’s Fort Peck Reach”, Journal of Hydraulic Engineering, 130(4), ASCE, 279–292.

Fisher, M., (2012). “Analysis and evaluation of existing and novel turbulent dynamic pressure based methods for measuring bridge pier and abutment scour.” Ph.D. Dissertation. Clemson University, USA.

Fisher, M., Khan, A.A., and Atamturktur, S., (2013a). “The state of the art in scour monitoring.” In Sediment Transport: Monitoring, Modeling and Management, Ed: Khan, A.A., and Wu, W., Nova Science Publishers, Inc., New York, ISBN: 978-1-62618-683-5, 2013, 37–72.

Fisher, M., Chowdhury, M.N., Khan, A.A., and Atamturktur, S., (2013b). “An evaluation of scour measurement devices.” Flow Measurement and Instrumentation, Vol. 33, 55–67.

Fisher, M., Atamturktur, S., and Khan, A.A., (2013c). A novel vibration-based monitoring technique for bridge pier and abutment scour. Structural Health Monitoring, 12(2), 114–125.

Fisher, M., Khan, A.A., and Atamturktur, S., (2013d). Scour monitoring via turbulent open channel flow. Measurement Science and Technology, 24(8), Paper No. 085602.

Galanti, B., and Tsinober, A., (2004). “Is turbulence ergodic?” Physics Letters A, Vol. 330, 173–180.

Gray, J.R., Melis, T.S., Patiño, E., Larsen, M.C., Topping, D.J., Rasmussen, P.P., and Figueroa-Alamo, C., (2003). “US Geological Survey research on surrogate measurements for suspended sediment.” In Proceedings of the 1st Interagency Conference on Research in Watersheds, 95–100.

Guemes, A., and Menendez, J.M., (2006). “Chapter 3: Fiber-optic sensors.” In Structural Health Monitoring, Ed: Balageas, D. Fritzen, C.P., Guemes, A., ISTE Ltd, 225–285.

Guo, N., Cawley, P., and Hitchins, D., (1992). “The finite element analysis of the vibrational characteristics of piezoelectric discs.” Journal of Sound and Vibration, 159(1), 115–138.

Hamilton, E.L., (1980). “Geoacoustical modeling of the sea floor.” Journal of the Acoustical Society of America, 68(5), 1313–1340.

Hayden, J.T., and Puleo, J.A., (2011). “Near real-time scour monitoring system: Application to Indian River Inlet, Delaware.” Journal of Hydraulic Engineering, ASCE, 137(9), 1037–1046.

Hayes, D.C., and Drummond, F.E., (1995). "Use of fathometers and electrical-conductivity probes to monitor riverbed scour at bridge piers." USGS, Water Resource Investigations Report 94-4165, Richmond, VA.

Holnbeck, S.R., and McCarthy, P.M., (2011). "Monitoring hydraulic conditions and scour at I-90 bridges on Blackfoot River following removal of Milltown Dam near Bonner, Montana, 2009." In Scour and Erosion: Proceedings of 5th International Conference on Scour and Erosion, Ed: Burns, S.E., Bhatia, S.K., Avila, C.M.C., Hunt, B.E., ASCE, November 7-10, 2010, San Francisco, CA.

Hunt, B.E., (2005). "Scour monitoring programs for bridge health." Transportation Research Record: Journal of the Transportation Research Board, Washington D.C., 531–536.

Hunt, D., (2009). "Monitoring scour critical bridges." NCHRP Synthesis 396, Transportation Research Board, Washington, D.C.

Hurther, D., and Lemmin, U., (2001). "A correction method for turbulence measurements with a 3D acoustic Doppler velocity profiler." Journal of Atmospheric and Oceanic Technology, Vol. 18, 446–458.

Isley II, J., Saafi, M., and Julius, J., (2006). "MEMS-based sensor networks for bridge stability safety monitoring during flood induced scour." In Bridge Maintenance, Safety, Management, Life-cycle Performance and Cost: Proceedings of the Third International Conference on Bridge Maintenance, Safety and Management, Ed: Cruz, P.J.S., Frangopol, D.M., Porto, Portugal, July 16-19, 2006.

Itakura, T., and Kishi, T., (1980). "Open channel flow with suspended sediments." Journal of the Hydraulics Division, Proceedings of the American Society of Civil Engineers, 106(HY8), 1325–1343.

Jaffe, H., and Berlincourt, D.A., (1965). "Piezoelectric transducer materials." Proceedings of the IEEE, 53(10), 1372–1386.

Kironoto, B.A., and Craf, W.H., (1994). "Turbulence characteristics in rough uniform open-channel flow." Proceedings of the ICE - Water Maritime and Energy, 106(4), 333–344.

Ko, Y.Y., Lee, W.F., Chang, W.K., Mei, H.T., and Chen, C.H., (2011). "Scour evaluation of bridge foundations using vibration measurement." In Scour and Erosion: Proceedings of 5th International Conference on Scour and Erosion, Ed: Burns, S.E., Bhatia, S.K., Avila, C.M.C., Hunt, B.E., ASCE, November 7-10, 2010, San Francisco, CA.

Kuwahara, S., (1939). “Velocity of sound in sea water and calculations of the velocity for use in sonic soundings.” Hydrogeologic Review., Vol. 16, 123–140.

Leroy, C.C., (1969). “Development of simple equations for accurate and more realistic calcualtion of the speed of sound in seawater”, The Journal of the Acoustical Society of America, 46(1B).

Lagasse, P.F., Richardson, E.V., Schall, J.D., and Price, G.R., (1997). “Instrumentation for measuring scour at bridge piers and abutments.” NCHRP Report 396: TRB, National Research Council, Washington, D.C.

Lagasse, P.F., Clopper, P.E., Pagán-Oriz, J.E., Zevenbergen, L.W., Arneson, L.A., Schall, J.D., and Girard, L.G., (2009). “Bridge scour and stream instability countermeasures: Experience, selection and design guidance.” Hydraulic Engineering Circular No.23, 3rd Edition, Publication No. FHWA-NHI-09-111, U.S. Department of Transportation, Federal Highway Administration.

Lin, Y.B., Chang, K.C., Lai, J.S., and Wu, I.W., (2004). “Applications of optical fiber sensors on local scour monitoring.” Proceedings of the IEEE: Sensors, Vol. 2, 832–835.

Lin, Y.B., Lai, J.S., Chang, K.C., and Li, L.S., (2006). “Flood scour monitoring system using fiber bragg grating sensors.” Smart Materials and Structures, Vol. 15, 1950–1959.

MacKenzie, K.V., (1981). “Nine-term equation for sound speed in the oceans.” Journal of the Acoustical Society of America, 70(3), 807–812.

Manzoni, S., Crotti, G., Cigada, A., Inzoli, F., and Ballio, F., (2011a). “Monitoring bridge scour by bragg grating array.” In Scour and Erosion: Proceedings of 5th International Conference on Scour and Erosion, Ed: Burns, S.E., Bhatia, S.K., Avila, C.M.C., Hunt, B.E., ASCE, November 7-10, 2010, San Francisco, CA.

Manzoni, S., Crotti, G., Ballio, F., Cigada, A., and Colombo, E., (2011b). “BLESS: A fiber optic sedimeter.” Flow Measurement and Instrumentation, 22(5), 447–455.

Mason, R.R., and Sheppard, D.M., (1994). “Field performance of an acoustical scour-depth monitoring system.” In Fundamentals and Advancements in Hydraulic Measurements and Experiments, Ed: Pugh, C.A., Proceedings of the Symposium, Buffalo, N.Y., ASCE, August 1-5, 1994.

Meecham, W.C., (1958). “Relationship between time symmetry and reflection symmetry of turbulent fluids.” The Physics of Fluids, 1(5), 408–410.

Millard, S.G., Bunget, J.H., Thomas, C., Soucos, M.N., Shaw, M.R., and Patterson, A., (1998). “Assessing bridge pier scour by radar.” NDT&E International, 31(4), 251–258.

Mueller, D. S., (2000). “National bridge scour program-measuring scour of the streambed at highway bridges.” U.S. Geological Survey, Reston, VA.

Murillo, J.A., (1987). “The scourge of scour.” Civil Engineering, July, ASCE, 66–69.

Nakagawa, H., Nezu, I., and Ueda, H., (1975). “Turbulence of open channel flow over smooth and rough beds”, Proceedings of the Japan of Society of Civil Engineers, Vol. 241, 155–168.

Nassif, H., Ertekin, A.O., and Davis, J., (2002). “Evaluation of bridge scour monitoring methods.” Final Report, Federal Highway Administration, Report FHWA-NJ-2003-09, March, 2002.

Neill, C.R., (1964). “River-bed scour: A review for bridge engineers.” Contract No. 281, Research Council of Alberta, Calgary, Alberta, Canada.

Nezu, I., and Nakagawa, H., (1993). *Turbulence in Open-Channel Flows.* IAHR Monograph, A.A. Balkema Publishers, Rotterdam, Netherlands.

Nezu, I., and Rodi, W., (1986). “Open-channel flow measurements with a laser Doppler anemometer.” Journal of Hydraulic Engineering, ASCE, 112(5), 335–355.

Nezu, I., (1977). “Turbulent structure in open-channel flows.” Ph.D. Dissertation presented to Kyoto University, Kyoto, Japan.

Nezu, I., (2005). ”Open-channel flow turbulence and its research prospect in the 21st century.” Journal of Hydraulic Engineering, ASCE, 131(4), 229–246.

N.T.S.B., (1987). “Collapse of New York Thruway (I-90) Bridge, Schoharie Creek, near Amsterdam, New York, April 5, 1987.” NTSB Number: HAR-88/02, NTIS Number: PB88-916202.

N.T.S.B., (1989). “Collapse of the northbound U.S. Route 51 Bridge spans over the Hatchie River, near Covington, Tennessee, April 1, 1989.” NTSB Number: HAR-90/01, NTIS Number: PB90-916201.

Parker, G.W., Bratton, L., and Armstrong, D.S., (1997). “Stream stability and scour assessments at bridges in Massachusetts.” U.S. Geological Survey Open File Report No. 97-588 (CD-ROM), Massachusetts Highway Department Bridge Section, Marlborough, MA.

Panton, R.L., (2005). *Incompressible Flow*. 3rd Edition, John Wiley and Sons, Inc., Hoboken, New Jersey.

Placzek, G., and Haeni, F.P., (1995). "Surface geophysical technique used to detect existing and infilled scour holes near bridge piers." USGS Water-Resources Investigations Report 95-4009.

Rhodes, J., and Trent, R., (1993). "Economics of floods, scour and bridge failures." In Hydraulic Engineering '93: Proceedings of 1993 Conference, Ed: Shen, H.W., Su, S.T., Wen. F., ASCE, July 25-30, San Francisco, CA.

Richardson J.R., Price, G.R., Richardson, E.V., and Lagasse, P.F., (1996). "Modular magnetic scour monitoring device and method for using the same." U.S. Patent # 5532687, Issued July 2, 1996.

Richardson, J.R., and Price, J., (1993). "Emergent techniques in scour monitoring devices." In Hydraulic Engineering '93: Proceedings of 1993 Conference, Ed: Shen, H.W., Su, S.T., Wen. F., ASCE, July 25-30, San Francisco, CA.

Roberson, R.E., (1951). "Vibration of a clamped circular plate carrying concentrated mass." West Coast Conference of the Applied Mechanics Division, The American Society of Mechanical Engineers, Stanford, CA, June 22-23, 349–352.

Robins, A.J., (1990). "Reflection of plane acoustic waves from a layer of varying density." Journal of the Acoustical Society of America, 87(4), 1546–1552.

Samizo, M., Watanabe, S., Fuchiwaki, A, and Sugiyama, T., (2007). "Evaluation of structural integrity of bridge pier foundations using microtremors in flood conditions." Quarterly Report of RTRI, 48(3), 153–157.

Samizo, M., Watanabe, S., Sugiyama, T., and Okada, K., (2011). "Evaluation of the structural integrity of bridge pier foundations using microtremors in flood conditions." In Scour and Erosion: Proceedings of 5th International Conference on Scour and Erosion, Ed: Burns, S.E., Bhatia, S.K., Avila, C.M.C., Hunt, B.E., ASCE, November 7-10, 2010, San Francisco, CA.

Shirole, A.M., and Holt, R.C., (1991). "Planning for a comprehensive bridge safety assurance program." Transportation Research Record, No. 1290, Vol. 1, Transportation Research Board, National Research Council, Washington, D.C.

Spindel, R.C., (1998). "Chapter 38: Oceanographic and navigational instruments." In Handbook of Acoustics, Ed: Crocker, M. J., John Wiley and Sons, Inc.

Stogryn, A., (1971). “Equations for calculating the dielectric constant of saline water.” IEEE Transactions on Microwave Theory and Techniques, August, 733–736.

Stoll, R.D., and Kan, T.K., (1981). “Reflection of acoustic waves at a water-sediment interface”, Journal of the Acoustical Society of America, 70(1), 149–156.

Topp, G.C., Davis, J.L., and Annan, A.P., (1980). “Electromagnetic determination of soil water content: Measurements in coaxial transmission lines.” Water Resources Research, 16(3), 574–582.

Trucano, T.G., Pilch, M, and Oberkampf, W.L., (2002). “General concepts for experimental validation of ASCI code applications.” Sandia National Labs, Report No. SAND2002-0341.

Urick, R.J., (1975). *Principles of Underwater Sound*, McGraw-Hill Inc, New York, USA.

USGS, (2006a). “Water Data Report 2006: 02172053 Cooper River at Mobay near North Charleston, SC.”, U.S. Dept. of Interior, U.S. Geological Survey.

USGS, (2006b). “Water Data Report 2006: 02156500 Broad River Near Carlisle, SC.” U.S. Department of Interior, U.S. Geological Survey.

von Karman, T., (1948). “Progress in the statistical theory of turbulence.” Proceedings of the National Academies in Science, Vol. 34, 530–539.

Webb, D.J., Anderson, N.L., Newton, T., and Cardimona, S., (2000). “Bridge scour: Application of ground penetrating radar.” FHWA and Missouri DOT Special Publication.

Yankielun, N.E., and Zabilansky, L.J., (1999). “Laboratory investigation of time domain reflectometry system for monitoring bridge scour.” Journal of Hydraulic Engineering, ASCE, 125(12), 1279–1284.

Yao, C., Darby, C., Hurlebaus, S., Price, G.R., Sharma, H., Hunt, B.E., Yu, O.Y., Chang, K.A., and Briaud, J.L., (2011). “Scour monitoring development for two bridges in Texas.” In Scour and Erosion: Proceedings of 5th International Conference on Scour and Erosion, Ed: Burns, S.E., Bhatia, S.K., Avila, C.M.C., Hunt, B.E., ASCE, November 7-10, 2010, San Francisco, CA.

Yu, X., and Yu, X., (2006). “Time domain reflectometry tests of multilayered soils.” Proceedings of the TDR 2006, Purdue University, West Lafayette, USA, Sept. 2006.

Yu, X., and Yu, X., (2011). “Development and evaluation of an automatic algorithm for a time-domain reflectometry bridge scour monitoring system.” Canadian Geotechnical Journal, Vol. 48, 26–35.

Yu, X., and Zabilansky, L.J., (2006). “Time domain reflectometry for automatic bridge Scour monitoring.” In GeoShanghai 2006: Site and Geomaterial Characterization, GSP 149, Ed: Puppala, A. J., Fratta, D., Alshibli, K., and Pamukcu S., ASCE.

Zabilansky, L.J., Ettema, R., Weubeen, J., and Yankielun, N., (2002). “Survey of river ice influences on channel bathymetry along the Fort Peck Reach of the Missouri River, winter 1998–1999.” Technical Report ERDC/CRREL TR-02-14., US Army Corps of Engineers, Engineer Research and Development Center, September, 2002.

Zabilansky, L.J., (1996). “Ice force and scour instrumentation for the White River, Vermont.” Special Report 96-6, U.S. Army Corps of Engineers, Cold Regions Research and Engineering Laboratory.